5-2013

Alkane Adsorption on MgO(100): Volumetric Isotherm, Inelastic Neutron Scattering, and Computational Studies

Andrew Spencer Hicks
ahicks7@utk.edu

To the Graduate Council:

I am submitting herewith a dissertation written by Andrew Spencer Hicks entitled "Alkane Adsorption on MgO(100): Volumetric Isotherm, Inelastic Neutron Scattering, and Computational Studies." I have examined the final electronic copy of this dissertation for form and content and recommend that it be accepted in partial fulfillment of the requirements for the degree of Doctor of Philosophy, with a major in Chemistry.

John Z. Larese, Major Professor

We have read this dissertation and recommend its acceptance:

T. Ffrancon Williams, Frank Vogt, Takeshi Egami

Accepted for the Council:

Carolyn R. Hodges

Vice Provost and Dean of the Graduate School

(Original signatures are on file with official student records.)

Alkane Adsorption on MgO(100):
Volumetric Isotherm, Inelastic Neutron Scattering, and Computational Studies

A Dissertation
Presented for the
Doctor of Philosophy Degree
The University of Tennessee, Knoxville

Andrew Spencer Hicks
May 2013

DEDICATION

The following work is dedicated to the search for Absolute Truth.

ACKNOWLEDGEMENTS

I am eternally grateful, I Am that I Am.

I have received so much help along my journey, and I could not possibly give adequate thanks in the space and time provided. I pray that those not mentioned by name understand these limitations and do not take offense.

I thank my family for shaping my life and for loving me no matter how many mistakes I made along the way. Mom and Dad have done more than anyone to help me become the man I am today. Words cannot express my gratitude for the love and support they have given me. I thank them as well as Grandma, Granddaddy, Grandpop, and Grandma Blanche for sacrificing so that I may have more opportunities than they did. I especially thank my grandparents for sacrificing for my parents as they have sacrificed for me. You will be with me always. I thank Kadee for loving me even though she was often on the wrong end of many of my missteps (a steep driveway and a broken office chair come to mind). I may not have always been the best big brother, but I hope you at least learned from my mistakes. Michael, thanks for being my partner in crime through the years as well as my first homey. Without him and Laurie, Charlie, Matt, Eric, and James, family vacations would not have been the same. Along with my parents and grandparents, Connie, Le, Norn, and Harli deserve special thanks for helping keep all of us in line during those days. Allie, Sarah, Siobhan, Katie, Cheryl, and someone else very important likewise deserve thanks for keeping us all in line now. I similarly thank Terry for helping my dad contain his addiction to new cars, as well as being a wonderful Steppy. Lastly, I thank my in-laws Rus, Yvonne, Samantha, Dear, Nanni, Maw Maw, Todd and Toni for treating me like family from the day I met them. Thank you everyone for your love and support.

Throughout grade school, I was blessed with outstanding teachers, and the lessons they taught me remain with me. Mr. Austin and Mrs. Bovender among others deserve special mention for advancing my intellectual development. During this period, I often learned more about life in athletics than in the

classroom. Accordingly I would like to thank Coach Sensabaugh, Coach Brewer, Coach Watson, Coach Vance, and Coach Clark among others for their guidance and for teaching me the value of hard work and discipline,. My former and teammates also deserve thanks for their contributions and for helping me through some difficult times. Jamaar taught me more about the preciousness of life than I ever cared to know, and I still miss him greatly. Throughout everything, I could not have asked for more loyal and steadfast friends than Matt, Brandon, Zack, and Thad. I have long considered Matt my spiritual advisor, and special thanks to him for helping me with this and the previous section. YHWH willing, we will all remain close for decades to come.

I am blessed to have had excellent professors throughout my undergraduate studies, and I especially want to thank Dr. Stiver for introducing me to the economics and politics of liberty and Dr. Chen for introducing me to quantum mechanics. The lessons I learned from them forever changed the way I think. As in grade school, I often learned the most about life while pursuing "extracurricular" activities, and for this I thank all of my Delta Upsilon fraternity brothers. Dikaia Upotheke. The experience of Hell Week during my pledge semester helped enormously in preparing me for the task of writing a dissertation: I would describe both experiences as the most amount of fun that I never want to have again. I could not have made it through without my fellow Beta Delta pledge brothers, especially Kiel, Coop, Zebrak, Shark, and Tutt. I hope that I returned the favor. I especially want to thank Kiel and Keith, who were always there for me in my darkest hours. Elder brothers such as Moose, Keith, Schmanske, Jeff George, and Pellet were excellent mentors as I made the tricky transition to living on my own. I can only hope that I was as an effective mentor to younger members as they were to me.

My graduate experience in the UTK Chemistry Department has further enlightened my thought process, and along the way I have made many great friends outside my research group. Pippin and Vik, you guys have been great, and I doubt I will ever have as much fun in one week as we did Myrtle Beach.

Additionally, numerous staff members including Bill Gurley, Gary Wynn, Pam Roach, and Marilyn Ownby helped me enormously throughout my time here, and each deserves my thanks. My coursework provided me with the foundation necessary to become a competent scientist, and for that I thank Dr. Harrison, Dr. Hinde, Dr. Feigerle, Dr. Plummer, Dr. Egami, Dr. Moreo, Dr. Williams and Dr. Larese. I additionally would like to thank my committee members—Dr. Vogt, Dr. Egami, Dr. Williams, and Dr. Larese—for granting me the freedom to write my dissertation at my own pace and not holding my feet to the fire regarding the deadline that traditionally occurs two weeks prior to defense date.

There are so many people to thank within the research group. As in earlier stages of my life, I benefitted from the wisdom of my senior fellow group members, and in this regard I would like to thank Rick, Pete, George Thomas, Sami, Mike, Lillian, David, Andi, Paige, and Ben. I came into the group with very little research experience, and Andrea Freitag deserves special mention for helping develop my skills as an experimentalist. Without her help, I do not know if my isotherm studies would have ever gotten off the ground. In this regard, I also owe a debt to Nathaniel, who is a troubleshooting whiz in the lab and has helped me with so many with the countless problems that always seem to creep up. Similarly, the Accelrys calculations reported could not have been completed without help from Nick and George (R.). Moreover, my beliefs, both science-related and otherwise, have greatly been clarified in my mind thanks to conversations with great friends such as Nathaniel and Ben. In this vein, I would also like to thank Sourav for sharing with me a proverb from his native country as well as Hangning for showing me the meaning of true toughness. I should also thank the newest member of the group, Daniele, for making me laugh during a particularly stressful period of my life. Also thanks to all of the former Chem 479 students who would later join the group: Steve, Malcolm, Sean, Morgan, Brandon, and Chris. I have genuinely enjoyed going to lunch and cutting up in the office with all of you.

Without question, the group member to whom I am most grateful is Dr. Larese. As Lillian said in her dissertation, “Though we have had our ups and downs, he has continued to believe in me and my abilities.” Also like Lillian, I suspect that I owe Mrs. Larese a debt of gratitude for being my champion during the downs. During those times, I relied primarily on conversations with other group members and on my unwavering faith that Dr. Larese was more concerned with my interests than his own. This was and is always evident by the time, money and effort that he invests in his students while asking for little in return. Early on, I found his “dumb like a fox” teaching style confusing, and sometimes even maddening, but I now realize the method in his madness. Above all, I thank him for sharing with me his passion for science, which continues to amaze me. If I could be as passionate about any one thing as he is about science, it would greatly simplify my future career decisions, in which I know he will continue to play a major role. Regardless of what the future may bring, I know that I will always have Dr. Larese to thank for helping me unlock my potential in a way no other mentor ever has.

I could never have achieved what I have here at UT without my soul-mate Blake. She has helped support us financially, selflessly delaying her own dreams while I pursued mine. More importantly, she supports me emotionally and is a constant source of love and strength. Ever since we first met, she has filled my life with purpose and has restrained my wilder impulses. In short, she keeps me grounded, and without her my mind would fly off into deep space. This much was never as obvious as in the past months as I frantically assembled this dissertation. While I neglected her needs in a mad rush to make all the pieces fit, she looked after my needs by reminding me of Earthly concerns such as eating, sleeping, showering, and brushing my teeth. What is all the more remarkable is that she did all of this while carrying our first child. I am delighted that she finally has the chance to fulfill her dreams of motherhood. She is already an exceptional mother. If I can be half as good a father, then I know our daughter will become as great a woman as Blake.

This brings me to my final and most exciting acknowledgement. Our daughter Vivienne has filled me with immeasurable joy in her brief existence in this world, and I'm sure she will continue to do so for years to come. I have seen her face only on ultrasounds, but she more than anyone motivates me to be the best man I can be. Without her, I do not know how long I would have taken to get my butt in gear and try to put the pieces together. To her I am eternally grateful.

ABSTRACT

Volumetric adsorption isotherms and computational molecular dynamics (MD) simulations were performed for nonane and decane adfilms on MgO(100) nanocubes. From the isotherms, variety of thermodynamic quantities are calculated. These values, along with visual inspection of the isotherms, indicate a layer by layer trend from 2D to 3D behavior. This is attributed to the increasing importance of vertical adsorbate-adsorbate interactions as distance from the surface increases. Additionally, a 2D phase transition is observed for the first adsorbed layer as indicated by the evolution of the widths of the isotherm first derivative peaks. These experimental results are complemented by the MD calculations, which provide a qualitative description of the behavior of adsorbate molecule as temperature and surface coverage are varied. Excellent agreement is found between theory and experiment. These results are then compared to those of shorter-chain alkanes, and apparent deviations from trends relating thermodynamic properties and alkane chain length are explained in terms of molecule-surface compatibility.

In a separate investigation, inelastic neutron scattering measurements of rotational tunneling spectra of CH2D2 and CH3D are also presented in order to explore the effects of site and molecular symmetry on the rotational tunneling behavior of adsorbed methane monolayer solids. The experimental spectra are interpreted in terms of a pocket state model that accounts for these symmetries using a 12x12 Hamiltonian matrix. Diagonalizing this matrix produces a tunneling diagram that can be used to predict possible tunneling transitions. The experimental spectra are analyzed by comparing the widths and energy transfers of the observed spectral features. This analysis indicates a relatively simple spectrum for CH2D2 and a much more complicated spectrum for CH3D. These differences in complexity are explained by the complementary symmetry of the CH2D2 molecule and the interaction potential of the adsorption site as compared to the mismatch in symmetry between the CH3D molecule (threefold) and the speculation adsorption site (two-fold). Reasonably good agreement between theory and experiment is found for CH2D2/MgO, while the assumptions made in developing these models remain uncertain for the CH3D system.

TABLE OF CONTENTS

LIST OF TABLES

LIST OF FIGURES

CHAPTER I
THERMODYNAMICS OF N-NONANE AND N-DECANE ADSORBED ON MGO(100)

1.1 Adsorption Introduction & Background

1.1.1 Overview

The physisorption of molecular adsorbates onto metal oxide (MO) surfaces is pertinent to a diverse range of technological applications, including fluid separation and purifaction, gas storage, and catalysis. In addition to addressing fundamental theoretical questions, a more comprehensive understanding of adsorption properties vary with surface-molecule (S-M) compatibility could aid in the design of materials for these and other purposes. Studies that focus on surfaces and adsorbates with similar chemical characteristics but varying dimensions are useful for identifying trends in these properties. With this in mind, this chapter reports investigations of n-nonane and n-decane adsorbed films on the (100) face of MgO. The thermodynamics of both systems are examined using volumetric adsorption isotherms, and these experimental results supplemented with theoretical molecular dynamics simulations. These efforts are part of a larger inquiry into how the thermodynamic aspects of alkane adsorption on MgO(100) vary with chain length.

Following this overview, this section proceeds by defining terms commonly used in adsorption isotherm studies. A brief review of the theoretical development of three types of isotherms provides some historical context. Relevant characteristics of different categories of surface wetting are then discussed. Next, phase transitions between the familiar states of bulk matter (solid, liquid, & gas) are compared to those that occur in two-dimensional adsorbed films. This section ends with a literature review of previous investigations of alkane adsorption on MgO(100).

Section 1.2 provides details of the procedures used throughout this chapter. Details about the materials used for the adsorption isotherm studies are provided in addition to a description of the form and function of the isotherm apparatus. The procedures for collecting the isotherm data and setting up the molecular dynamics calculations are then outlined. Finally, molecular orientations with respect to the surface used to describe translational, rotational, and torsional motion are defined.

Section 1.3 demonstrates how thermodynamic quantities of adsorption can be calculated from volumetric isotherms using representative examples from nonane and decane on MgO. From the raw data, a single isotherm may be plotted in terms of the amount of gas adsorbed as a function of either the equilibrate adfilm vapor pressure or the difference in chemical potential between the 2D adfilm and the 3D condensed adsorbate. The Point B method of determining the monolayer capacity of the surface is shown, from which the area per molecule (APM) of the adsorbates is determined by comparison to methane isotherms. The locations of discreet layers are determined from the numerical derivative of the isotherm. A Clausius-Clapeyron analysis is then performed over the entire experimental temperature range in order to calculate the heat of adsorption, differential enthalpy, and differential entropy of each adsorbed layer. Next, a plot of the isosteric heat of adsorption as a function of coverage is presented for each system. Finally, the 2D isothermal compressibility and susceptibility—two quantities useful for determining the locations of 2D phase transitions--are defined, and representative plots of each are shown for both adsorbates.

Section 1.4 presents a more thorough discussion of the macroscopic isotherm data, and these are assimilated with qualitative microscopic visualizations and—when possible—quantitative analyses of the MD computations. Nonane and decane adsorbed films frequently exhibit similar behaviors that differ only by the temperature ranges at which they occur. In these cases, often results from only one of the two systems are depicted, but the

temperature variations for the remaining system are mentioned in the text. First, analysis of the isotherm derivative is used to ascertain the temperature ranges at which various 2D phases exist, and these are confirmed by inspection of the surface densities of the MD molecular trajectories. These are supplemented by images from the MD calculations performed at low temperature (≤160K), used to illustrate the minimum energy configurations for molecules at these coverages. Next, vertical M-M interactions coverages of 1, 2 and 3+ ML are considered by comparing the macroscopic isotherms results with molecular behavior in the MD simulations. Finally, a summary of the trend from 2D to 3D behavior with increasing coverage is provided.

The final section of this chapter compares these trends for nonane and decane to those of smaller alkanes in order to ascertain effects due to alkane chain length. Since these effects are intricately related to S-M compatibility, the section begins with a literature review of adfilms of spherical molecules in order to provide clues as to which thermodynamic quantities are significant when comparing the dimensions of the surface and adsorbate dimensional. These trends are then applied to the first and second adlayers of alkanes on MgO. At the conclusion of this chapter, the S-M compatibility effects of spherical admolecule diameter relative to the lattice constant are compared and contrasted with those due to the evolution of alkane molecular shape from spherical to linear. Finally, recommendations for future investigations of S-M compatibility effects are offered.

1.1.2 Adsorption Isotherm Terminology

Molecular *adsorption* occurs when the constituent molecules of a fluid phase adhere to the surface of another phase. It should not be confused with *absorption*, in which the molecules of the fluid permeate the surface phase (e.g. water in a sponge). The fluid phase is called the *adsorbate*, and the surface phase is often referred to as the *substrate* or *adsorbent*. A third phase is formed at the interface between the adsorbate and the surface—a thin film (*adfilm*) of adsorbed molecules (*admolecules*). For a planar substrate, molecular motion in

the direction normal to the surface is typically restricted, and the chemical and physical properties of the adfilm are often markedly different from those of the three dimensional (*bulk*) adsorbate. Monolayer coverage (denoted in moles as n_{ML} or in number of molecules as N_{ML}) occurs when the surface is completely covered by one layer of admolecules (or one *adlayer*). In many cases, one or more additional adlayers will form on top of first, with each adlayer having unique chemical and/or physical properties. The reverse process of adsorption occurs when admolecules leave the surface and rejoin the bulk. This is called *desorption*. Equilibrium between the adfilm and the bulk adsorbate occurs when the rate of adsorption equals the rate of desorption.

Adsorption can be loosely categorized as either *chemisorption* or *physisorption*. In chemisorption, electrons are transferred or shared between the adsorbate and the substrate. Conversely, in physisorption, the admolecules are bound to the surface by electrostatic forces often associated with intermolecular interactions (e.g. Van der Waals' forces, dipole attractions, etc.). Therefore, the amount of energy required to remove an admolecule from surface (the *binding energy*) is often used distinguish between chemisorption and physisorption. Chemisorbed molecules typically have binding energies on the order of chemical bond energies (~1-10 eV), while the binding energies of physisorbed molecules are on the order of those for bulk intermolecular forces (~10-100 meV).

In an adsorption isotherm, an adsorbed film (usually of a bulk gas) and the substrate are maintained at constant temperature. An initial amount of 3D adsorbate (n_i) is exposed to the substrate, and some of this initial amount (n_{ads}) adsorbs to the surface. The amount remaining in the 3D gas phase is determined by some extensive property of the gas (usually pressure). Once this amount has reached a constant value (n_f), the adfilm and the bulk adsorbate are assumed to be in equilibrium, and n_{ads} is assumed to be the difference between n_f & n_i. This process is repeated successively such that a plot of increasing n_{ads} versus pressure may be made. This representation constitutes an adsorption isotherm. If adsorption isotherms are recorded at several temperatures and the

area (*A*) of the surface is known, then the result is an equation of state for the 2D system [1]:

$$n_{ads} = n_{ads}(p, T, A). \quad \textbf{(1)}$$

Note that this is the two-dimensional analogue of the equation of state *n = n(p, T, V)* commonly used for three dimensional systems. The IUPAC system of classification recognizes six types of isotherms as shown in Figure 1 [2] (all figures are located in Appendix). The derivation of the functional form for isotherms of Types I, II and VI provides important historical context to the isotherms shown in later sections.

1.1.3 Theoretical Interpretations of Adsorption

Type I isotherms are representative of systems which follow the Langmuir equation [3]. Langmuir theory assumes that all adsorption sites are equivalent, and that interactions between adsorbate molecules are negligible. An adsorption site may host only one admolecule (i.e. only adlayer may form on the surface). Once the monolayer has completely formed, no more adsorption occurs, regardless of how high the pressure (*p*) is increased—note the plateau in amount adsorbed for a Type I isotherm. The rates of adsorption/desorption are proportional to the fraction of adsorption sites that are vacant/filled. At equilibrium, these rates are equal, and the Langmuir equation of state relating the fractional coverage (*Θ*) and pressure can be derived:

$$\Theta = \frac{b \cdot p}{1 + b \cdot p}. \quad \textbf{(2)}$$

The parameter *b* is a constant related to the relative rates of adsorption & desorption. Langmuir theory breaks down when the Gibbs free energy of adsorption is not constant, perhaps due to heterogeneity of the surface or

interactions between adsorbate molecules (both likely situations). Very few adsorption isotherms follow the Langmuir formalism past the first layer, and it is generally more applicable to chemisorption systems, where adsorbate-surface interactions are much greater than those between adsorbate molecules. Nevertheless, more advanced theories of adsorption incorporate aspects of Langmuir theory, and for this reason the development of the Langmuir equation is of great historical importance [4–7].

Brunauer-Emmett-Teller (BET) theory [8] overcomes some of the shortcomings of Langmuir's description by including the possibility of molecules adsorbing on top of other admolecules, i.e. allowing the formation of multiple layers. Each adsorbed layer is assumed to independently obey its own Langmuir equation. However, only the first layer is distinct from the bulk phase: The energy of adsorption/desorption for all subsequent layers is assumed to be equal to the energy of liquefaction/vaporization of the bulk. Once the saturation vapor pressure (SVP or p_0) of the adsorbate is reached, the number of adsorbed layers is infinite, appearing as a vertical asymptote in Type II isotherms as p approaches the SVP. By summing the contributions from all layers, the following equation of state can be derived:

$$\Theta = \frac{c \cdot (p/p_0)}{(1 - (p/p_0))(1 + (c-1)(p/p_0))}. \qquad (\mathbf{3})$$

The parameter c is dependant on the Gibbs free energy of adsorption. The BET equation above provides a reasonable model for many physisorbed systems and is commonly used to calculate the surface area of samples [4–7]. However, BET theory does not adequately describe systems in which layers beyond the first are thermodynamically distinct from the bulk.

Treatment of the second and subsequent adlayers is a significant shortcoming of the Langmuir and BET theories. As coverage increases, subsequent adlayers are further from the surface, and their interactions with the

surface grow increasingly weaker, adsorbate-adsorbate interactions play an increasingly important role. This is most clearly seen in Type VI isotherms, which show multiple steps corresponding to the formation of multiple layers.

Nonpolar molecules (such as nonane and decane) interact with other nonpolar molecules primarily through Van der Waals' (also called London dispersion) forces. These forces result when the electron cloud of one molecule induces a temporary electrostatic moment in the electron cloud of another molecule. These forces are always attractive and operate at intermediate and long distances. At extremely short distances, the electron clouds of two molecules begin to overlap, and the Pauli exclusion principle forces electrons to occupy higher energy levels. This results in a strong repulsive force between the two atoms. The competition between long-range attractive forces and short-range repulsive forces can be modeled as a function of the distance r between a pair of atoms within these molecules using the Lennard-Jones potential (V_{LJ}) [9]:

$$V_{LJ} = 4 \cdot \varepsilon \cdot \left[\left(\frac{\sigma}{r} \right)^{12} - \left(\frac{\sigma}{r} \right)^{6} \right]. \qquad (\mathbf{4})$$

The r^{-12} term describes the repulsive forces, while the r^{-6} term accounts for the attractive forces. A graphical representation of V_{LJ} (Figure 2) shows that these forces combine to form a potential well. The parameters ε & σ respectively correspond to the depth of this well and the distance at which the attractive and repulsive terms cancel. The minimum of this potential occurs at distance $r_m = 2^{1/6}\sigma$. Thus for any ensemble of admolecules, these pairwise L-J interactions between its constituent atoms can be summed over all surface and adsorbate atoms to give the total interaction potential.

Frenkel-Halsey-Hill (FHH) theory [10–12] applies this approach to each adsorbed layer. The repulsive forces are neglected at the interatomic distances associated with physisorption, and the attractive forces are assumed to depend primarily on the distance from the surface. By assuming that the distance from

the surface is proportional to the fractional coverage Θ, the FHH equation of state was derived [5–7]:

$$\ln\left(\frac{p_0}{p}\right) = \frac{k}{\Theta^3}. \qquad (\mathbf{5})$$

The term Θ^{-3} arises from integration of the r^{-6} attractive term. This equation predicts the stepwise appearance of Type VI isotherms. The amount adsorbed increases with p in a fashion similar to Langmuir or BET isotherms until the end of the first horizontal step signifying monolayer completion. At that point, a large amount of adsorbate may be added with little change in pressure as a second layer is formed. Subsequent layers may also form, exhibiting a horizontal plateau of the previous layer.

1.1.4 Surface Wetting

The behavior of a droplet of adsorbate on a surface is often described in terms of wetting. Dash has categorized the types of wetting into three classes [13]. In the complete wetting case (Class I), the droplet spreads out uniformly across the entire surface. For systems with incomplete wetting (Class II), the droplet spreads over a limited area before forming the bulk. For the extreme nonwetting case (Class III), bulk nucleation takes place immediately with little to no interaction with the surface. As shown in Figure 3, the approach of an isotherm towards SVP indicates the type of wetting present. For complete wetting, the surface directs the adsorption in a layer-like fashion. These layering steps are smoothed out as the distance of each layer from the surface increases, resulting in the appearance of an asymptotic approach to SVP. Isotherms corresponding to incomplete wetting look similar to those for complete wetting at low relative pressures, but show a sharp vertical break at SVP. In an extreme nonwetting system, no adsorption occurs, and the corresponding isotherm is vertical at SVP and perfectly horizontal at lower pressures.

1.1.5 3D versus 2D Phase Transitions

A phase diagram between the three states of 3D matter shows the phase in which a substance exists in terms of two of the three thermodynamic parameters that define its equation of state. Curves along the phase diagram show values of these two parameters at which two phases can coexist. A phase transition can be characterized using an order parameter—a parameter that is markedly different between the two phases in question. The Ehrenfest classification of phase transitions categorizes phase transitions by the discontinuity of their derivatives of their order parameter with respect to Gibbs free energy (i.e. chemical potential). First order transitions are discontinuous in their first derivative, while second order transitions are continuous in their first derivative but discontinuous in their second [14].

For example, if the equation of state for a bulk substance is described in terms temperature, pressure, and density, the liquid and gas phases are seen to coexist at relatively low temperatures and pressures (cf Figure 1.1(a) in Reference [15]). Below these values, the density of the gas phase is markedly distinct from that of the liquid phase at constant temperature and pressure, therefore density is the order parameter for the 3D liquid-gas phase transition. Below the critical temperature, the density plotted against temperature is discontinuous, i.e. the liquid↔gas transition is first order. The curve separating the liquid and gas phases (the vapor pressure curve) terminates at the critical point defined by the critical values of those parameters. As the critical temperature and pressure is approached, the difference between the density of the gas and the density of the liquid approaches zero (cf Figure 1.2(a) in Reference [15]). Above, the critical point, the liquid and gas phases can no longer be distinguished by their densities, and the phase is said to be a supercritical fluid. The transition from gas-liquid coexistence to a supercritical fluid is second order, because the density has an inflection point at the transition temperature instead of a discontinuity.

Molecules within the adfilm can exist in phases analogous to those of three dimensional substances. Ideally, these phases are two dimensional because they exist only within a given adlayer, and any motion of the constituent admolecules is confined to the surface plane. Admolecules in the 2D gas phase have a long mean free path (i.e. rarely collide) and are translationally mobile on the surface. Admolecules within a 2D liquid tend to cluster together while remaining their mobile. Within a 2D solid, however, these clusters remain more or less stationary on the surface. In clumsy accordance with the analogy to three dimensions, comparable behavior to the continuous 3D supercritical transition occurs above a critical temperature (T_{2c}) at which the 2D gas and 2D liquid become indistinguishable.

The vertical risers of a stepwise isotherm usually represent a path followed along a 2D phase diagram within the corresponding adlayer. At the bottom of the riser, most (if not all) of the topmost admolecules are in a 2D gas phase. As molecules are added and one moves up the riser, a 2D condensed phase (either solid or liquid) forms at the expense of the 2D gas. At the top of the riser nearly all admolecules are in the condensed phase [16]. If one performs a series of isotherms at appropriate temperatures, a complete phase transitions can be constructed. For example, the shape of the riser may deviate from verticality as the temperature is increases. This behavior could indicate a transition from a 2D liquid-gas coexistence to a 2D supercritical phase. This transition has been extensively studied for noble gases on metal chloride surfaces of varying lattice constants [17–20]. Other systems, such as xenon and krypton on graphite [21,22], exhibit a substep just before completion of the first monolayer corresponding to a transition between two condensed phases (i.e. a 2D solid and a 2D liquid). Figure 4 [16] shows a phase diagram constructed from such a series of isotherms.

1.1.6 Alkane Adsorption on MgO(100)

Adsorbed methane films on MgO powders have been extensively studied using adsorption isotherms and other techniques. This system is of interest due to the close match between molecular diameter and lattice constant (4.16 & 4.21 Å, respectively). If an MgO(100) sample is exceptionally uniform, as many as 7-8 layers are visible on isotherms performed around 77K (see Figure 5 [23]). The molar enthalpies and entropies of each adsorbed layer converge to the bulk values as coverage increases, and a phase transition observed at 80 K for the first layer is attributed to the melting of the 2D solid into a 2D liquid [24]. Below this temperature, neutron scattering studies have revealed that the monolayer forms a $\sqrt{2}x\sqrt{2}R45°$ (alternatively denoted C(2x2)) crystal structure commensurate with the surface [25,26] in agreement with theoretical predictions [27–29]. Other studies at multilayer coverages have shown that the rotational dynamics of individual molecules evolve in a layer by layer fashion, with bulk-like behavior beginning in the fourth layer [23,30].

The isotherms of longer n-alkanes through octane have also been studied in order to examine the effects of chain length and adsorbate-surface compatibility. Ethane isotherms show three distinct layers [31], while only two layers are visible for propane through octane [32,33]. Like methane, the molar enthalpies and entropies of all of these adsorbates approach bulk values of vaporization as the number of layers increases. Unlike methane, no first layer 2D melting transition is attributed to any of these alkanes due to the higher temperatures at which these experiments were performed. Instead, at temperatures well above the bulk melting point, these studies identify a 2D liquid→supercritical fluid transition within the first layer.

1.2 Procedural Details

1.2.1 Materials

N-nonane and n-decane (C_9H_{20} and $C_{10}H_{22}$) are straight-chain alkanes produced primarily from the refinement of petroleum. Relevant standard thermodynamic data [34] for these two compounds are provided in Table 1.

Table 1. Relevant standard thermodynamic data for adsorbates.

	n-nonane	**n-decane**
T_{boil} (K)	423.8	447.2
T_{fus} (K)	219.5	243.3
T_{triple} (K)	219.6	243.4
T_c (K)	595.	617.8
$\Delta H_{vap}°$ (kJ*mol^{-1})	46.43	51.38
$\Delta°H_{sub}$ (kJ*mol^{-1})	71.4	80.3

The n-nonane and n-decane used in this work were obtained from *Acros Organics* and of purity greater than 99%. The adsorbates were then transferred under argon into separate stainless steel cylinders fitted with *Swagelok* bellows valves. Before use, the adsorbates were subjected to several freeze-pump-thaw distillation cycles to remove any dissolved gaseous impurities. This consisted of freezing the alkane in a liquid nitrogen bath, pumping the headspace of the frozen alkane under high vacuum, and allowing the alkane to thaw and reliquefy. This process was repeated until the vapor pressure of the frozen alkane was less than 10^{-4} torr (typically 4-5 cycles). This process was repeated on a monthly basis. Warmer temperature baths (but still below the triple point of the adsorbate) were also tried, but no improvement in the baseline vapor pressure or isotherm quality was observed.

The MgO nanocubes used in this study were produced using the Kunnman-Larese method [35], which produces particles of narrow size distribution (250 ± 30 nm), large surface area (~10 m^2g^{-1}), and almost complete exposure of the (100) face (TEM image shown in Figure 6). The procedure for preparing and loading the MgO samples has been described in detail in previous studies [36,37]. In summary, the material was heat-treated under vacuum at 950°C for 36 hours prior to use. Following heat treatment, care was taken to minimize the exposure of the sample to the atmosphere. The MgO was transferred in an argon-filled glove box to copper sample cell which was then sealed with an indium wire gasket.

1.2.2 Apparatus

The apparatus for conducting the adsorption isotherms consisted of two parts: a system for controlling the temperature of the sample cell and a computer automated gas handling system (GHS). The setup has been detailed elsewhere [38] and is illustrated in Figure 7. All adsorption experiments were controlled using the ISO-LAB program programmed using LABVIEW software on an Apple Mac mini.

The sample cell was thermally insulated from the outside environment by a vacuum jacket. A helium compressor and expander (ARS m/n 2HW & DE202 respectively) were used to continuously cool the sample, while a resistance heater linked to a PID temperature controller (LTC-21, Neocera) simultaneously heated the sample to the desired temperature. The temperature controller was connected to the ISO-LAB interface and monitored the temperature using a Pt resistance thermometer. This setup was capable of maintaining sample temperatures as low as 10K or as high as 300K to within ± 5 mK.

The GHS consisted of ¼ inch stainless steel tubing and Swagelok bellows valves. The sample cell was connected to a calibrated dosing volume (V_{dose}), which in turn was connected to a gas reservoir, a turbo pump, and two MKS manometers (maximum pressure readings: 1 & 100 torr). All automated valves

are controlled from the ISO-LAB interface via a pressure control box built in-house. ISO-LAB allows complete automation and remote control throughout the entire course of an isotherm. The process for collecting a single data point is as follows: An amount of gas of a known pressure (p_i) is introduced into the dosing volume. The automated valve to the sample cell (V_1) is opened, exposing the aliquot of gas to the cooled sample. The pressure corresponding drops as the gas expands and is adsorbed onto the sample. Once the pressure has equilibrated (as determined by an algorithm within ISO-LAB), V_1 is closed. ISOLAB then records the equilibrated pressure (p_f) and the sum of the current and all previous pressure drops ($\Sigma\Delta p$). This procedure may be repeated 100+ times during the course of one adsorption isotherm.

1.2.3 Collection of Isotherm Data

In order to evaluate the isotherm data, several data reduction steps were performed using Kaleidagraph from Synergy Software. First, the volume of the 3D vapor phase within the sample cell must be known. This volume—also termed as the dead space or V_{dead}—consists of the cell volume not occupied by the MgO sample itself. Following the loading of the sample, aliquots of helium gas were expanded from the dosing volume into the cell. The dead space was calculated from the corresponding pressure drop by applying Boyle's Law.

Once the dead space has been determined, a methane isotherm at ≈77K was performed to characterize the quality of each MgO sample (see Figure 8). A high quality sample of MgO(100) nanocubes will typically show five or more steps of equal height. This provides an excellent gauge of the uniformity of the particle size and adsorption potential, since any variations will be reflected in the molecular density of the adsorbed layers [24]. These isotherms were later used to determine the surface area of the sample.

Approximately twenty isotherms were performed with each adsorbate, spanning temperature ranges of approximately 230-280 K for nonane and 250-290 K for decane. In order to prevent the premature formation of the bulk

adsorbate, the capillary leading from V_1 to the sample cell was gently heated with a resistance heater, and the difference initial dosing pressure and the previous equilibration pressure (shot size) was kept below half of the estimated SVP. At lower temperatures, this often necessitated shot sizes of less than 10 mtorr. The SVP drops to less than 1 mtorr for these adsorbates as the triple point is approached; therefore the lower bound of feasible experimental temperatures was restricted by the resolution (10^{-5} torr) of the 1 torr manometer. The dosing volume was kept at room temperature, constraining the upper limit of temperatures at which isotherms could be performed. The isotherms were allowed to continue until the final equilibrated pressure reached saturated vapor pressure (SVP). An important note: the SVP was used in conjunction with the semi-empirical Antoine equation parameters [34] to determine the sample temperature of each isotherm.

Between nonane/decane isotherms, CH_4 isotherms were performed to monitor the quality of the sample. A significant degradation of the sample was noticed after three nonane/decane isotherms, after which the sample was replaced. Due to the relatively small shot sizes and long equilibration times (45-60 minutes), one nonane/decane isotherm typically required about one week to run.

1.2.4 Molecular Dynamics Setup

In order to supplement the macroscopic isotherm data with a microscopic representation of the dynamics of adsorption, a series of molecular dynamics calculations were performed using software from *Accelrys Software Inc*. These calculations were performed using the Forcite program module, and visual representations of the results were displayed and manipulated using Materials Studio, 6.0. Forcite can be used to perform a wide range of tasks by approximating the potential energy field of atoms, molecules, and periodic structures using a classical forcefield. Quantum effects are neglected, allowing

the determination of bulk properties of large systems (> 1000 atoms) while using a reasonable amount of computational resources [39].

The calculations herein were performed using Forcite's *Dynamics* option, which calculates the time-dependent trajectories of structures using Newton's laws of motion. The COMPASS forcefield [40] was used to define the interatomic potentials, and the trajectories of adsorbed nonane and decane films were calculated in 1.0 fs time steps.. The NVT ensemble in which the number of molecules, volume, and temperature are held constant was used. The temperature for each simulation was regulated by an NHL thermostat [41]—a modification of the Nosé thermostat [42]. In addition to the Nosé parameter Q, the NHL thermostat contains a parameter γ to account for random fluctuations in Q. This parameter improves the performance of the thermostat, especially when the initial structure is far from thermal equilibrium [39,43]. Within Forcite, γ is expressed as a decay constant $1/\gamma$. A wide range of decay constants and Q values were tested to see which combination allowed the temperature to steadily approach the setpoint before equilibrating. A decay constant of 0.1 ps and Q = 0.1.were determined to be optimal and were subsequently used throughout the course of the simulations.

An MgO slab with periodic boundary conditions and lattice parameters $a = b$ = 67.38 Å, c = 10.53 Å was constructed and cleaved such that only the two (100) faces of the *ab* plane was exposed. The area of the substrate available for adsorption was therefore 9080 Å^2. A vacuum slab was added in the *c* direction such that it extended an additional 30 Å beyond each *ab* face. In order to explore the coverage dependence and determine the nominal monolayer capacity (N_{ML}) of the slab, a series of dynamics calculations with varying numbers of adsorbed molecules were performed, and N_{ML} was taken to be the coverage at which molecules just begin to populate the second layer at low temperature (< 200 K). The results are summarized in Table 2. The resulting APM's were calculated to be much lower than what was determined

experimentally. Presumably this is because the isotherms were performed at a much higher temperature than that at which the MD calculations were run.

Table 2. MD APM Results.

	N_{ML} (molecules)	MgO Surface Area (Å^2)	APM (Å^2/molecule)
Nonane	140	9080	64.9
Decane	125	9080	73.2

A series of MD calculations of gradually decreasing temperature would then be performed. In a typical simulation, the number of adsorbate molecules corresponding to the desired coverage were placed on the surface, and a rough energy optimization was performed (typical convergence criteria: energy = 0.001 kcal/mol, displacement = 0.001 Å). A high temperature (T = 300-350 K) dynamics calculation would then be performed on the optimized structure. The temperature setpoint would then be lowered by a set interval (10-30K), and last frame of the calculation used as the input for the next. This was intended to allow admolecules to explore the entire surface and to prevent the system from getting trapped in a local minimum. The coverage and temperatures at which these calculations were performed is summarized in Table 3.

Table 3. Summary of Decreasing Temperature Simulations.

Coverage	Temperature Range	Temperature Increment
0.7 ML	100 - 350 K	10 K
1.0 ML	160 - 300 K	20 K
2.0 ML	270 -300 K	30 K
3.0 ML	300 K	n/a

Every 100th calculated structure from the trajectory of the MD simulations was saved, allowing a frame-by-frame structural comparison of the systems in 0.1 ps

time steps. These results were converted into video files for visual inspection. The still-frames and videos were viewed from two perspectives. The top view (looking down on one face of the MgO slab), allows observation of the lateral interactions between admolecules. This is most useful at monolayer and submonolayer coverages for identifying which 2D phases are present as well as determining minimum energy orientations of molecules with respect to the surface. The side view allows the observation of admolecule motion and orientation perpendicular to the surface. This view is useful for observing trends such as multilayer occupation or the tendency to exhibit bulk-like properties at higher coverages.

Since nonane and decane contain more torsional degrees of freedom (tdf) than smaller, distortions of the carbon backbone were quantified using the *Analysis→Torsion Distribution* function within Forcite. This module tracks all possible dihedral angles formed by four connected atoms over all specified output frames. It then tabulates these results by a user-specified bin width (1 ° in this work) and provides the distribution function of the dihedral angles as a fraction. In this manner, the temperature dependence of the tdf's was quantified for both systems over the 100-350K temperature range of simulations at 0.7 ML.

1.2.5 Definition of Molecular Orientations

Within this work, the orientation of an alkane admolecule with respect to the surface will be described by that of its carbon backbone (cbb). If there is no reorientation about a C-C single bond within a molecule (i.e. the cbb lies within a single plane), then two cbb axes can be defined as in Figure 9. The major axis extends the entire length of the molecule, while the minor axis lies perpendicular to the major axis. Each of these axes may orient itself independently with respect to the surface, and they will be examined separately.

Regarding the minor axis, the cumulative distance between adsorbate hydrogen atoms and the surface is minimized at high symmetry orientations (i.e. when it is either parallel or perpendicular to the surface). These should

correspond to minimum energy configurations, as the Van der Waals attraction should be the greatest. In Figure 10, all possible orientations with the nonane and decane minor axes parallel and perpendicular to the surface are shown. These are denoted by the number of carbons in the plane parallel to the surface. Due to the different cbb symmetries for odd- versus even-numbered alkanes, there are two distinct orientations for decane (C5 and C10), whereas there are three for nonane (C4, C5, and C9).

Regarding the major axis, there are two surface parallel orientations of high symmetry in the ‹10› and ‹11› directions along the crystal face. If the molecular center of mass is at a surface site of four-fold symmetry, then the 45° arc bounded by these two vectors is sufficient to cover all unique major axis orientations. Because the molecular footprint of these long alkanes spans multiple unit cells of the substrate, intermediate orientations of the major axis may result in local minima with respect to the surface potential.

If one assumes that the alkane molecules are rigid, then the MD simulations would be dominated by three rotational and translational degrees of freedom that become increasingly active as the temperature is increased. However, if one accounts for the free rotation about C-C bonds introduces additional torsional degrees of freedom are possible (hereafter tdf) in all but methane. Assuming all bond angles remain fixed, ethane has one such tdf formed by the dihedral angles of the planes formed by the H-C-C and C-C-H bonds. Propane has two tdf's between the C-C-C plane and the two C-C-H planes; and so on. The number of tdf's (n-1) increases linearly with chain length (n). Beginning with butane, tdf's formed by planes defined entirely by carbon atoms begin to be seen. Since this requires four C atoms, butane only has one such tdf, and n-alkanes have n-3. Therefore, nonane and decane have 6 and 7 cbb tdf's respectively, and these appear as distortions of their cbb in the videos.

Molecules molecules that differ only by the torsion angle about a single bond are referred to generally as conformers and specifically as rotamers. Although rotation about a single bond is relatively unhindered, certain molecular rotamers

minimize steric hindrance of substituents and thus correspond to conformations of rotational minimum energy. For ethane and terminal methyl groups on larger alkanes, these torsional minima are termed the staggered conformation and occur when the three hydrogen atoms bonded to one carbon are rotated 60° with respect to substituents on the neighboring carbon atom. For n-alkanes with cbb tdf's, two staggered conformations are possible: the anti conformation with a cbb torsion angle of 180°, and the two gauche conformations that are rotated 120° in either direction from the anti conformation. The anti conformation is the global energy minimum and the gauche conformations are local minima.

1.3 Isotherm Analysis

1.3.1 Moles Adsorbed and Chemical Potential

The moles of gas adsorbed n_{ads} can be calculated from p_f, $\Sigma\Delta p$, V_{dose}, V_{dead}, the temperature of the room (T_{room}), the temperature of the sample (T_{sample}) and the ideal gas constant R:

$$n_{ads} = \frac{\Sigma\Delta p \cdot V_{dose}}{R \cdot T_{room}} - \frac{p_f \cdot V_{dead}}{R \cdot T_{sample}}. \quad \textbf{(6)}$$

The above equation assumes that the nonane and decane vapor behave as ideal gases. Isotherms were also analyzed using Van der Waals and virial equations of state with negligible differences calculated for n_{ads} (~0.1% at the highest equilibration pressures). Figure 11 and Figure 12 show respective representative nonane and decane isotherms as well as their numerical derivatives. Two adsorption steps are observable in each isotherm, corresponding to the formation of the first and second layers. For all isotherms, these two layering features were clearly observed as steps in the raw data and as peaks in the numerical derivative; although the second step becomes less pronounced at higher temperatures. The locations (in terms of p_f) of these transitions were determined by fitting Lorentzians to the numerical derivative peaks (see Figure 13). After the first layer, the adsorption isotherms trend upward as SVP is approached, and the second step appears on this upward curve. The derivative likewise trends toward infinity as p_f approaches SVP, distorting the peak corresponding to second layer formation. Therefore, this background was fit to an exponential growth curve and subtracted from the second layer peaks prior to Lorentzian fitting.

At p_f, the 2D surface film and the 3D vapor are assumed to be in equilibrium, i.e. their chemical potentials are assumed to be equal. If all adsorbate vapors

are assumed to behave as ideal gases, then the chemical potential difference between the adsorbed film and the bulk condensed adsorbate ($\mu - \mu_0$) may be calculated from p_f:

$$\mu - \mu_0 = R \cdot T \cdot \ln\left(\frac{p}{p_0}\right). \quad \textbf{(7)}$$

In the above equation, p_0 is the SVP of the bulk, T is temperature, and R is the ideal gas constant (8.314 $J*K^{-1}*mol^{-1}$). In Figure 14 and Figure 15, the same two adsorption curves are plotted against $\mu - \mu_0$ rather than p_f. Note that since chemical potential is the logarithm of pressure, the abscissa axis is expanded at low values and contracted at high values.

1.3.2 Monolayer Capacity and APM

The monolayer capacity, n_{ML}, was previously defined as the moles of gas required to completely cover the substrate with one layer of adsorbate. This quantity was determined for all isotherms using the so-called Point B method [5]. Figure 16 illustrates this procedure for the first step of a CH_4/MgO isotherm at 77K. Linear regression fits are applied to both the initial vertical riser and the first horizontal step of the isotherm. The ordinate value of the intersection of these two fits is n_{ML}. This was done for all isotherms in this study. As mentioned previously, the CH_4 isotherms were performed on each sample prior to any nonane/decane isotherms. CH_4 is known to form a commensurate monolayer on the MgO surface with an area per molecule (APM_{CH4} = 17.74 $Å^2$ [25]), hence the surface area of the sample (*SA*) can be easily calculated:

$$SA = n_{ML} \cdot N_A \cdot APM, \quad \textbf{(8)}$$

where N_A is Avogadro's number. The surface area of the sample is presumably constant throughout the course of subsequent isotherms, therefore the APM for nonane/decane can be calculated:

$$APM_{adsorbate} = \frac{n_{ML,\,CH4}}{n_{ML,\,adsorbate}} \cdot APM_{CH4}. \qquad (9)$$

Using the above equation, the average APM was calculated to be 124.7 ± 4.6 Å^2 for nonane and 250 ± 12 Å^2 for decane. No trend in the variation of APM with temperature was observed (Figure 17), arguing against the presence of a low- to high-density condensed phase transition within this temperature range.

1.3.3 Clausius-Clapeyron Analysis

For a phase transition involving condensed phase and a vapor phase in equilibrium, the pressure of the vapor phase (p) can be related to the temperature (T) and the enthalpy of the transition (ΔH_{trans}) using the Clausius-Clapeyron equation:

$$\frac{dp}{dT} = \frac{p \cdot \Delta H_{trans}}{T^2 \cdot R}. \qquad (\mathbf{10})$$

Here, if ΔH_{trans} is assumed to be constant over a given over a given interval of p and T, then the above equation can be integrated to give the following relation:

$$\ln(p) = -\frac{\Delta H_{trans}}{R \cdot T} + \frac{\Delta S_{trans}}{R}, \qquad (\mathbf{11})$$

where the change in entropy of the transition (ΔS_{trans}) appears as an integration constant.

For all nonane/decane isotherms, the numerical derivative with respect to p_f was plotted. As shown earlier, adsorption features appearing as steps in a raw isotherm are peaks in its derivative. The first and (background-subtracted) second layer derivative peaks were fitted to Lorentzian functions (example in Figure 13), and the peak center is presumed to correspond to the pressure of individual layer formation (i.e. the inflection point of the isotherm). The natural logarithms of these pressures as well as the SVP's are plotted against inverse temperature in Figure 18 & Figure 19, and a linear regression of the following form is applied:

$$\ln\left(p_n\right) = B^{(n)} - \frac{A^{(n)}}{T}, \tag{12}$$

where n = 1, 2, & ∞ designates respective values for the first layer, second layer, and bulk adsorbate. Using the equations below, the heat of adsorption (Q_{ads}), the differential enthalpy ($\Delta H^{(n)}$), and the differential entropy ($\Delta S^{(n)}$)for each layer were calculated:

$$Q_{ads} = R \cdot A^{(n)}. \tag{13}$$

$$\Delta H_{(n)} = -R \cdot \left(A^{(n)} - A^{(\infty)}\right). \tag{14}$$

$$\Delta S_{(n)} = -R \cdot \left(B^{(n)} - B^{(\infty)}\right). \tag{15}$$

The heat of adsorption represents the enthalpy change in forming a given layer from molecules in the gas phase. Since this process is always exothermic, the sign is typically ignored, and only the magnitude of Q_{ads} is given. Q_{ads} should not be confused with the differential enthalpy $\Delta H^{(n)}$, which is the difference in enthalpy between a given layer and the bulk phase. The sign for $\Delta H^{(n)}$ is crucial, as it indicates which phase is enthalpically favorable (negative if the adsorbed layer is favored, positive if the bulk phase is favored. The reverse is true for the

sign of $\Delta S^{(n)}$ (negative if adsorbed layer is entropically favored, positive if bulk is favored). These values for both systems are summarized in Table 4 & Table 5.

Table 4. Clausius-Clapeyron thermodynamic values (nonane).

n	$A^{(n)}$	$B^{(n)}$	Q_{ads}	$\Delta H^{(n)}$	$\Delta S^{(n)}$
1	4471	11.746	37.17	9.83	71.23
2	5683.9	19.832	47.26	-0.25	4.01
∞	5653.9	20.314	47.01	n/a	n/a
units	K	none	$kJ*mol^{-1}$	$kJ*mol^{-1}$	$J*K^{-1}*mol^{-1}$

Table 5. Clausius-Clapeyron thermodynamic values (decane).

n	$A^{(n)}$	$B^{(n)}$	Q_{ads}	$\Delta H^{(n)}$	$\Delta S^{(n)}$
1	2993.3	5.2199	24.89	23.40	119.46
2	5849.9	19.196	48.64	-0.35	3.27
∞	5807.8	19.589	48.29	n/a	n/a
units	K	none	$kJ*mol^{-1}$	$kJ*mol^{-1}$	$J*K^{-1}*mol^{-1}$

1.3.4 Isosteric Heat of Adsorption

The isosteric heat of adsorption (Q_{st}) signifies the amount of work required to bring one adsorbate molecule from the 3D vapor into the 2D adsorbate film. It is defined thusly [1]:

$$Q_{st} = R \cdot T^2 \cdot \left(\frac{\partial \ln(p)}{\partial T} \right)_{\Theta}, \qquad (\mathbf{16})$$

where the derivative is taken at constant coverage Θ. It is distinct from Q_{ads} in that Q_{ads} describes that heat for the formation of an entire layer, whereas Q_{st} can indicate the heat at any point during layer formation. Q_{st} can be calculated from two closely spaced isotherms by approximating the partial derivative as $\Delta \ln(p)/\Delta T$, where ΔT ~ 1-2 K [24]. Because Θ is a dependent variable for these

isotherm measurements, it is virtually impossible to obtain two isotherms with data points at precisely the same coverage. Therefore, it is necessary to interpolate values from the experimental data. Figure 20 shows Q_{st} as a function of Θ for nonane and decane adsorbed on MgO.

Due to the aforementioned approximations and the extreme slopes of the first steps of these isotherms, the exact calculations at low coverages are often quantitatively unreliable. For example, Q_{st} should always be positive, yet for nonane it is calculated to be negative over the range $0.75 < \Theta < 0.95$. Nevertheless, Figure 20 provides a useful qualitative comparison of these systems. Both curves show local maxima as the first and second layers begin to form. Moreover, these maxima are higher for nonane for the first layer and for decane in the second layer, in agreement with the Q_{ads} values calculated from the Clausius-Clapeyron plots (Figure 18 & Figure 19). At $\Theta > 8$, these Q_{st} converges to values of 46 & 58 $kJ*mol^{-1}$ for nonane and decane, respectively. Table 6 compares these values to the bulk enthalpies of vaporization ΔH_{vap} [34] at these respective temperatures. Agreement is within 5% for nonane and 10% for decane. Considering that the temperatures of the Q_{st} plots fall outside of the range for which the literature values of ΔH_{vap} are calculated, this agreement is excellent.

Table 6. Comparison of Qst & ΔHvap.

	Temperature	**Q_{st} ($\Theta > 8$)**	**ΔH_{vap} (bulk)**
Nonane	275.34	46	48.0
Decane	285.74	58	52.3
Units	K	$kJ*mol^{-1}$	$kJ*mol^{-1}$

1.3.5 2D Isothermal Compressibility and Susceptibility

The widths of the isotherm derivative peaks can be used to determine the location of phase transitions, and several related physical quantities have been

used for this purpose. One such quantity is the 2D isothermal compressibility, which is a measure of the change in the surface area occupied by the adsorbate in response to changes in 2D spreading pressure. It is defined in [24] as:

$$K_{2D} = \frac{A \cdot p}{N_A \cdot k_B \cdot T \cdot N^2} \cdot \frac{dN}{dp}, \qquad \textbf{(17)}$$

where A is the surface area of the sample, k_B is the Boltzmann constant, N_A is Avagadro's number, and N is the total number of adsorbate molecules. Like the raw numerical derivative of an isotherm, layer formation appears as a peak in. Figure 21 & Figure 22 show two K_{2D} plots for nonane and decane on MgO. Note that the peaks are weaker and broader at higher temperature. This effect is less pronounced for the second layer peak than the first.

The derivative of the order parameter with respect to change in free energy (i.e. chemical potential) is the susceptibility (χ). As mentioned in Section 1.1, for 3D phase diagram of density (ρ) and temperature, the order parameter for liquid-gas transition is ρ. The 3D susceptibility would therefore be $(\partial\rho/\partial\mu)_T$ [44]. For the 2D liquid-gas phase transition the area density is directly proportional to the fractional coverage Θ [45],such that:

$$\chi_{2D} = \left(\frac{\partial \Theta}{\partial \mu} \right)_T. \qquad \textbf{(18)}$$

This quantity is related to the isothermal compressibility by a factor of Θ, and both have been used to identify phase transition temperatures of adsorbed films [45–47]. The susceptibility was calculated over the entire range of each nonane and decane isotherm. Figure 23 shows the first layer susceptibility peaks for seven representative nonane and decane isotherms. Note the evolution from tall, sharp peaks to shallow, broad ones as the temperature is increased. The susceptibility peaks corresponding to second layer formation (not

shown) all occurred at chemical potentials much closer to the bulk ($\mu - \mu_0 = -1.3 \pm 0.2$ kJ*mol^{-1}) and were significantly broader over the entire temperature range.

1.4 Comparison of Isotherms to Molecular Dynamics Results

1.4.1 2D Phase Transitions

Given the dominance of lateral adsorbate motion and the absence of vertical adsorbate-adsorbate interactions, any phase transitions at submonolayer coverage should be two dimensional in nature. The 2D triple point typically occurs ~$0.7 \cdot T_{triple,3D}$, while the 2D critical temperature of condensation (T_{2C}) typically occurs around ~$0.4 \cdot T_{3C}$ for the first layer of physisorbed films [48]. All of the isotherms reported here were performed well above the bulk triple point; therefore observing any transitions involving a 2D solid phase is unlikely. However, the experimental temperatures are in the ideal range for determining T_{2C}.

Figure 24 shows the first monolayer of decane plotted against chemical potential. At the lowest temperature (red curve), the slope is nearly vertical, indicating liquid-gas coexistence and a 2D condensation transition. At the base of this riser, adsorbed molecules behave as a 2D gas, although there are insufficient low-coverage data points to clearly identify this behavior. As adsorbate is added, the average distance between admolecules decreases to the point that the 2D condensed phase begins to form. As the coverage increases further up the vertical riser, the fraction of the surface covered by 2D liquid grows at the expense of the fraction covered by 2D gas according to a leverage rule. The gas and liquid are in equilibrium (i.e. $\mu_{gas} = \mu_{liquid}$), hence a significant amount of adsorbate can be added with little change in chemical potential. At the top of the riser, the entire surface is covered by the condensed phase. With the addition of more molecules, the chemical potential rises, signaling that an increase in pressure is needed to form a second layer. Note that this occurs before the monolayer is completed at $\Theta = 1$, meaning that molecules begin to occupy the second layer prior to completion of the first.

Contrast this with the isotherm at the highest temperature (brown curve). There is no vertical riser to separate two distinct phases, i.e. the derivative with

respect to chemical potential with coverage is continuous. No 2D liquid and 2D gas phases can be distinguished, suggesting that the adsorbate may be in a supercritical phase throughout. Presumably, T_{2C} lies somewhere within this temperature range. The exact this transition temperature cannot be determined from Figure 24, since none of the isotherms are perfectly vertical (suggesting that 2D condensation in this system may not be first order).

With this potentially continuous phase transition in mind, one considers what is needed in order to determine the critical temperature. Here the susceptibility (i.e. the derivative) of the order parameter Θ is examined. Below T_{2C}, the region of where the 2D gas and 2D liquid coexist (the vertical riser) covers a large interval in coverage and narrow interval in chemical potential, resulting tall narrow peaks in the susceptibility (see top plot of Figure 23). As T_{2C} is approached, the coexistence region covers a steadily decreasing range of coverages, but the difference in chemical potential remains mostly unchanged, so the widths of the susceptibility peaks remain relatively constant. At T_{2C}, the coexistence region disappears, and the susceptibility peaks begin to broaden. In the top plot in Figure 25, the half-width-at half-maximum (HWHM) of the first layer susceptibility peaks for both decane and nonane are clearly seen to linearly diverge past a threshold temperature. A piecewise curvefit containing parameters T_{2C}, b, & m is applied to each set of HWHM versus temperature data:

$$\begin{aligned} &\text{If } T < T_{2C}, \quad \text{HWHM} = b; \\ &\text{If } T > T_{2C}, \quad \text{HWHM} = b + m \cdot T. \end{aligned} \tag{19}$$

From these fits, T_{2C} is determined to be 263.04 ± 1.36 K for the first adlayer of nonane and 277.77 ± 1.72 K for the first adlayer of decane. The bottom of Figure 25 shows a similar plot for the second adlayer of each system. Here the susceptibility HWHM increases linearly over the entire temperature range for both nonane and decane. Therefore, the second adlayer might be in a 2D supercritical phase throughout this temperature range, and the corresponding T_{2C}

would be lower than the lowest temperature isotherm for each system (230.89 ± 0.03 K for nonane & 251.59 ± 0.04 K for decane).

The MD simulations at 0.7ML coverage confirm the presence of T_{2C} near these temperatures. A supercritical phase was identified at the highest temperatures for each system, and as the temperature was lowered, both systems formed a 2D condensed phase. This transition is evident by examining the homogeneity of the density of the surface film, as shown in the snapshots in Figure 26. At 350K for both systems, the surface density is relatively uniform, and any local irregularities fluctuate randomly. At lower temperatures (250K for nonane and 260K for decane), the admolecules have clearly formed a condensed, leaving of large patches of uncovered surface. These vacant regions were seen in the videos correspond to a 2D gas: Occasionally, an admolecule will break away from the condensed phase and travel through the unoccupied regions before rejoining the condensed phase. Further inspection of the video files narrows the possible temperature ranges of T_{2C} to 270-290K for nonane and 280-300K for decane. The agreement of the lower bounds of these ranges with experiment is excellent.

The identity of this condensed phase was confirmed to be a 2D liquid by monitoring the evolution of the adlayer with time. Video clips at these temperatures showed the covered regions moving around the surface. This can also be seen by comparing the first and last frame of these simulations, as in Figure 27. As the temperature is lowered, the translational molecular motion decreases, and the molecules eventually settle into potential energy minima on the surface to form a 2D solid. This is illustrated at 100K for both systems in Figure 28. Note that the positions of the covered/uncovered surface regions do not change over the 50ps time interval between the initial and final frames. In this case, the possible ranges of the melting transition temperature was narrowed to 170-230K for nonane and 210-260K for decane by examining the video files. Again, the lower bound of these ranges is likely a better indicator of the true

transition temperature, given that they correspond to ≈0.77 and 0.86 times the respective bulk melting points for nonane and decane.

1.4.2 Submonolayer Molecular Configurations

At monolayer and submonolayer coverages, videos over the entire temperature range showed the carbons backbones of both systems remained predominantly flat on (i.e parallel to) the surface, confirming that adsorbate intermolecular interactions are predominantly lateral. At the lowest temperatures studied, the behavior of admolecules is predominately dictated by the potential energy of the system; therefore these simulations were used to gauge the relative importance of intermolecular interactions versus adsorption interactions with the surface.

The lowest temperature MD simulations was 100K, and the individual snapshots at 0.7ML were shown earlier in Figure 28. Here, the cbb major and minor axis configurations of individual molecules are classified for these simulations. Occasionally, torsional reorientations about a C-C bond would cause a bend in the cbb. These effects are ignored for the moment, and molecules are classified according the orientation of the major fragment.

In neither system did any adsorbate molecule at any point ever have a majority of its cbb perpindicular to the surface, indicating that the potential energy of molecules is stabilized by the surface potential. Moreover, only four nonane/decane molecules in each system deviate from parallel minor axis orientations C9 and C10. This is not surprising, because these orientations minimize the cumulative distance of all hydrogen atoms from the surface. This distance for the hydrogen atoms pointing down (i.e. toward the surface) is roughly the same for any high symmetry minor axis orientation, but Figure 10 shows that this distance for upward-facing hydrogen atoms is clearly greater for molecules in perpendicular minor axis orientations. For nonane, none of the four perpindicular minor axis molecules are in the C4, all are C5. Since nonane has no such distinction between perpindicular minor axis orientations, this suggests a

source of even-odd disparity in chain length. Finally, no molecule in either system changes minor axis orientation throughout the entire 50ps duration of the simulation. This indicates a high barrier to cbb minor axis reorientation, much higher than k_BT = 8.6 meV for these simulations.

For both nonane and decane in Figure 28, the predominant orientation major axes is ‹11›. Molecules in ‹10› orientations are very rare (none in the frame shown for decane and one for nonane circled in frame). This indicates that the ‹11› orientation is the global energy minimum. Viewing the compiled movies from these simulations shows significant movement of the molecules within minimum energy orientations. Two top views of the MgO slab in suggest a likely explanation for the ‹11› preference (Figure 29). When viewed upright, the alternating Mg^{2+} and O^{2-} ions appear as a checkerboard, but when rotated 45°, they align vertically and horizontally. This emphasizes the fact that the MgO(100) surface can be thought as alternating channels of positive and negative charge in the ‹11› direction. Since the molecules interact with the surface exclusively via their (negatively charged) electron clouds, it is sensible that they prefer to align along these channels to minimize the cumulative distance from the positive Mg^{2+} ions.

As mentioned in Section 1.2, the minimum energy conformations for n-alkane cbb torsional degrees of freedom (tdf's) are the anti conformation (global) and the two gauche conformations (local). shows the distribution of all torsion angles for the 100-350K temperature range studied. Three peaks, each fit nearly perfectly by Gaussian distributions, correspond to the three minimum energy conformations. The anti conformation (represented by the largest peak centered at 180°) is still the global energy minimum. The centers of the other two peaks are spaced 111° from the anti peak center and correspond to distorted gauche local minima. Figure 30 shows the Gaussian distributions of each of these conformers, with the two gauche peaks binned together. This is also done in all subsequent analyses.

The widths of these Gaussian distributions correspond to degree of random fluctuations about the local torsional minima (i.e. rocking or wiggling molecular motion within the cbb). As expected, these widths decreased with decreasing temperature (Figure 31) as k_BT decreases as more molecules settle deeper into torsional potential minimum energy wells. Additionally, the percentage of molecules in each conformation was determined as a function of temperature by integrating the Gaussian fits. Since these correspond to the only two unique minima, these percentages subtracted from 100% presumably gives the average number of molecules transitioning between minima at a given instant. The temperature dependence of these phenomena is shown in Figure 32. The results for nonane and decane are strikingly similar despite the extra tdf for decane. At 100K, over 95% of molecules have settled into straight chain conformations. Less than 1% are transitioning between configurations, while the remainder are trapped in gauche local minima.

Qualitative analysis of the MD videos provides an excellent visual representation of the phenomena quantified above. The anti and distorted gauche conformations appear in the MD trajectories as straight and bent molecular cbb's respectively. Notable decrease in torsional rocking is noticed at simulations of decreasing temperature, and below 220K, molecules show a tendency to become trapped in bent cbb conformations on the surface. However, due to random temperature fluctuations, molecules are never permanently trapped within these minima, and changes in conformation are observed even at the lowest temperatures (100K).

1.4.3 First Adsorbed Layer

In Section 1.3, a variety of thermodynamic quantities were defined and calculated for the first adlayer of nonane and decane. These results are compiled into Table 7:

Table 7. Summary of Calculated First Layer Thermodynamic Values.

	Q_{ads}	$Q_{st,max}^{(1)}$	$Q_{st}^{(bulk)}$	$\Delta H^{(1)}$	$\Delta S^{(1)}$
nonane	37.17	94.6	46	9.83	71.23
decane	24.89	43.6	58	23.4	119.46
units	$kJ*mol^{-1}$	$kJ*mol^{-1}$	$kJ*mol^{-1}$	$kJ*mol^{-1}$	$J*K^{-1}*mol^{-1}$

A peculiar feature of these adsorbates is that Q_{ads} is lower than the bulk Q_{st} values. These results indicate that the first adsorbed layer is less enthalpically stable than the bulk liquids. This is also confirmed by the values of $\Delta H^{(1)}$. This effect is especially conspicuous for decane: Even at its maximum in the first layer, Q_{st} scarcely exceeds 75% of its value at 8+ monolayer coverage. This begs the question: Why does the first adlayer form at all rather than immediately forming bulk liquid in the sample cell?

Given that steps corresponding to first layer formation are clearly observed in all isotherms, this implication of extreme nonwetting behavior is indeed troubling. Fortunately, $\Delta S^{(1)}$ for both of these systems is large and positive, i.e. thermodynamically favorable, at least at high temperatures. Taking $\Delta H^{(1)}$ *and* $\Delta S^{(1)}$ to be constant over the relevant temperature ranges (an admittedly dubious assumption), calculation of the differential Gibbs free energy ($\Delta G^{(1)} = \Delta H^{(1)} - T\Delta S^{(1)}$) reveals that $\Delta G^{(1)}$ is less than zero above temperatures of 138K for nonane and 197K for decane, well below the experimental temperatures studied. Therefore, the first layer is still thermodynamically favored over the bulk albeit due to entropic causes rather than enthalpic ones.

Two other features in the first monolayer region of the isotherms are worth examination. First, the plateau following the first vertical riser is far from perfectly horizontal, indicating that molecules begin to form a second layer before the first is completed. Additionally, the APM at monolayer coverage calculated for nonane and decane showed considerable variation as judged from Figure 17.

Taken together, these observations argue against the formation of a commensurate monolayer. This can be tested by examining the MD simulations trajectories from a top view.

Such still frames are shown in Figure 33 for simulations performed at the highest and lowest temperatures within the experimental range. Here, the coverage is just shy of one monolayer, as judged by the small regions of uncovered surface. These simulations indicate that nonane and decane are in either the 2D liquid or 2D supercritical fluid for the experimental temperatures studied, in accordance with the 2D adsorbed phase transition temperatures discussed earlier in this section. The lowest temperature still frames can be taken to approximate the structure of the 2D monolayer solid. There is short-range order, as molecules tend to align parallel in the ‹11› direction at the lowest temperature, favoring the same orientations as at 0.7 ML for both systems. However, there is no clearly defined unit cell, much less one commensurate with the surface.

This figure also shows the temperature dependence of the cbb major and minor axis orientations for nonane and decane discussed in Section 1.4.2. As the temperature is increased to those similar to the isotherm measurements, Although the same trends that were noted at 0.7 ML coverage continue at 1.0 ML coverage: Most of the molecules are oriented in the ‹11› direction in any given frame, at higher temperatures increased translation motion with increasing k_BT results in deviations from this global minimum. Moreover, it is not unusual for molecules to briefly orient themselves in the ‹10› or intermediate directions before returning to ‹11›. The lingering of molecules in these orientations shows that these correspond to local potential energy minima with respect to the surface. Lastly, it was noted that no reorientations of the ccb axis occurred even in the simulations corresponding to the highest experimental temperatures, which is sensible considering the reduced mean free path at 1ML results in greater lateral intermolecular attractions. These would be expected to stabilize the

lateral orientation of any molecule and suppress rotational motion about the cbb minor axis.

1.4.4 Second Adsorbed Layer

. It was explained in Section 1.3 that all nonane and decane isotherms exhibited a second step corresponding to the formation of a second layer. In Section 1.4.1, the widths of the susceptibilities were plotted against T to determine T_{2C} for the first monolayer. Although not initially discussed, a similar attempt was made for the second layer of nonane and decane, as shown in the bottom of Figure 25. The widths are seen to increase linearly with temperature, leading to the question of whether the critical temperature falls above or below the temperature range studied. If compared to the range of linearly diverging susceptibilites from the first layer data might lead to the conclusion that both decane and nonane second layer critical temperatures are below the experimental temperature range. This, however, would imply a confusing result—that T_{2C} diverges away from bulk values with increasing coverage. A more likely explanation is that there is no two dimensional critical temperature of condensation, perhaps due to the intermingling of the first and second layers. This molecular behavior was frequently seen in the MD simulations corresponding to the experimental temperatures, as will be described below.

A comparison of the Clausius-Clapeyron and Q_{st} results shown below in Table 8 for the second adsorbed layers provide values more consistent with the transition to bulk behavior:

Table 8. Summary of Calculated Second Layer Thermodynamic Values.

	Q_{ads}	$Q_{st,max}^{(2)}$	$Q_{st}^{(bulk)}$	$\Delta H^{(2)}$	$\Delta S^{(2)}$
nonane	47.26	66.7	46	-0.25	4.01
decane	48.64	90.6	58	-0.35	3.27
units	$kJ*mol^{-1}$	$kJ*mol^{-1}$	$kJ*mol^{-1}$	$kJ*mol^{-1}$	$J*K^{-1}*mol^{-1}$

The values of Q_{ads} and are much closer to Q_{bulk} than was the case for the first layer, and the enthalpy and entropy approach that of the bulk, i.e. $\Delta H^{(2)}$ and $\Delta S^{(2)}$,approach zero. Even more interesting, the sign of the differential enthalpy changes from positive to negative, indicating that the second layer becomes more enthalpically favorable than the bulk. The sign of $\Delta S^{(2)}$ remains negative indicating that entropic favorability is maintained. These two facts taken together make the disappearance of the second peak more puzzling.

Figure 35 shows the temperature dependence as the first layer is completed and at the beginning of the first. Three nonane and two decane molecules lie on top of the first layer on the top half of the slab. This step was particularly conspicuous at low temperatures, but barely visible at the highest temperatures (see nonane examples in Figure 34).

These values indicate increasingly 3D behavior due to the introduction of vertical molecule-molecule interactions. The low temperature effects of vertical interactions is perhaps most starkly shown in Figure 36. This shows a top view of a decane 160K system that has 3 molecules in the second layer. These three molecules have been removed from the still frame so that their effects on the first layer can be seen, but their previous locations are outlined in black. Note that the molecules below them are all in a C5 orientation, as opposed to the C10 orientations of virtually all other molecules.

The vertical orientation of the molecules within the film is of prime importance in understanding the wetting properties of these two films and is best studied at

coverages greater than 1ML and typically best viewed the side, i.e. parallel to the MgO(100) surface plane.

The side view at the lowest temperature shows that the terminal methyl group of two nonane molecules extending above the plane of surrounding admolecules, corresponding to torsional reorientation. No such behavior is noticed for decane at this temperature. The molecules in the second layer exhibit many more torsional reorientations. These occur throughout the length of the molecule, unlike those in the first layer.

Once molecules begin to occupy the second layer, the vertical interactions clearly begin to play an important role in molecular behavior. This also is seen to vary with temperature, as judged by the 2nd layer behavior of molecules on the top half of the slab. Note that at the lowest temperatures, these molecules lay flat on top of the first layer. Video evidence shows that the molecules remain in the second layer for the duration of the video clip and display little translational motion. As the temperature is increased, the molecules in the second layer begin to translate about surface formed by the first layer molecules. As these molecules diffuse, eventually they find a gap within the structure of the first layer. They fall into the gap, and momentarily are part of both the first and second layers. This can been seen in the frames close to the experimental isotherm temperatures (240-300K). Looking at the decane 280K system, one such molecule is seen transitioning between the two layers, and appears perpendicular to the surface. These vertical motions show the first signs of multilayer occupation, a broadening of the interface and perhaps signaling the transition toward bulk-like behavior. This is exceptionally clear in the nonane 300K frame, where one molecule momentarily appears to be in the 3D bulk gas phase.

The higher temperature MD frames are considerably more disordered in the monolayer; molecules in both layers are substantially more mobile, both translationally and rotationally. Both systems are therefore in the 2D liquid phase. The boundary between first- and second-layer molecules is much less

clearly defined, as molecules move in between these two layers. In the decane system, one such molecule is seen transitioning between the two layers, and appears perpendicular to the surface.

1.4.5 Bulk Behavior

In regions above , it was not uncommon for the absorbate to suddenly form the bulk liquid rather than adsorbing onto the surface (note how p_f abruptly lurches to the bulk SVP in these figures. This discontinuity indicates a relatively small difference in chemical potential between the adsorbed and bulk phases (μ & μ_0, respectively). When these isotherms are plotted against $\mu - \mu_0$ instead of p_f, then the discontinuity is much less pronounced, and its causes become clear (Figure 14 & Figure 15). Due to their high molecular weight, the velocity of the vapor molecules is low. Furthermore, the kinetics of their adsorption are known to be slow due to the long equilibration times (>1 hour near SVP). At these high coverages, the formation of the 2D surface film is not significantly more thermodynamically favorable than the formation of the bulk adsorbate. The vapor pressure due to adsorbed phase prior to opening V_1 is already close to that of the bulk, and if the shot size is a significant fraction of p_0, then the formation of the bulk can become more favorable than that of the 2D film for kinetic reasons. Since the rest of the isotherm is driven by thermodynamic favorability, this shift to kinetic favorability with the addition of just one aliquot of vapor appears discontinuous.

The sudden lurch to SVP complicates the determination of the type of wetting present. Initially, one might classify this as incomplete wetting, but examination of higher temperature isotherms shows an asymptotic approach to the bulk SVP, characteristic of complete wetting. For the lower temperature isotherms, the nearly horizontal portion immediately prior to the break to SVP is characteristic of nonwetting behavior, suggesting that the kinetic factors above cause the adsorbate to form a nonwetting film on the interior of the sample cell rather than continuing to wet the MgO surface.

The effects at higher coverage (≈2 & 3 ML) are shown in the MD still frames shown in Figure 37 at high temperature. Here the progression of layers toward bulk-like behavior begins to be seen. At both coverages, the 1st layer molecules can still be distinguished as they predominantly lie flat on the surface, but the movement of molecules between the first and second layers begins to accelerate with temperature. At the highest coverages and temperatures, no layers beyond the first can easily be discerned, in agreement with the experimental isotherms.

1.4.6 Summary

Two dimensional solid, liquid, gas, and hypercritical fluid phases of both nonane and decane were observed in the adfilm at 0.7 ML coverage over the temperature range studied (100-350K). At lower temperatures, the gas phase is distinguished from the condensed solid and liquid phases by its low surface density of molecules. At these temperatures, the solid and liquid phases were distinguished by the translational mobility of their constituent molecules, and a temperature dependent transition of the condensed phase was observed. At higher temperatures, the relative surface density of the condensed and gas phases was observed to converge at a critical temperature T_{2c}.

A more precise determination of T_{2c} was made by plotting the width of the isotherm derivative peaks against temperature. The temperature at which the peaks diverged was calculated to be 263.04 ± 1.36 K for nonane & 277.77 ± 1.72 K K for decane, in relatively close agreement with the theoretical MD simulations.

Given the experimental values of T_{2C} values determined in this work and the 2D/3D T_{2C} and T_{2f} ratios determined for other systems (discussed later), the lower bound of the transition temperature ranges as determined in the MD simulations is likely a better indicator of the true transition temperatures. Due to the subjective nature of these qualitative methods, the continuous appearance of these changes should not be interpreted as evidence of continuous phase transitions in either case. More rigorous quantitative analyses would be required to determine the order of these transitions.

At low coverage, lateral adsorbate interactions were compared to the vertical interaction with the surface. Torsional, rotational, and translational motion is observed for adsorbed nonane and decane at the coverage and temperature ranges studied. The translational motion was qualitatively examined. Even at the lowest temperatures studied, significant movement of molecules between potential energy minima due to the surface was observed. The temperature dependence of torsional motion was quantified, and less than 1% of molecules were determined to be reorienting at any given time at the lowest temperatures studied. Rotational motion was clearly the least commonly seen at low temperature, as the minor axis of no molecules were seen to reorient. The barriers to reorientation are therefore clearly the highest for rotational motion. The relative barriers between translational and torsional motion would require further study, as the temperature dependence was only quantified for torsional modes.

The convergence of the behavior of the 2D adfilms toward that of the 3D bulk as coverage increased was investigated. This was judged by the extent of vertical interactions between adsorbate molecules. A tendency toward bulk-like was seen to increase both with temperature and coverage. The convergence of the behavior of the 2D adfilms toward that of the 3D bulk as coverage increased was investigated. This was judged by the extent of vertical interactions between adsorbate molecules. A tendency toward bulk-like behavior was seen to increase both with temperature and coverage. In the experimental isotherms, this was seen in the form of a prominently large step corresponding to formation of a thermodynamically distinct monolayer. This was followed by a less prominent second step that gradually diminished as the temperature was decreased. The thermodynamic values for this second step were calculated to be much closer to bulk literature values of each adsorbate. Following the second step, a smooth, asymmtotic approach to bulk SVP was observed, corresponding to complete wetting and a gradual convergence to bulk behavior.

These trends were further confirmed by comparison to still frames from the MD simulations. As coverage increases at constant temperature, vertical motion between subsequent layers accelerates, and the behavior of molecules trends even more towards that of the 3D bulk phase. At 0.7 ML, molecules were predominantly flat on the surface at all temperatures. At 1ML, molecules began to transition between the first and second layers, especially as temperature increased. Looking at the 2ML frames, molecules begin to transition between the 2^{nd} and 3^{rd} layers, and these two layers are even harder to distinguish. When the coverage is between 3 and 4 ML, these two layers are nearly impossible to distinguish. At these coverages and temperatures, even the second layer begins to merge with the upper layers as judged by the vertical movement of individual molecules.

The interplay between lateral interactions (exclusively molecule-molecule) with vertical interactions (both M-M and M-S) warrants further study. The temperature dependence of the relative importance of these interactions is of particular interest. As the temperature increases, modes of all types of motions become more active, and molecular collisions become more frequent. The energy exchange of these collisions will be evident from the observed changes in molecular motion of all types.

Within this work, this was done primarily qualitatively. Future studies should supplement this approach with further quantitative analyses, as was done for the torsional motion reported here. Regarding future torsional analyses, it is recommended that each tdf be analyzed independently to aid in the investigations of carbon chain length. Torsional reorientations of terminal erminal methyl groups were observed much more frequently in the MD simulations that torsions amongst four carbon atoms. This is due to the greater steric hindrance in rotating large fragments of the cbb about a single bond.

In addition to torsional motion, quantitative analyses of the rotational and translational motion can also be quantified using the Analysis options within Forcite. Materials Studio allows the definition of axes for use in future analysis.

This should be done for the major and minor axes of the cbb plane, prior to the addition to the surface, The Concentration Density, Density Field, and Radial Distribution Function tasks within the Analysis module could then be used to determine both the lateral and vertical orientations of these axes with respect to the surface plane. Particular attention should be paid to the Radial Distribution Function, since this gives the Fourier transform of the structure factor and could be compared to future experimental neutron diffraction results.

1.5 Thermodynamic Trends

1.5.1 Noble Gases on Metal Dihalides

The ratio of the critical temperatures of a 2D adsorbed phase and the bulk phase (T_{2C} / T_{3C}) is thought to be closely related to the compatibility of the size of the adsorbate molecule with the size of adsorption site. In an extensive study, Lahrer used spherical molecules adsorbed on transition metal dihalides [1,20]. The incompatibility factor i was defined as $(a - d) / d$, where a is lattice constant of the substrate and d is the diameter of bulk adsorbate molecules on the (111) face of their fcc crystal. T_{2C} / T_{3C} was found to reach a maximum of 0.51 for perfect compatibility ($i = 0$), and to decrease as the incompatibility rose in either direction (see Figure 38).

Moreover, T_{2C} / T_{3C} , $\Delta S^{(1)}$ and surface incompatibility are closely intertwined. The trend between $\Delta S^{(1)}$ and i for spherical molecules on halides has been shown to be the reverse of that of T_{2C} / T_{3C}: $\Delta S^{(1)}$ reaches a minimum at $i = 0$ and then increases as i deviates in either direction, presumably due to a decrease of the in-plane vibrational frequency of admolecules [1]. When there is a significant mismatch between the dimensions of the surface and adsorbate, the structure of the 2D monolayer deviates significantly from that of an exposed face of the bulk adsorbate. This weakens the interactions between adsorbate molecules relative to those of the bulk (i.e. larger $\Delta H^{(1)}$ and lower T_{2C} / T_{3C}) and allows individual admolecules more degrees of freedom (i.e. larger $\Delta S^{(1)}$).

Based on this analysis, the differential entropy and the density of the monolayer (or its inverse, APM) seem to be intertwined. This was also noted in the noble gas/halide studies [17]. That work provided a theoretical justification for using the ratios of the adsorbate densities as a proxy for the ratios of $\Delta S^{(1)}$, provided the adsorbate was significantly larger than the potential well. The surface density and $\Delta S^{(1)}$ ratios of Kr and Xe on $CdCl_2$ and $FeCl_2$.were compared, and near perfect agreement within experimental error was found.

1.5.2 Alkanes on MgO - First Layer Trends

Applying this reasoning to alkanes adsorbed on MgO, one might expect a maximum in *i* for methane (nearly perfect match between lattice constant and molecular diameter), and then a decrease as one goes up in chain length, since the lattice constant remains the same while the molecular size increases. The data show otherwise (Table 9 & Figure 39). T_{2C} / T_{3C} remains nearly constant at 0.42 through propane, then begins to increase up to a maximum of 0.48 for octane, and finally decreases again for nonane and decane (0.44 & 0.45 respectively).

Table 9. Alkane Critical Temperature Trends.

Alkane	**T_{2C} (K)**	**T_{3C} (K)**	**T_{2C}/T_{3C}**
Ethane	127	305	0.416
Propane	155	370	0.419
Butane	190	425	0.447
Pentane	215	470	0.457
Hexane	230	508	0.453
Heptane	255	540	0.472
Octane	275	569	0.483
Nonane	263	595	0.442
Decane	277	618	0.448

In fact, a number of the quantities determined for the first layer of nonane and decane are quite anomalous when viewed in the context of those calculated for smaller alkanes on MgO. When plotted against the number of carbons in the adsorbate backbone, the differential enthalpies/entropies (Figure 40) and the area per molecule (Figure 41) all diverge from the trends set by the smaller alkanes. This obviously deserves an explanation.

Looking at the thermodynamics plots for the first layer, the heat of adsorption Q_{ads} steadily increases with chain length through octane before plummeting for

nonane and decane. Correspondingly, the differential enthalpy $\Delta H^{(1)}$ spikes from relatively small negative values (~ -5 kJ/mol) to much larger positive values for nonane and decane (≈ 10 & 24 kJ/mol respectively). This indicates that the first adsorbed layer goes from being slightly more enthalpically stable than the bulk phase for octane to being much less enthalpically stable for nonane and decane. This begs the question of why the first adlayer should form at all rather than immediately forming bulk liquid in the sample cell.

Fortunately, the anomalous enthalpy results are accompanied by anomalous entropy results, as $\Delta S^{(1)}$ also jumps from being small and negative to large and positive. When used to calculate the differential free energy change between the first adlayer and the bulk ($\Delta G = \Delta H - T\Delta S$), the entropic term more than offsets the enthalpic term over the temperature range studied for each system, meaning that the first layer is still thermodynamically favored over the bulk, albeit due to entropic causes rather than enthalpic ones. The enthalpy results are no longer not as troubling, as there are similar examples in the literature of entropically driven adlayer formation (e.g. the second layer of krypton on CaI_2 [19] and the first layer of krypton on alkali fluorides [49]).

Although large n-alkane molecules are not spherical, the same principle applies to nonane and decane. For these roughly linear molecules, minima in the surface interaction potential are not so much energy wells (as is the case for spherical molecules), but rather energy channels in the (11) direction. This is evident from the low temperature molecular dynamics simulations, in which the major axis of the carbon backbone showed a clear preference to align in the (11) direction. In these calculations, the closest spaced ccb major axes were separated by ≈3-4 Å. These are significantly larger compared to the closest *d*-spacings for bulk nonane and decane (2.30 and 2.02 Å [50], respectively). The spacing between molecules has certainly expanded with adsorption, leading to an increase in entropy. This is further confirmed by the fact that admolecules showed a significant amount of lateral reorientation of the ccb major axis, even at temperatures ~0.4 times the bulk freezing point.

Calculating the corresponding entropy and APM ratios for nonane and decane yields values of 1.7 and 2.0. These do not compare quite as favorably as the Kr and Xe results, even when the most favorable APM values within experimental error are used. Nevertheless, the general trend buttresses the argument for the simultaneous divergence of $\Delta S^{(1)}$ and APM for these two systems.

1.5.3 Alkanes on MgO - Second Layer Trends

The thermodynamic values of the second layer of nonane and decane, however, do not diverge from those of smaller n-alkanes (Figure 42). This is not surprising, as any corrugations in the surface potential are smoother for the second layer than the first. Since the vertical interactions of second-layer admolecules are primarily with other admolecules in the first layer instead of directly with the surface, their behavior is much more bulk-like. Methane and ethane are exceptions, but the second adlayer for both of these are known to interact significantly with the surface as judged by the presence of distinct third layers. Although there is no divergence in the behavior of the second adlayers of nonane and decane, a rough even-odd trend with carbon chain length emerges for the second layer. Recall that the C9 and C10 orientations (those with the minor axis parallel to the surface) were predominant in the MD simulations at submonolayer coverages. For nonane a clear preference was also shown between C4 and C5 orientation (i.e. the two minor-axis-perpendicular orientations), with literally no molecules adopting the C4 orientation at the lowest temperatures. This trend has also been shown to hold true for smaller odd-numbered alkanes. For even-numbered alkanes, these two orientations are equivalent (both C5 for decane). Since molecules in the second adlayer interact appreciably with those in the first, this preference for one minor axis orientation over another should be felt for odd—but not even—numbered alkanes, providing a possible explanation for the sawtooth appearance of these plots.

1.5.4 Conclusions

The simultaneous divergence of various thermodynamic data for the first adlayer of nonane and decane on MgO(100) is explained in terms of the relationships of the 2D/3D ratio of the critical temperature, differential entropy, and admolecule density with surface compatibility as outlined by Larher *et al* for spherical adsorbates on transition metal dihalides [1,17–20]. For chain-like alkanes, the channel-like corrugations of the surface potential in the (11) direction of the MgO substrate are analogous to the radially isotropic potential wells experienced by the spherical adsorbates studied by Lahrer.

Additionally, the coarse even-odd dependence of thermodynamic data the second adlayer with alkane chain length is attributed to adsorbate-adsorbate interactions between the first and second layers. First-layer admolecules of odd-numbered alkanes possess two distinct orientations in which the plane of the carbon backbone is perpendicular to the surface, and the orientation with more carbon atoms closer to the surface is favored. For even-numbered alkanes, no such distinction can be made. This asymmetry in odd-numbered alkane first adlayer orientations is extended to the second layer through intermolecular Van der Waals forces, leading to a saw-tooth appearance when the differential enthalpy and entropy of the second layer are plotted as a function of chain length.

Many questions remain concerning the divergent behavior of the first adlayer thermodynamic data. The substrate channels are infinitely long from the perspective of an alkane molecule, and the widths of the carbon backbones are approximately equal for all alkanes. It is not clear why nonane should be the threshold at which this behavior appears. Neutron experiments should help address these concerns. QENS techniques would allow more precise determination of the 2D critical temperatures of condensation, allowing better comparison of their 2D/3D ratios. Moreover, since the lower temperature limit of QENS is not limited by decreasing vapor pressure (as is the case for adsorption isotherms), the presence of 2D melting transitions might also be detected. Given

that nonane and decane represent just the beginning of this divergence, it would be worthwhile to explore the thermodynamics of the first adlayer of even larger alkanes (i.e. undecane and dodecane). The differential enthalpy and entropy for these systems is predicted to be even higher than that of decane, while the ratio T_{2C} / T_{3C} is predicted to be lower. Due to the decreased vapor pressure of these molecules, current in-house adsorption isotherm apparatus would need to be modified to allow higher dosing and sample temperatures.

CHAPTER II
ROTATIONAL TUNNELING OF ADSORBED CH_2D_2 AND CH_3D ON MGO(100)

2.1 Introduction & Background

2.1.1 Overview

As mentioned in the previous chapter, molecular adsorption on MO's has a wide variety of potential applications, and magnesium oxide in particular has uses as a catalyst and catalyst support. Meanwhile, methane is a vital feedstock for hydrogen and syngas production, and its economic competiveness as an energy source has boomed with recent technological advances in hydraulic fracturing. Although many aspects of the competing electrostatic interactions governing physisorbed films on MO surfaces remain poorly understood, examining systems involving relatively simple surfaces and adsorbates can provide fundamental knowledge of these processes. In this regard, MgO(100) and methane are prime candidates for investigation: MgO(100) has a prototypical rock-salt structure, and methane is the simplest hydrocarbon.

The goal of this chapter is to understand the low temperature (< 4K) behavior of methane thin films adsorbed onto MgO. As is always the case in surface adsorption, this behavior is regulated by the interplay between adsorbate-surface and adsorbate-adsorbate forces. Due to the insignificant translational and rotational molecular motion at these temperatures, these interaction potentials are static in nature, i.e. random fluctuations are negligible. Under these conditions, libration and rotational tunneling are the primary behaviors observed. As will be described, rotational tunneling spectra (RTS) are extremely sensitive to the strength and symmetry of the interaction potential between an admolecule and its adsorption site, and Inelastic Neutron Scattering (INS) is one of the few methods capable of observing these spectra. The focus of this work is to

investigate how the relative compatibility between molecular and site symmetry affects the rotational tunneling of methane adsorbed onto MgO(100).

Following this overview, the concept of rotational tunneling is compared to an example of tunneling that might be more familiar to students of quantum chemistry: Translational tunneling between two minima of a square potential. The similarities between this system and hindered quantum rotors are highlighted. This section proceeds with a brief introduction to INS and a discussion of why this technique is so well-suited for measuring the RTS of hydrogenous species. The remainder of the section consists of a literature review of previous investigations of methane RTS. The simplest such spectrum involves high symmetry of both the molecule and the site (both at least approximately tetrahedral in the case of Phase II CH_4). These are then compared to CH_4 monolayers adsorbed on graphite and MgO(100) in order to explore the effects of reduced site symmetry. Finally, the section concludes by reviewing the limited studies available for systems of reduced molecular symmetry (Phase III CH_2D_2 and CH_3D as well as CH_3D on graphite). and with

Section 2.2 begins with an explanation of the experimental difficulties in measuring the RTS of these lower symmetry methane isotopologues, followed by a description of the function and technical capabilities of the Backscattering Silicon Spectrometer (BASIS) at the Spallation Neutron Source (SNS) at Oak Ridge National Laboratories (ORNL). Emphasis is placed on how the scattering geometry of BASIS can overcome the challenges mentioned. Lastly, the experimental methods used to collect RTS of CH_2D_2 and CH_3D on MgO(100) are summarized.

Section 2.3 presents these experimental findings, and the energy transfers and widths of the features of these two systems are analyzed. These experimental results are complemented by a theoretical framework based on theory developed by Hüller, Press, and others [51–55]. For both systems, both the 2D crystal lattice of the adsorbate and the minimum energy rotational configurations (i.e. pocket states, or PS's) are assumed to be the similar to that

of CH_4 on MgO. This approach predicts possible tunneling transitions by analyzing the symmetry relationships between PS's for one molecule at one adsorption site. For CH_2D_2/MgO, the energy transfers of selected transitions predicted by the PS model are calculated over a range of interaction potential strengths using variational methods.

Section 2.4 compares these theoretical predictions to the experimental spectra, and the CH_2D_2/MgO and CH_3D/MgO systems are described as two opposing cases of molecule-site compatibility. In the complementary case (CH_2D_2), the C_3 axes present in tetrahedral CH_4 are removed, presumably reinforcing the tendency of the molecule to align with the C_2 rotational potential at a given adsorption site. The PS model for this system is then simplified in order to match the experimental spectrum. Next, the observed features of this spectrum are assigned to the resulting predicted tunneling transitions, and the magnitude of PS overlap as well as the height of selected barriers to rotation is calculated. These results will be compared to those from other systems mentioned in Section 2.1. Conversely, CH_3D contains no molecular C_2 axes, and the compatibility of molecular symmetry (threefold) and site symmetry (twofold) is frustrated. How this affects the rotational orientation of the molecule with respect to the surface is unclear. This chapter then concludes with a summary of findings and recommendations for future studies.

2.1.2 Translational vs. Rotational Quantum Tunneling

A simple example of quantum tunneling is that of a particle confined to a double minimum square potential well. This is an extension of the particle in a 1D box problem—typically the first system students are exposed to in quantum chemistry. In that system, the allowed wavefunctions of the particle are a sum of sine and cosine components. If the walls of the potential are infinite, then these wavefunctions terminate at the boundaries of the well, i.e. the particle may not travel into the walls of the well. The presence of a neighboring well with an equivalent minimum does not change this description of the system provided that

the barrier separating the two minima is also infinite. If the initial position of the particle is not known *a priori*, then the particle is equally likely to be in either well, and these two states are degenerate. The particle may not travel between the two wells (neither classically nor quantum mechanically). If, however, the barrier separating the wells is finite yet still greater than the kinetic energy of the particle, then the quantum and classical descriptions of the system diverge. Classically, the particle still cannot overcome the barrier, but from a quantum mechanical perspective the wavefunctions of the particle now decay exponentially into the barrier. The components corresponding to each well now may overlap inside the potential barrier, and there is a small—but nonzero—probability that the particle will tunnel through the barrier into the other well. This overlap causes a splitting of the energies of the two states, which were degenerate in the infinite barrier case.

Figure 43 illustrates this example alongside that of a quantum rotor with one rotational degree of freedom within a rotational potential of six-fold symmetry. Hypothetically, this might correspond to a methyl group of some large molecule rotating about a C-C single bond in close proximity to a benzene ring. The potential may be sketched on the surface of a circle, and it has six equivalent minima and six equivalent saddle points. If the kinetic energy of the rotor is less than that of the rotational potential barriers, then it will be confined within one of the six minima corresponding to minimum energy configurations, although it may still angularly oscillate (librate) within these minima. The wavefunctions of the rotor are therefore localized within the potential minima (PS's), but they do overlap within the barriers since the barriers are not infinite. This allows the rotor to reorient itself by tunneling from one PS to another.

This principle also applies to rotors with three rotational degrees of freedom, e.g. CH_4. Within a crystalline solid (either 2D or 3D), the interactions of a reference molecule with neighboring atoms can be approximated by the Lennard-Jones potential mentioned in the previous chapter. These combine to form a rotationally hindering potential. Methane—a tetrahedral molecule—has three C_2

axes and four C_3 axes, yielding a total of twelve rotational symmetry operations (including the identity operation). When a CH_4 molecule is confined to a minimum energy rotational configuration, then performing any of these twelve operations will result in a state degenerate to the original. Therefore, a CH_4 molecule librating in a rotational potential of any symmetry may occupy one of twelve degenerate pocket states. However, unless the barriers to rotation are infinite, these PS's are not eigenstates for the molecule due to overlap between wavefunctions of neighboring PS's. Although the molecule may lack sufficient kinetic energy to classically overcome the rotational barriers, these overlaps enable the molecule to quantum mechanically tunnel through them. This rotational tunneling is observed as a splitting of the ground librational state into sublevels. Not surprisingly, the symmetry of both the adsorbate and the adsorption site determines the number and relative positions of these sublevels. The magnitude of the splittings decreases exponentially as the ratio of the height of the potential to the molecular rotational constant (V/B) increases. Assuming that the sites of the material are uniform (as in MgO(100)), the rotational tunneling spectra (RTS) of adsorbed molecules are an extremely sensitive probe of the strength and symmetry of the interaction potential at these sites.

2.1.3 Inelastic Neutron Scattering (INS)

Neutron scattering involves bombarding a sample with a beam of neutrons. The neutrons are then scattered by nuclei in the sample, and the direction and energies of the scattered neutrons provide information about the structure and dynamics of the sample. The incident and scattered neutrons are described by their momentum vectors (**k** and **k'**, respectively). The difference between these two vectors is termed the scattering vector (**Q**). If the magnitudes of **k** and **k'** are not equal, then energy has been transferred either from the neutron to the sample or vice versa. This can be illustrated in terms of a scattering triangle showing **Q**, **k** and **k'** (Figure 44). The scattering is said to be inelastic, and the energy transfer is denoted as ε. The intensity of scattered neutrons as a function

of **Q** and ε (also called the structure factor $S(\mathbf{Q}, \varepsilon)$ or the scattering law $I(\mathbf{Q}, \varepsilon)$) provides information about the dynamics of the system in a manner analogous to Raman spectroscopy [56].

For a variety of reasons, inelastic neutron scattering (INS) is an ideal technique for measuring the RTS of adsorbed hydrogenous monolayer films. Rotational tunneling is an inherently single-particle phenomenon, i.e. the reorientation of one molecule occurs independently from that of neighboring molecules. The corresponding scattering of neutrons is therefore incoherent. Since the 1H nucleus has an incoherent scattering cross section that is over 40 times that of any other isotope of any element, nonhydrogen-bearing substrates (such as MgO) are virtually transparent; and the observed spectrum primarily measures the contribution from the hydrogenous methane adsorbate. Moreover, because neutrons only interact with atomic nuclei through the short-range strong nuclear force, matter appears as mostly empty space. Neutron beams are therefore highly penetrating and are not appreciably attenuated by the cryostat, sample cell, etc. This penetration also allows the neutrons to probe the entire sample, rather than just the exterior. Most importantly, in order for the wavefunction of the molecule to satisfy the spin statistics theorem, a tunneling transition involving a change in PS symmetry must be accompanied by a change in nuclear spin function symmetry. Unlike methods that use electrons or photons as probes, neutrons can flip nuclear spins, inducing the changes in nuclear spin symmetry necessary to observe rotational tunneling transitions [51].

2.1.4 Phase(II) CH_4

The INS spectrum of Phase II CH_4 is particularly helpful in understanding the importance of ratio of the rotational barrier to rotational constant (V/B) for hindered 3D rotors. The structure of CH_4(II) was predicted using a model that considered only nearest-neighbor octapole-octapole interactions [57], and its unit cell consisted of eight molecules. This model was later improved with the inclusion of hexadecapole terms [58], and the corresponding structure for CD_4(II)

was later experimentally confirmed using neutron diffraction [59].. The octapole-octapole interactions cancel for two of the eight molecules ($V/B \approx 0$), which behave nearly completely free 3D rotors as judged from the presence of peaks at 1.06 and 1.8 meV, corresponding to J = 0→1 and J = 1→2 rotational transitions [60]. These electrostatic interactions do not cancel for the remaining six molecules in the unit cell, and their rotational orientations are fixed with respect to the crystal lattice. Their RTS of has been measured via INS [61,62] and is shown in Figure 45.

The theory of CH_4 INS tunneling spectra has been described in terms of the symmetries the PS's and nuclear spin states of the rotationally ordered molecules [51,54,63]. The intensities of the INS spectrum were determined by calculating the structure factor $S(\mathbf{Q}, \varepsilon)$ contributions for each of the 192 combinations of the twelve PS functions and the sixteen nuclear spin functions. The symmetry relationships between the twelve PS's dictate that the ground librational state will split into sublevels composed of one singlet, one doublet, & three triplet states with respective symmetries A, E, & T. Meanwhile, the sixteen nuclear spin states of the molecule decompose into five A, three T, & one E states. These correspond to states of total nuclear spin I = 2, 1, & 0, respectively. A neutron (I = ±1/2) can either flip the nuclear spin of a single proton or leave all nuclear spins unchanged. Therefore, only changes in total nuclear spin of ΔI = ±1, 0 are allowed. In order to satisfy the Pauli Exclusion Principle, a tunneling transition between PS's of different symmetries must be accompanied by an identical change in nuclear spin symmetry. Therefore A↔T & T↔E transitions for CH_4 molecules are allowed (ΔI = ±1), but A↔E transitions are forbidden (ΔI = ±2).

The spectra of CH_4(II) has been explained in terms of a PS model in which the symmetry of the rotational potential at the ordered sites was approximated as tetrahedral [55,64]. This resulted in the degeneracy of all three T sublevels. The peaks at 73 and 143 μeV therefore correspond to the A→T and T→E tunneling transitions. Furthermore, the ratio of the energy transfers of these transitions

was perfectly 2:1 within experimental error. This indicates that overlap between PS's separated by two-fold rotations is negligible compared to those separated by three-fold rotations. In a manner analogous to increasing the barrier width for translation tunneling [65], it was postulated that the barrier to 120° rotation is less than that of 180° rotation due to the smaller arc through which constituent atoms must rotate. This would subsequently be supported by INS results of CH_4 in environments of various potential symmetries, as the corresponding RTS were consistently shown to be dominated by these three-fold overlaps.

2.1.5 CH_4 Adsorbed on Solids

At surface temperatures below 20K, the rotational motion of an adsorbed methane molecule within a monolayer solid is noticeably reduced. Molecular rotation exists primarily as librations within a potential energy well much deeper than the rotational constant of the molecule. At typical INS experimental temperatures (below 4K), virtually all molecules are in the ground librational state, and only rotational tunneling occurs. If methane forms a 2D crystal structure commensurate with the surface, then the adsorption sites (as well as their corresponding interaction potentials) are uniform. In contrast with the nearly tetrahedral potential symmetry at the ordered sites of CH_4(II), adsorbed methane films allow the exploration of lower-symmetry rotational potentials consisting of both molecular and surface contributions. The importance of the surface contribution to the rotational potential of a reference methane molecule is twofold: In addition to direct interactions, the surface also guides the structure and the 2D adsorbate lattice and the rotational orientation of nearest neighbors.

Systems featuring interactional potentials containing C_2 and C_3 symmetry elements are of particular interest, as these coincide with the tetrahedral molecular symmetry of CH_4.

On graphite, CH_4 forms a $\sqrt{3}x\sqrt{3}$ 2D lattice commensurate with the hexagonal substrate lattice, and the molecules oriented tripod down with respect to the surface [66]. The rotational potential for an individual CH_4 molecule is therefore

of symmetry C_{3v}. INS studies of the RTS of this system [67] revealed five observable tunneling transitions, indicative of a splitting of the three T states into two separate sublevels (Figure 46). There are two distinct three-fold overlaps between PS's: One corresponding to rotation about the molecular axis normal to the surface and the other about the three C_3 axes pointing toward the surface. Given the relatively smooth surface potential of graphite, the barrier to reorientation about the normal axis is primarily associated with adsorbate-adsorbate interactions. The barrier about surface-facing axes is of course dependent on the strength of the surface potential. These barriers to reorientation were calculated from the magnitude of the RTS splittings to be 202 cm^{-1} and 172 cm^{-1} about surface-normal and surface-facing axes, respectively. This led to the conclusion that potential is dominated by contributions from adsorbate-adsorbate interactions.

For MgO(100), a neutron diffraction study determined that the CH4 monolayer solid phase adopts a commensurate $\sqrt{2}x\sqrt{2}R45º$ (also known as C(2x2)) structure [25]. Subsequent INS studies of this monolayer [23,26] uncovered three evenly spaced T sublevels (Figure 47), which is consistent with an interaction potential of C_{2v} symmetry that is inconsistent with a tripod admolecule orientation. Therefore, it was concluded that CH_4 assumes dipod orientation with respect to the surface. Moreover, the normal component of the surface potential is of fourfold symmetry at high-symmetry sites on MgO(100), indicating that the reduction to twofold symmetry is due to adsorbate-adsorbate interactions. Since each admolecule has four nearest neighbors, each must be rotated by 90° in order to produce a C_{2v} rotational potential for a reference molecule. These spectra extended over an energy window five times that of graphite, indicating lower barriers to rotation for CH_4/MgO. Later INS investigations [30] concentrated on the layer-by-layer evolution of CH_4/MgO RTS behavior and found that the spectrum converged to that of bulk Phase II CH_4 as adlayer distance from the surface increased. The local structure at coverages of ~4 layers looked more similar to the fcc bulk phase.

These spectroscopic predictions for CH_4 on MgO(100) surfaces were explored in more detail using a DFT approach employing a plane-wave basis set and periodic boundary conditions. The results of these calculations confirmed the experimental conclusions and showed unequivocally that the minimum-energy configuration of the CH_4 molecules is directly above a surface Mg atom, that a C_{2v} axis of the molecule is normal to the surface plane, and that pairs of hydrogen atoms are oriented along the lattice lines that include adjacent surface O atoms. Moreover, the rotation of neighboring methane molecules by 90° was found to reduce H-H steric hindrances [27,29]. Other more restricted DFT studies have also confirmed the energetic favorability of the dipod configuration for a CH_4 molecule above a Mg atom by focusing on the electrostatic and polarization components of a rigid CH_4 molecule and a lattice of point charges intended to mimic the MgO(100) surface [68]. Most recently, calculations of monolayer and bilayer lattices of methane on MgO(100) have reproduced the observed stability of the commensurate lattices using a surface energy corrugation that implies a large gap in the monolayer phonon density of states consistent with the incoherent inelastic neutron scattering measurements [28].

For CH_4 monolayers on both graphite and MgO, the splitting of the T levels has proven to be an effective indicator of the rotational potential symmetry of individual molecules. This information is valuable in determining the 2D lattice structure and molecular rotational orientation. Agreement between experiment and theoretical predictions is found, even when contributions from twofold overlaps are neglected, supporting the notion that threefold reorientations are generally predominant for CH_4. It should be noted for CH_4/MgO, however, that the energy transfers of the two T→T transitions differ by ~20% (cf. Table 1 in [23]). For an idealized tetrahedral molecule in a C2 rotational potential, these transitions would occur at identical locations if the RTS were solely due to three fold overlaps. As will be seen, the possible relative significance of the twofold overlaps is particularly relevant the spectra reported in Section 2.3.

2.1.6 Reduced Molecular Symmetry – CH_2D_2 & CH_3D

The INS spectra of systems featuring lowered molecular symmetry are not as well understood as the lowered-site-symmetry systems mentioned in the previous section. Comparatively fewer RTS studies currently exist for the lower symmetry methane isotopologues such as CH_2D_2 & CH_3D. Previous INS studies of the bulk Phase III crystal of these species have revealed multiple rotational tunneling features in the range of 0-40 μeV. These were accounted for using a PS model based on a structure in which half of the molecules reside in sites of C_2 symmetry and half in sites of C_s symmetry. Given the presumption of two unique adsorption sites, this model predicted substantially complex spectra, and multiple tunneling transitions were attributed to each feature [69].

INS data have also been collected for the first adlayer of CH_3D on graphite, and three features were identified at energy transfers of less than 60 μeV [70,71]. The strongest of these features was initially predicted to be a combination of two tunneling transitions based on its width, and later the remaining two features were also attributed to multiple transitions. The CH_3D/graphite system was interpreted using a PS approach similar to that used for CH_4 systems, with an added distinction that the twelve minimum energy configurations were no longer degenerate upon substitution of a deuteron. Correspondingly, these twelve PS's were divided into two groups of degenerate states (D-up and D-down) based upon the orientation of the C-D bond (away and toward the surface) [71,72]. The difference in energy between these two unique orientations was thought to be large enough that tunneling between nondegenerate orientations was negligible. PS's related by rotations about a C-H bond (no longer an axis of molecular symmetry for CH_3D) were assumed to be degenerate, provided that the deuterium atom maintained the same orientation about the surface. Although not explicitly stated, this neglects effects of nearest-neighbor orientations on the rotational potential. For the CH_2D_2 spectrum reported in Section 2.3, these effects will be discusses in a qualitative manner.

2.2 Experimental Details

2.2.1 Function and Capabilities of BASIS

As might be surmised from the relative lack of rotational tunneling studies for deuterated methane isotopologues, measuring these RTS presents additional experimental challenges compared to identical studies of CH_4. A principal reason is that the incoherent scattering cross section of a deuteron is 1/40 that of a proton. The signal from CH_3D and CH_2D_2 is therefore reduced by ≈25% and 50% respectively compared to that of an equivalent amount of CH_4. Consequently, higher neutron flux and/or longer counting times are required to achieve signal to noise ratios equivalent to those of CH_4 systems. Additionally, the rotational constants for these molecules are less than that of CH_4 due to the increased moments of inertia. Because the tunneling splittings decrease exponentially as *V/B* increases, the RTS of CH_3D and CH_2D_2 adfilms are confined to narrower energy windows, requiring a spectrometer with higher energy resolution. Fortunately, BASIS at the SNS at Oak Ridge National Laboratories meets these requirements. Spectra with signal to background equivalent to the ones described herein would be difficult (if not impossible) to perform elsewhere.

Time-of-flight (TOF) spectrometers such as BASIS determine that the incident and scattered neutron energies by time required for the neutrons to travel a known distance. TOF spectrometers may employ either direct or indirect scattering geometries. For direct scattering geometries, the incident (initial) neutron energy is fixed by a monochomator or chopper, whereas inverted scattering geometries such as BASIS detect scattered neutrons of fixed final energy. Indirect geometry spectrometers that use backscattering to maximize the resolution of the neutron energy transfer by detecting neutrons that are scattering in the direction from which they came, i.e. the Bragg reflection angle is θ at or near 90°. More specifically, the geometry of BASIS selects neutrons of final energy 2082 μeV (λ = 6.267 Å) which pass through Si(111) analyzer crystals

that reflect the neutrons at θ = 88° [73]. In the experiment reported below, this geometry provides a resolution of ≈3 μeV.

2.2.2 Methods

Approximately 20 grams of MgO nanocubes were prepared using the Kunnman-Larese method [35]. As mentioned in the previous chapter, this method produces nanocubes with a narrow particle size distribution (250 ± 30 nm edge length), high surface area (10 m^2g^{-1}), and with exclusively the (100) face exposed. The reader is referred to Section 1.2.1 for details concerning the production and characterization of these nanocubes. The sample was then transferred under argon into an aluminum sample and sealed with an indium gasket. This sample can was later inserted into a cryostat insert stick described elsewhere [74]. This was then placed in an orange cryostat (AS Scientific, Abingdon, U.K.) and connected to a portable isotherm station similar to the one describe in Section 1.2.

The temperature of the sample was then lowered to ≈77K, and an amount of adsorbate corresponding to ~0.8 monolayer coverage was added in 50-100 torr aliquots. This monolayer capacity was using a CH_4 isotherm at 77K. Once dosing was completed, the sample is cooled at ≈1K per minute to the order-disorder temperature (30K), where it was annealed for an hour. The sample was then slowly cooled to 2K over 1.5 hours. INS data was then collected within an energy window spanning -250 to +250 μeV. In addition to the adsorbate/MgO collection runs, data was also collected for the bare MgO sample as well as a vanadium sample of the same dimensions as the aluminum can. These were later used to subtract the substrate contribution to the spectra and determine the instrument resolution function. For all spectra report here, the data were summed over a Q range of 0.4 to 2.0 $Å^{-1}$.

2.3 Results & Analysis

2.3.1 Spectra

The background-subtracted INS spectrum of a monolayer of CH_2D_2 adsorbed onto MgO(100) at 2.0K is illustrated in Figure 48. The peaks at energy transfers near 15, 31, 45, and 126 μeV are attributed to rotational tunneling transitions within the ground librational state of the CH_2D_2 molecule. The corresponding INS spectrum for CH_3D is shown in Figure 49. When the spectrum is viewed over the full energy window, prominent features are readily observable near energy transfers of 40, 51, 95, & 138 μeV. Closer inspection of the region between 30 and 75 μeV reveals that additional transitions—possibly doublets and triplets—may be present. These fine structures are found at the same positions on both the energy loss and gain sides, strongly suggesting that they are genuine and not statistical noise.

Given that peak widths have been used as an indicator of the presence of multiple transitions within a feature for other RTS [71], the primary features (including the elastic line) of both spectra were fitted with Gaussian curve fits, and the full width at half maximum (FWHM) of these Gaussians were plotted against the peak centers. A linear relationship is observed between the width and position of these peaks for CH_2D_2/MgO, with the exception of the feature at 15 μeV (see Figure 50). When this peak is excluded, the least-squares linear regression of the remaining transitions predicts a FWHM of 4.46 μeV for a transition at 15 μeV. The observed width is 46% greater, suggesting that the feature at 15 μeV may consist of more than one transition. For the CH_3D spectrum, the widths of the primary features generally increase with increasing energy transfer, but the trend deviates significantly from linearity (see Figure 51).

There is no theoretical basis for a linear relationship between the peak width and energy transfer for rotational tunneling transitions; it is only an empirical observation seen in some rotational tunneling systems. Nevertheless, the exceptionally clear correlation in for CH_2D_2/MgO strongly suggests that this trend

is not spurious. The implication is that the features that obey this linear trend correspond to exactly one transition, while the outlying feature at 15 μeV corresponds to two or more closely separated transitions. In order to appear as one peak, these hypothetical transitions near 15 μeV must be separated by energies less than the resolution of the spectrometer (3 μeV). In that case, the width of the 15 μeV peak would then depend on both the separation and the widths of the component transitions. Presumably, each of the component transitions would individually follow the linear trend between width and energy transfer. If this trend is assumed to also apply to the CH_3D/MgO spectrum, then that would indicate that most, if not all, of the primary features identifies are composed of multiple tunneling transitions. This conjecture is supported by the apparent presence of multiplets within these peaks.

2.3.2 Pocket State Hamiltonian Matrices

The CH_4 rotational tunneling systems discussed in Section 2.1 all shared a common characteristic: a well defined crystal structure with only one unique rotationally ordered site. Such a definitive statement is not possible for CH_2D_2/MgO or CH_3D/MgO, because no diffraction data currently exists for the 2D monolayer of these systems. For the purposes of this study, it is assumed that the monolayer solids of both CH_2D_2 and CH_3D form a 2D C(2x2) commensurate lattice identical to that of CH_4/MgO, with the molecules sitting in a dipod orientation above uniform surface sites of fourfold symmetry and surrounded by four nearest neighbors rotated by 90°. This is a reasonable assumption for CH_2D_2/MgO, because the reduction in molecular symmetry to C_{2v} coincides with the rotational potential symmetry for CH_4's preferred dipod configuration on the MgO(100) surface. The assumption seems less certain for CH_3D/MgO due to the poor match between site and molecular symmetry.

If adsorbed CH_2D_2 is assumed to behave like CH_4, the molecule may occupy one of twelve PS's. A 12x12 Hamiltonian matrix encapsulating the symmetry relationships between these states can be constructed (Figure 52). However,

unlike the CH_4 case, where all twelve PS's are degenerate regardless of site symmetry, the orientations of CH_2D_2 on MgO can be separated into three nondegenerate groups of states as shown in Figure 53. The Hamiltonian consequently has three unique diagonal elements (D, H, & M) that correspond to the zero point librational energies of these orientations. States with deuterium atoms closest to the surface are expected to be lowest in energy due to at least two factors. First, a deuteron has a greater polarizabilty than a proton [75,76], resulting in a greater electrostatic interaction with the surface. Second, the asymmetry of the moments of inertia is stabilized by placing the heaviest atoms deeper in the potential well, as has been described for bulk CH_2D_2 [69]. The off-diagonal elements (O-DE's) represent the overlap integrals of neighboring PS wavefunctions. These can be divided into groups of identical elements that permute indistinguishable isotopes through rotational barriers of equivalent height and symmetry. For systems that exhibit translational tunneling within a generic double minimum potential well, it has been shown that asymmetries between minima less than 1% of the barrier height decrease the tunneling probability by as much as two orders of magnitude [65]. For the CH_3D/graphite system, similar calculations predicted that the O-DE corresponding to tunneling between nondegenerate PS's to be three orders of magnitude smaller than the other four unique O-DE's [71]. For this reason, CH_2D_2/MgO O-DE's relating nondegenerate orientations are set to zero. Diagonalizing this Hamiltonian matrix yields twelve nondegenerate sublevels (see Figure 54a). This diagram will be simplified further using symmetry arguments later in the discussion.

If CH_3D also adopts the same dipod orientation on MgO(100) as CH_4, then the twelve equilibrium orientations can be separated into two nondegenerate groups: The six states in which the deuteron points *up,* i.e. away from the surface, (hereafter referred to as U states) , and the six states in which the deuteron points *down,* toward the surface, (hereafter referred to as D states). The 12x12 Hamiltonian matrix for this system contains two unique diagonal elements (Figure 55). Again, the off-diagonal elements relating nondegenerate

orientations are set to zero. Furthermore, all O-DE's corresponding to two-fold reorientations are also neglected, as these have been shown to be negligible for systems in which the molecule contains true C_3 axes (i.e. CH_4 [51,64] and CH_3D/graphite [71,72]). Finally, diagonalization of the resulting matrix produces eigenvalues of A and E symmetry as shown in Figure 54b.

2.3.3 Calculation of CH_2D_2/MgO Transition Energies

The $H_A \rightarrow H_B$ and $D_A \rightarrow D_B$ transition energies of CH_2D_2/MgO were calculated using the variational method. Quaternion coordinates [77,78] are particularly useful for describing systems with multiple rotational frames of reference; therefore the CH_2D_2 system was modeled in quaternion space, Quaternions define points on the surface of a 3-sphere using coordinates τ_1, τ_2, τ_3, & τ_4 that obey the following identity:

$$\tau_1^2 + \tau_2^2 + \tau_3^2 + \tau_4^2 = 1. \qquad (\mathbf{20})$$

The identity quaternion $(\tau_1, \tau_2, \tau_3, \tau_4) = (0, 0, 0, 1)$ represents a reference rotational orientation; thus an orientation differing from the reference orientation by a rotation of φ about a unit vector $\mathbf{n} = (n_1, n_2, n_3)$ may be written as $(n_1 \cdot \sin(\varphi/2), n_2 \cdot \sin(\varphi/2), n_3 \cdot \sin(\varphi/2), \cos(\varphi/2))$.

For all molecules in H and D states, the C_2 molecular axis is aligned normal to the surface, and hence the corresponding rotational potentials are symmetrically equivalent. However, considering that the center of mass (com) for CH2D2 molecules is not the carbon atom but instead shifted toward the deuterons along the C_2 molecular axis, the com for a D state molecule is closer to the surface than for an H state molecule. D state molecules are therefore located deeper in the rotational potential well than H state molecules. Keeping these considerations in mind, the ansatz wavefunctions corresponding to both orientations are given the same functional form, but they are distinguished by the values of the potential strength parameter (discussed later). Because tunneling

between nondegenerate orientations is assumed to be negligible, these two transitions contain only two Hamiltonian elements (H & T_H or D & T_D, see Figure 52). Therefore only a reference PS (ψ_{ref}) and the PS corresponding to a C_2 rotation about the molecular axis (ψ_{C2}) are needed to calculate the transition energy transfers. Due to the localized nature of the PS's, Gaussian-like functions in quaternion space were employed as the ansatz wavefunctions. The corresponding wavefunctions given below also include a variational parameter (β) related to the width of the wavefunction (i.e. the extent to which it spills into the barrier):

$$\psi_{ref} = \exp\left(\beta \cdot \tau_4^2\right), \tag{21}$$

$$\psi_{C2} = \exp\left(\beta \cdot \tau_3^2\right). \tag{22}$$

The Hamiltonian operator was likewise expressed in quaternion coordinates. The kinetic energy operator (***T***) of an asymmetric top in quaternion space can be found in the literature (cf Equations 12, 16, and 17 in [53]). The potential was expanded into cubic rotator functions (CRF's) following the method described by Hüller and Kane [52]. Because only CRF's that are compatible with both the molecular and site symmetry contribute, most of the expansion coefficients are zero by symmetry. Earlier studies by Hüller and coworkers [52,55,64] have demonstrated that these expansions converge rapidly enough that truncation after one term is sufficient to approximate the system. The lowest order CRF with the requisite site and molecular symmetry (H^1_{33}) produces the following expression for the potential:

$$\mathbf{V}(\tau) = A \cdot \left(-\tau_1^2 - \tau_2^2 + \tau_3^2 + \tau_4^2\right), \tag{23}$$

where the expansion coefficient *A* is an adjustable parameter directly related to the strength of the potential. Solving the Schrödinger equation for the H (or D) PS's of A and B symmetry yields the energies E_A & E_B:

$$E_A = \frac{\langle \psi_{ref} | \mathbf{T} + \mathbf{V} | \psi_{ref} \rangle + \langle \psi_{ref} | \mathbf{T} + \mathbf{V} | \psi_{C2} \rangle}{\langle \psi_{ref} | \psi_{ref} \rangle + \langle \psi_{ref} | \psi_{C2} \rangle}, \quad \textbf{(24)}$$

$$E_B = \frac{\langle \psi_{ref} | \mathbf{T} + \mathbf{V} | \psi_{ref} \rangle - \langle \psi_{ref} | \mathbf{T} + \mathbf{V} | \psi_{C2} \rangle}{\langle \psi_{ref} | \psi_{ref} \rangle - \langle \psi_{ref} | \psi_{C2} \rangle}. \quad \textbf{(25)}$$

Integration is performed over the quaternion coordinates, thereby leaving only the parameters *A* and *β*. A range of potential strengths corresponding to 10-300 times the average rotational constant of CH_2D_2 (B = 436 μeV) were explored for *A*, and then the energy levels were minimized with respect to the variational parameter *β*. Figure 56 shows the calculated $H_A \leftrightarrow H_B/D_A \leftrightarrow D_B$ splitting as a function of *A*.

2.4 Discussion

2.4.1 Allowed Transitions for CH_2D_2 &. CH_3D

In earlier studies of the CH_4 systems, the rotational PS wavefunctions were combined with the nuclear spin state wavefunctions to calculate the intensities of peaks in the INS spectra [51,54]. It was shown that three nuclear spin species exist for CH_4 (A, T, & E) with nuclear spins I = 2, I = 1, & I = 0. Since I = ±½ for neutrons, A→E and E→A transitions (ΔI = ±2) between rotational PS's are forbidden in INS. A qualitative analysis of the nuclear spins allows the determination of whether any transitions are INS-forbidden for these systems. For CH_2D_2 and CH_3D, there are 36 (A & B symmetries) and 24 (A & E symmetries) respective nuclear spin functions. In order for any INS transitions to be forbidden (ΔI > 1), there must be at least three unique symmetries of nuclear spin functions. Since only two spin symmetries exist for both of these isotopologues, no transitions are truly forbidden, although some may be too weak to observe.

The goal of the following discussion is to compare the experimental spectra to the tunneling diagrams in Figure 54. As described in Section 2.3.1, analysis of the peak widths supports the notion that all but one of the observed spectral features in the CH_2D_2/MgOspectrum are likely due to single transitions. The relative simplicity of this spectrum argues for a much simpler tunneling scheme than the one shown in (Figure 54a). In the spirit of Ockham's razor, this diagram will be simplified by including only the minimum number of PS Hamiltonian O-DE's necessary to account for the observed transitions. In other words, the most probable tunneling transitions will be identified. For the CH_3D/MgO spectrum, however, most—if not all—of the features are likely composed of multiple irresolvable transitions. The apparent complexity of the CH_3D/MgO spectrum strongly argues for the presence of more tunneling sublevels within the ground librational state when compared to the CH_2D_2/MgO system. This is not surprising at all when the site and molecular symmetries are considered. The relative

simplicity of the CH_2D_2/MgO spectrum is consistent with the complementary molecular and potential symmetries (i.e. both are two-fold). In contrast, the frustrated symmetry of the CH_3D system (two-fold site symmetry and three-fold molecular symmetry) should produce a more complex RTS.

2.4.2 Simplifying the CH_2D_2 Model

For CH_2D_2/MgO, if every element in the PS Hamiltonian contributed significantly to the RTS (including those between nondegenerate PS's), then the resulting tunneling manifold would have twelve nondegenerate states with 66 transitions between these states. The observed RTS clearly does not support this description of the system. Given the extremely low tunneling probability of quantum particles (or groups of particles in this case) between nondegenerate states [65], the O-DE's connecting orientations of different energy were obvious candidates for exclusion and were already set to zero in producing the PS Hamiltonian matrix. This step is also empirically justified; the RTS of the CH_3D/graphite system showed no evidence of transitions between states of nondegenerate orientations [70,71]. The tunneling diagram still has twelve nondegenerate states, but only one transition is possible for molecules in the D or H states. Molecules in an M state, however, still may tunnel to one of seven other M states, resulting in 27 possible M→M transitions—still far more than are observed.

Considering the two-fold molecular symmetry of CH_2D_2, it is reasonable to assume that there is a significant barrier to three-fold reorientation and hence negligible tunneling probability about any C-H or C-D bond. Half of the C_3 elements transform an M state into an H or D state (or vice versa) and were eliminated in the constructing Figure 52. The remaining C_3 elements (labeled t_1, t_2, t_3, & t_4) transform one M state into another M state that is distinguishable from the original by the relative positions of H and D atoms, as is shown in Figure 57a. In that figure, a molecule in an M state is rotated 120° about the bond between carbon and the deuteron pointed toward the surface (labeled D1). Threefold

rotation in one direction produces a D state configuration. Rotation in the opposite direction results in an M state in which the upper H and D atoms are reversed from their original orientation. For an isolated molecule in an idealized C_2 potential, these two configurations will be degenerate. However, when nearest-neighbor interactions are taken into account, it is clear that this degeneracy is dependent on the orientations of adjacent molecules. As shown in Figure 57b, these two M states cannot be degenerate unless nearest-neighbor orientations have C_2 symmetry with respect to the reference molecule. In that figure, the bottommost reorientation shows a hypothetical case in which nn orientations are asymmetric. In the initial state, two of shortest the atom-atom interactions are between two hydrogen atoms (H-H) and two are between two deuterium atoms (D-D). For final state, these four interactions are H-H, D-D, and H-D (x2). Moreover, even in cases where nearest-neighbor orientations are symmetric about the C_2 axis of the reference molecule, the possibility remains that local asymmetries due to surface defects and orientations of more distant neighbors will break this degeneracy and suppress tunneling between these two states. When only two-fold reorientations of the molecule are allowed (i.e. all C_3 elements set to zero in the PS Hamiltonian), the result is four doubly degenerate M states (Figure 58a). There are six possible transitions with these proposed M sublevels, or eight total transitions those within the H and D sublevels are included. Since three of the four peaks within the INS spectrum are ascribed to single transitions, this leads to the conclusion that the remaining five are either part of the 15 μeV peak or are not observed. This is not a satisfying explanation of the experimental spectrum, and the possibility that some of the C_2 O-DE's might also be negligible should be considered.

It should be noted that some of the C_2 O-DE's relate distinguishable M states in a similar manner to C_3 O-DE's. This is because while a tetrahedron has three C_2 axes, for CH_2D_2 has only one true axis of molecular symmetry. Henceforth the other two will be referred to as "virtual" C_2 axes. For molecules in an M orientation, one of the virtual axes is perpendicular to the surface while the other

is parallel to the surface. Reorientations about these axes are denoted by respective O-DE's $T_{\perp}$ and $T_{\parallel}$ in the PS Hamiltonian. Only rotation about the true molecular axis produces a state identical to the original, so this is clearly the most probable reorientation. However, including only these elements (denoted T) does not sufficiently describe the observed spectrum, as shown in Figure 58b. Only three transitions between degenerate states are possible, whereas the experimental RTS shows evidence for at least four (probably more when the width at 15 μeV is considered). Therefore reorientations about one (and only one) of the two virtual axes must be included.

Similar effects on the tunneling diagram are seen regardless of which virtual axis O-DE is omitted: Two of the three spacings between adjacent M levels become equal. Although the resulting diagram still has four M sublevels, two pairs of transitions are necessarily identical in energy, leading to a total of six unique transition energies once the H & D states are included. Since the spectrum offers no clues as to whether $T_{\perp}$ or $T_{\parallel}$ should be neglected, the nature of contributions to the rotational potential from both the surface and neighboring adsorbate molecules must be considered.

Molecule-molecule contributions stabilize the lateral orientation of a reference M state CH_2D_2 molecule, preventing reorientations about the vertical virtual axis, while attraction to the surface stabilizes the molecule vertically, preventing rotation about the parallel axes. Taking the vertical dependence of the strength of the surface potential into account, comparison to the translational double minimum analogy suggest $T_{\parallel}$ should be the discarded element, because even small barrier asymmetries dramatically suppress tunneling probability [65]. However, empirical examples to the contrary do exist. For both CH_4 and CH_3D on graphite [67,71], the barrier to rotation about the surface-normal axis was found to be larger than that to rotation about an oblique axis, indicating that the lateral adsorbate contributions are dominant. If applied to CH_2D_2/MgO, this would suggest that $T_{\perp}$ rather than $T_{\parallel}$ should be neglected. However, a reference molecule in the C(2x2) lattice for methane on MgO has only four nearest

neighbors, as opposed to six for a molecule within the 2D methane/graphite lattice. Moreover, the 2D lattice constant of the commensurate methane monolayer is 4.26 Å on graphite compared to 5.95 Å on MgO, meaning molecules are spaced further apart by a factor of 1.4 on MgO than on graphite: Considering that the attractive portion of the Lennard-Jones potential decreases with r^6 and that there are 1.5 times as many nn molecules on graphite, the lateral contribution to the rotational potential from nn's on MgO would be expected to be less than 10% than on graphite. This also partially explains the larger energy window of the CH_4/MgO RTS compared to CH_4/graphite (i.e lower V/B). With these considerations in mind, $T_{\parallel}$ was set to zero to produce the sublevel diagram shown in Figure 58c. Note that the M sublevels only include the O-DE's T and $T_{\perp}$, corresponding to reorientation about the molecular and potential C_2 axes of symmetry.

2.4.3 Peak Assignments for CH_2D_2

Not only does the diagram in Figure 58c provides a reasonable number of transitions given the observed CH_2D_2 spectrum, it also explains other aspects of the observed transition energies. For example, the sum of the energy transfers of two of the peaks (15 & 31 μeV) is approximately equal to the energy transfer of a third (45 μeV). Meanwhile, the sublevel diagram predicts one of the transitions ($M_1 \rightarrow M_4$) to be a combination of two others ($M_1 \rightarrow M_2$ & $M_2 \rightarrow M_4$, or alternatively $M_1 \rightarrow M_3$ & $M_3 \rightarrow M_4$). Hence the transitions of energy $2T_{\perp}$ and 2T are assigned to the peaks at 15 and 31 μeV. The $M_1 \rightarrow M_4$ transition ($2T + 2T_{\perp}$) would then correspond to the 45 μeV peak, while the $M_2 \rightarrow M_3$ transition ($2T - 2T_{\perp}$) should occur at ≈15 μeV. That $T_{\perp}$ should approximately (but not identically) equal $T - T_{\perp}$ is a fortunate coincidence: This provides an explanation for the anomalous width of the 15 μeV peak. Presumably this feature is actually a combination of these two transitions at two closely spaced, yet distinct, energy transfers of 2T and

2T - 2T⊥. Table 10 summarizes the energy transfers of the transitions between M states predicted by this model in terms of the Hamiltonian matrix elements as well as their corresponding assignments to the observed spectrum.

Table 10. Assignment of CH_2D_2 M state transitions.

Transition	Energy	Assignment
$M_1 \rightarrow M_2$	2T⊥	15 μeV
$M_1 \rightarrow M_3$	2T	31 μeV
$M_1 \rightarrow M_4$	2T + 2T⊥	45 μeV
$M_2 \rightarrow M_3$	2T - 2T⊥	16 μeV
$M_2 \rightarrow M_4$	2T	31 μeV
$M_3 \rightarrow M_4$	2T⊥	15 μeV

Assignments are color coded to match the M state transitions shown in Figure 58c. Energies are given in terms of the matrix elements in Figure 52.

Transitions within the M block then account for all of the observed features except for the one at 127 μeV. This must then be attributed to either the $H_A \rightarrow H_B$ or $D_A \rightarrow D_B$ transition. The H states—highest in energy—occupy the shallowest wells of the rotational potential, and therefore their splitting should occur at the largest energy transfer. Thus the 127 μeV peak is assigned to $H_A \rightarrow H_B$. This peak is also the weakest in intensity, which is sensible considering that the H states should be the least populated at these temperatures. Referring to Figure 56, this assignment corresponds to a potential strength of 18.9B (8.25 meV) for molecules in the H configuration. Similarly, the $D_A \rightarrow D_B$ transition should be at the lowest energy transfer, as the D states are lowest in energy (i.e. deepest

potential well). One possible explanation for its absence could be that it occurs at less than 3 μeV and is buried within the elastic line. If this were the case, then the D transition—if of sufficient intensity—might be detected as increased width in the elastic line. With this in mind, the elastic peaks of the vanadium scan and the CH_2D_2/MgO spectrum are plotted in Figure 59. The difference in widths between the two elastic peaks is negligible; and that the vanadium elastic line is actually 1.9% wider than the CH_2D_2 peak. Therefore there is no evidence that the D transition the lies within the elastic line. Nor, however, is it definitive proof to the contrary: It may well exist but be too weak in intensity relative to the elastic line to be detected. For the purposes of calculating the potential strengths, it will be assumed that this is the case, and that it occurs at an energy transfer of less than 3 μeV (the resolution of BASIS).

In this assignment, the variational calculations predict a potential strength of greater than 41.0 meV. These H state and D state transition assignments are summarized in Table 11.

Table 11. $H_A \rightarrow H_B$ & $D_A \rightarrow D_B$ transition assignments.

Transition	**Assignment**	**Potential. Strength**
$H_A \rightarrow H_B$	127 μeV	8.25 meV
$D_A \rightarrow D_B$	< 3 μeV	> 36.7 meV

The two-site PS model used in the study of Phase III partially deuterated methanes [69] calculated differences ~10% in absolute potential strength among the three isotopologues, increasing with molecular weight. Using the experimental CH_4-MgO INS spectrum, the strength of the rotational potential has been calculated to be 10.03 meV for that system [26]. In this work, the calculated potential for the H states of CH_2D_2 (8.25 meV) is about 18% *less* than

that calculated for CH_4 on MgO. As the CH_4 work used spherical harmonic wavefunctions and a potential expanded in terms of Wigner functions, this discrepancy is likely attributable to the different methods used. Another point of interest regarding the CH_4/MgO studies [23,26,30] is the splitting between T levels. If the two-fold matrix elements for this system are assumed negligible, then the three T levels would be evenly spaced. However, the INS data shows discrepancies of approximately 20 μeV. If this is attributed to contributions from the C_2 overlaps, then two-fold matrix elements for CH_4/MgO are of the same order of magnitude (~10 μeV) as those for the M states for the CH_2D_2/MgO model presented here. The corresponding H state element is about five times greater, and the D state element is at least five times less.

2.4.4 Conclusions

The major features of the CH_2D_2/MgO rotational tunneling spectrum presented here are examined using by plotting peak width versus energy transfer, and linear relationship is interpreted to mean that all peaks except one are attributable to individual tunneling transitions. A pocket state formalism is applied, and molecular orientations are found to exist in three nondegenerate groups. Inclusion of all possible tunneling reorientations results in tunneling diagrams that predict far more transitions than are observed, so the model is simplified to include only 180° molecular reorientations about axes aligned with the C_2 symmetry axes of the molecule and/or rotational potential. Agreement between the theoretically predicted transition energy transfers and experiment is reasonably good. The one anomalously wide peak is attributed to a convolution of two transitions at two closely spaced energy transfers. The only feature predicted by the model that is not observed is the transition between D tunneling sublevels. Within the model, these states should experience the strongest rotational potential, and hence exhibit the smallest tunneling splitting. However, analysis of the widths of the elastic line showed no increase compared to that of the vanadium scan.

Comparison of the CH_2D_2/MgO spectrum and its theoretical interpretation provide some interesting results with respect to other methane RTS. For example, configurations in which the molecular and potential symmetry axes are perpendicular (i.e. the M states) produce evenly spaced sublevels, much like the T states in CH_4/MgO. The peak assignments of the M states provide estimates of the twofold overlap elements of the pocket state Hamiltonian matrix, the magnitudes of which suggest that asymmetries within the T levels of the CH_4/MgO spectrum might be due to tunneling through barriers of twofold symmetry. Additionally, variational calculations of the interaction potential strength for molecular configurations in which the C_2 molecular axis aligns with that of the rotational potential (i.e. the H and D states) provide reasonable values compared to other the RTS of other deuterated methane isotopologues. The fact that the spectrum can be described so well exclusively in terms of twofold reorientation is significant in and of itself, because previously only threefold pocket state overlaps were thought to contribute appreciably to methane rotational tunneling.

The trend between peak width and energy transfer was much more ambiguous for the CH_3D/MgO spectrum, and this was interpreted to mean that many of the observed features were convolutions to multiple transitions. The indeterminate number of transitions significantly complicates matching theoretical predictions from the PS Hamiltonian to the observed spectral features. Additionally, due to the mismatch between site and potential symmetry, more parameters must be included in any expansion of the potential. Therefore, variational calculations similar to those presented here for CH_2D_2/MgO would be much more cumbersome. As a result of these factors, comparatively little theoretical work and analysis is performed for the CH_3D/MgO system. However, a few comments concerning the peak at 150 μeV energy transfer will be made here: First, it occurs at the highest energy transfer (i.e. lowest V/B) of any of the observed features, indicating that it likely involves three-fold reorientation about the C-D axis (i.e. transitions in the tunneling diagram in which either d↑ or d↓

terms do not cancel). Second, it is of the greatest intensity than any others observed, indicating a relatively high tunneling frequency. Intriguingly, this intensity is equally high on the energy gain and energy loss sides of the elastic line, indicating that this high frequency is not due to low temperature detailed balance effects.

The models described here rest on two key assumptions: 1) The structure of the 2D lattice is the same as that for CH_4/MgO, and 2) Molecules do not tunnel between nondegenerate orientations. These assumptions appear justified for the CH_2D_2/MgO spectrum given the relative simplicity and the fairly good agreement of the spectral lines with the PS tunneling diagram. These assumptions seem less certain for CH_3D/MgO. The mismatch between molecular and site symmetry clearly adds complexity to the spectrum. This complexity might not be the result of a dipod molecular configuration, as it conceivably could also be explained by the mismatch in symmetry from a tripod-down or even tripod up configuration on the square MgO lattice. Similarly, this symmetry mismatch might also result in an intermingling of sublevels between equilibrium pocket state orientations of high and low energy in the infinite V/B limit.

The former assumption can easily be tested via neutron diffraction experiments of the monolayer solid, as have been done for several CH_4 lattices. The latter assumption might be tested by DFT calculations of the energies of the two pocket state orientations predicted by this model. If the difference in energy is even ~1%, then tunneling between nondegenerate minima will likely be suppressed. Both assumptions might also be verified by further INS studies focusing on the detailed balance of the spectra. If the sample is cooled as close to absolute zero as possible for an extended period of time before measurement, then presumably most molecules will be in the ground tunneling sublevel. Differences in intensity between the energy gain and energy loss sides of the elastic line could be used to identify transitions from the ground state. This should considerably simplify interpretation of the CH_3D/MgO spectrum. Moreover, this technique would be also useful for CH_2D_2/MgO, since according to

this model the D transition (lowest energy) is not observed. If this model is correct, the result should be a comparatively barren spectrum, with only increased width on the energy loss side of the elastic line of the elastic line.

LIST OF REFERENCES

[1] Y. Larher, in *Surface Properties of Layered Structures*, edited by G. Benedek (Kluwer Academic, Dordrecht ; Boston, 1992).
[2] K. S. W. Sing, Pure and Applied Chemistry **57**, 603 (1985).
[3] I. Langmuir, J. Am. Chem. Soc. **38**, 2221 (1916).
[4] E. A. Flood, *The Solid-gas Interface* (Edward Arnold; Dekker, London, New York, 1967).
[5] S. J. Gregg, *Adsorption, Surface Area, and Porosity*, 2nd ed (Academic Press, London ; New York, 1982).
[6] V. Ponec, *Adsorption on Solids* (Butterworths, London, 1974).
[7] F. Rouquerol, *Adsorption by Powders and Porous Solids: Principles, Methodology, and Applications* (Academic Press, San Diego, 1999).
[8] S. Brunauer, P. Emmett, and E. Teller, J. Am. Chem. Soc. **60**, 309 (1938).
[9] J. E. Lennard-Jones, Physica **4**, 941 (1937).
[10] G. Halsey, Advances in Catalysis **4**, 259 (1952).
[11] G. Halsey, The Journal of Chemical Physics **16**, 931 (1948).
[12] T. Hill, Advances in Catalysis **4**, 211 (1952).
[13] J. Dash, Physical Review B **15**, 3136 (1977).
[14] S. Blundell, *Concepts in Thermal Physics* (Oxford University Press, Oxford ; New York, 2006).
[15] H. E. Stanley, *Introduction to Phase Transitions and Critical Phenomena* (Oxford University Press, New York, 1987).
[16] A. Thomy, X. Duval, and J. Regnier, Surface Science Reports **1**, 1 (1981).
[17] Y. Larher, Journal of Colloid and Interface Science **37**, 836 (1971).
[18] Y. Larher, The Journal of Physical Chemistry **72**, 1847 (1968).
[19] Y. Larher and D. Haranger, Surface Science **39**, 100 (1973).
[20] Y. Nardon and Y. Larher, Surface Science **42**, 299 (1974).
[21] F. A. Putnam and T. Fort, The Journal of Physical Chemistry **79**, 459 (1975).
[22] A. Thomey and X. Duval, J Chim Phys **67**, 1101 (1970).
[23] J. Z. Larese, Physica B: Condensed Matter **248**, 297 (1998).
[24] A. Freitag and J. Larese, Physical Review B **62**, 8360 (2000).
[25] J. Coulomb, K. Madih, B. Croset, and H. Lauter, Physical Review Letters **54**, 1536 (1985).
[26] J. Z. Larese, J. M. Hastings, L. Passell, D. Smith, and D. Richter, The Journal of Chemical Physics **95**, 6997 (1991).
[27] M. Drummond, B. Sumpter, W. Shelton, and J. Larese, Physical Review B **73**, (2006).
[28] L. Bruch and J. Larese, Physical Review B **85**, (2012).
[29] M. L. Drummond, B. G. Sumpter, W. A. Shelton, and J. Z. Larese, The Journal of Physical Chemistry C **111**, 966 (2007).
[30] J. Larese, D. y Marero, D. Sivia, and C. Carlile, Physical Review Letters **87**, (2001).

[31] T. Arnold, R. E. Cook, and J. Z. Larese, The Journal of Physical Chemistry B **109**, 8799 (2005).
[32] T. Arnold, A. Barbour, S. Chanaa, R. E. Cook, D. Fernandez-Canato, P. Landry, T. Seydel, P. Yaron, and J. Z. Larese, The European Physical Journal Special Topics **167**, 143 (2009).
[33] T. Arnold, R. E. Cook, S. Chanaa, S. M. Clarke, M. Farinelli, P. Yaron, and J. Z. Larese, Physica B: Condensed Matter **385–386, Part 1**, 205 (2006).
[34] P. J. Linstrom and W. G. Mallard, *NIST Chemistry WebBook, NIST Standard Reference Database Number 69* (National Institute of Standards and Technology, Gaithersburg MD, 20899, n.d.).
[35] W. Kunnman and J. Z. Larese, U.S. Patent No. 6179897 (2001).
[36] A. Freitag and J. Larese, Physical Review B **62**, 8360 (2000).
[37] T. Arnold, R. E. Cook, and J. Z. Larese, The Journal of Physical Chemistry B **109**, 8799 (2005).
[38] Z. Mursic, M. Y. M. Lee, D. E. Johnson, and J. Z. Larese, Review of Scientific Instruments **67**, 1886 (1996).
[39] Accelrys Software Inc., *Materials Studio Release Notes, Release 6.0* (Accelrys Software Inc., San Diego, CA, 2011).
[40] H. Sun, The Journal of Physical Chemistry B **102**, 7338 (1998).
[41] A. A. Samoletov, C. P. Dettmann, and M. A. J. Chaplain, Journal of Statistical Physics **128**, 1321 (2007).
[42] S. Nosé, Progress of Theoretical Physics Supplement **103**, 1 (1991).
[43] B. Leimkuhler, E. Noorizadeh, and O. Penrose, Journal of Statistical Physics **143**, 921 (2011).
[44] P. Hohenberg and B. Halperin, Reviews of Modern Physics **49**, 435 (1977).
[45] R. Gangwar and R. Suter, Physical Review B **42**, 2711 (1990).
[46] R. Gangwar, N. Colella, and R. Suter, Physical Review B **39**, 2459 (1989).
[47] N. Colella and R. Suter, Physical Review B **34**, 2052 (1986).
[48] A. Thorny and X. Duval, Surface Science **299-300**, 415 (1994).
[49] Yung Fang Yu Yao, J. Phys. Chem. **65**, 2472 (1965).
[50] N. Norman, H. Mathisen, A. F. Andresen, M. Olli, and Å. Pilotti, Acta Chemica Scandinavica **26**, 3913 (1972).
[51] W. Press, *Single-particle rotations in molecular crystals* (Springer-Verlag, Berlin; New York, 1981).
[52] A. Hüller and J. Kane, The Journal of Chemical Physics **61**, 3599 (1974).
[53] A. Hüller, M. Prager, W. Press, and T. Seydel, J Chem Phys **128**, 034503 (2008).
[54] A. Hüller and W. Press, Physical Review B **24**, 17 (1981).
[55] A. Hüller and J. Raich, The Journal of Chemical Physics **71**, 3851 (1979).
[56] R. Pynn, *A Neutron Primer* (Los Alamos Science, Los Alamos, NM, 1990).
[57] H. M. James and T. A. Keenan, The Journal of Chemical Physics **31**, 12 (1959).
[58] T. Yamamoto, The Journal of Chemical Physics **48**, 3193 (1968).
[59] W. Press, The Journal of Chemical Physics **56**, 2597 (1972).

[60] H. Kappulla and W. Glaeser, *Inelastic Scattering of Neutrons in Solids and Liquids* (IAEA, Vienna, 1973).
[61] W. Press and A. Kollmai, Solid State Communications **17**, 405 (1975).
[62] A. Heidemann, The Journal of Chemical Physics **75**, 4003 (1981).
[63] A. Hüller, Physical Review B **16**, 1844 (1977).
[64] A. Hüller and D. M. Kroll, The Journal of Chemical Physics **63**, 4495 (1975).
[65] M. D. Harmony, Chemical Society Reviews **1**, 211 (1972).
[66] G. Bomchil, A. Huller, T. Rayment, S. J. Roser, M. V. Smalley, R. K. Thomas, J. W. White, and A. D. Buckingham, Philosophical Transactions of the Royal Society B: Biological Sciences **290**, 537 (1980).
[67] M. V. Smalley, A. Hüller, R. K. Thomas, and J. W. White, Molecular Physics **44**, 533 (1981).
[68] P. J. Stimac and R. J. Hinde, The European Physical Journal D **46**, 69 (2007).
[69] K. J. Lushington, The Journal of Chemical Physics **75**, 4010 (1981).
[70] A. Inaba, J. Skarbek, J. R. Lu, R. K. Thomas, C. J. Carlile, and D. S. Sivia, The Journal of Chemical Physics **103**, 1627 (1995).
[71] P. C. Ball, A. Inaba, J. A. Morrison, M. V. Smalley, and R. K. Thomas, The Journal of Chemical Physics **92**, 1372 (1990).
[72] K. Maki, The Journal of Chemical Physics **74**, 2049 (1981).
[73] E. Mamontov and K. W. Herwig, Review of Scientific Instruments **82**, 085109 (2011).
[74] C. F. Koehler and J. Z. Larese, Review of Scientific Instruments **71**, 324 (2000).
[75] V. I. Goldansky, O. A. Karpukhin, A. V. Kutsenko, and V. V. Pavlovskaya, Nuclear Physics **18**, 473 (1960).
[76] N. Rodning, L. Knutson, W. Lynch, and M. Tsang, Physical Review Letters **49**, 909 (1982).
[77] W. R. Hamilton, *Lectures on Quaternions* (Dublin, Hodges and Smith, 1853).
[78] A. Hanson, *Visualizing quaternions* (Morgan Kaufmann ; Elsevier Science [distributor], San Francisco, CA; Amsterdam; Boston, 2006).

APPENDIX

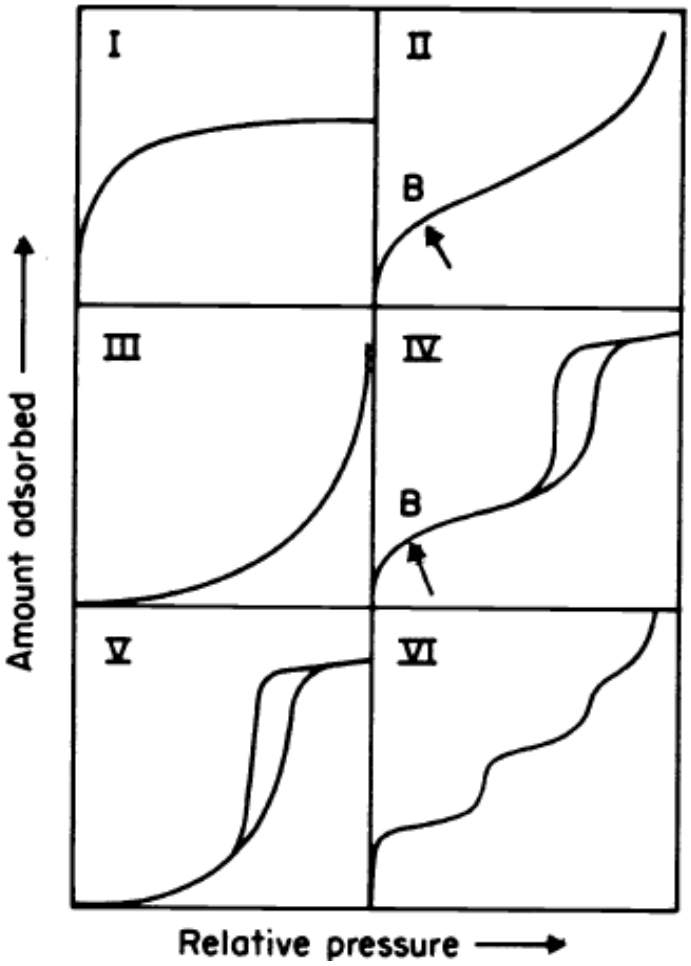

Figure 1. IUPAC Classification of Isotherms

From Reference [2].

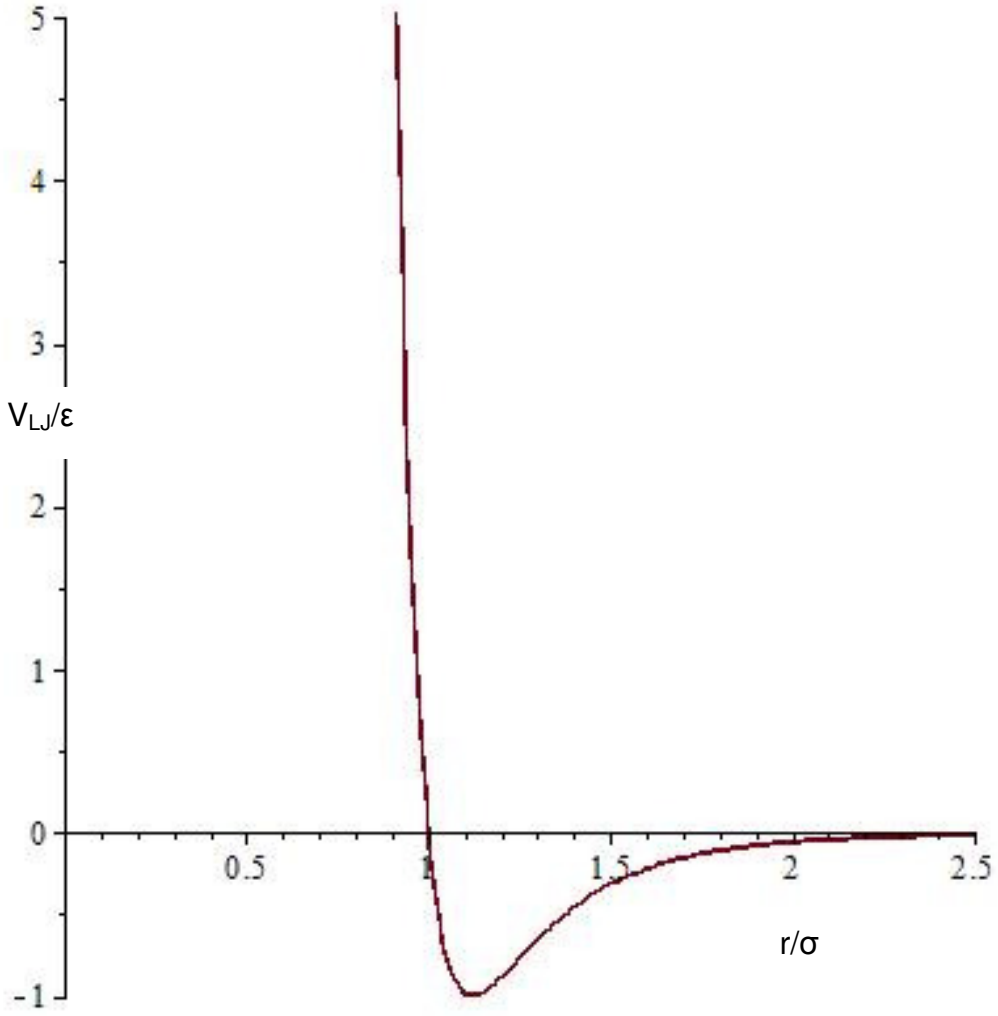

Figure 2. The Lennard-Jones Potential.

The L-J potential forms a well due to counteracting attractive and repulsive terms. This well reaches its minimum of $-\varepsilon$ *at* $r_m = 2^{1/6}\sigma$.

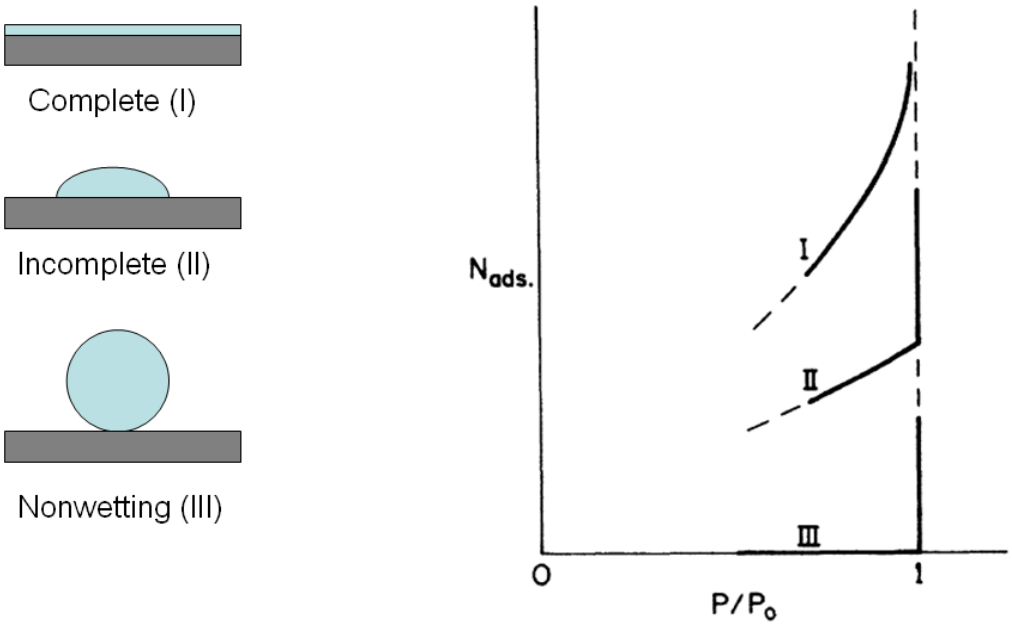

Figure 3. Types of Wetting & Corresponding Isotherms.

Right-most figure from Reference [13].

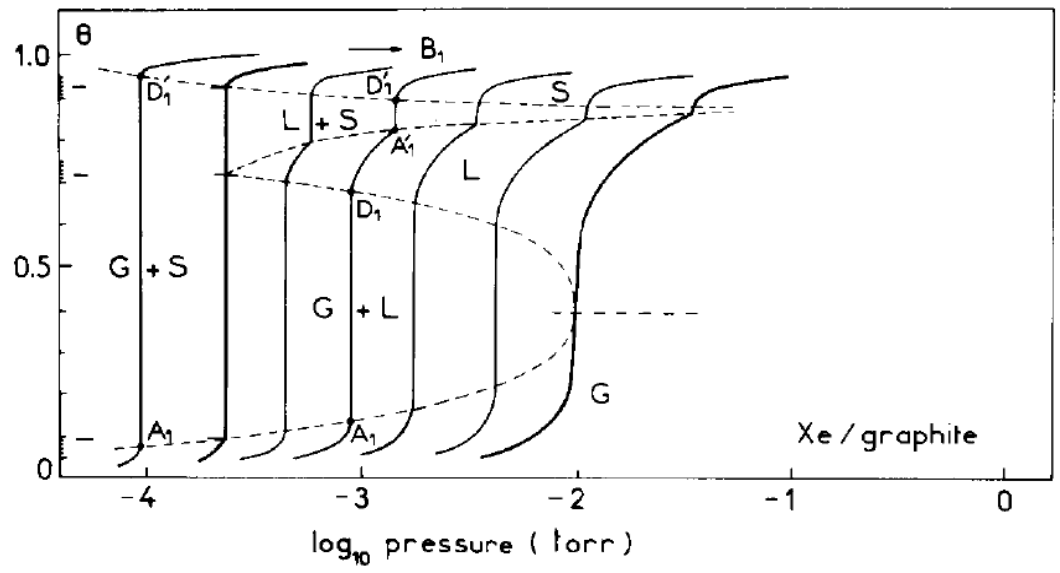

Figure 4. Phase Diagram for 1st Layer of Xe/Graphite.

The 2D critical point of condensation is at the temperature of the right-most isotherm, where the riser ceases to be vertical. The substep bound by points A_1' and D_1' indicates an additional phase transition (2D liquid → 2D solid). From Reference [16].

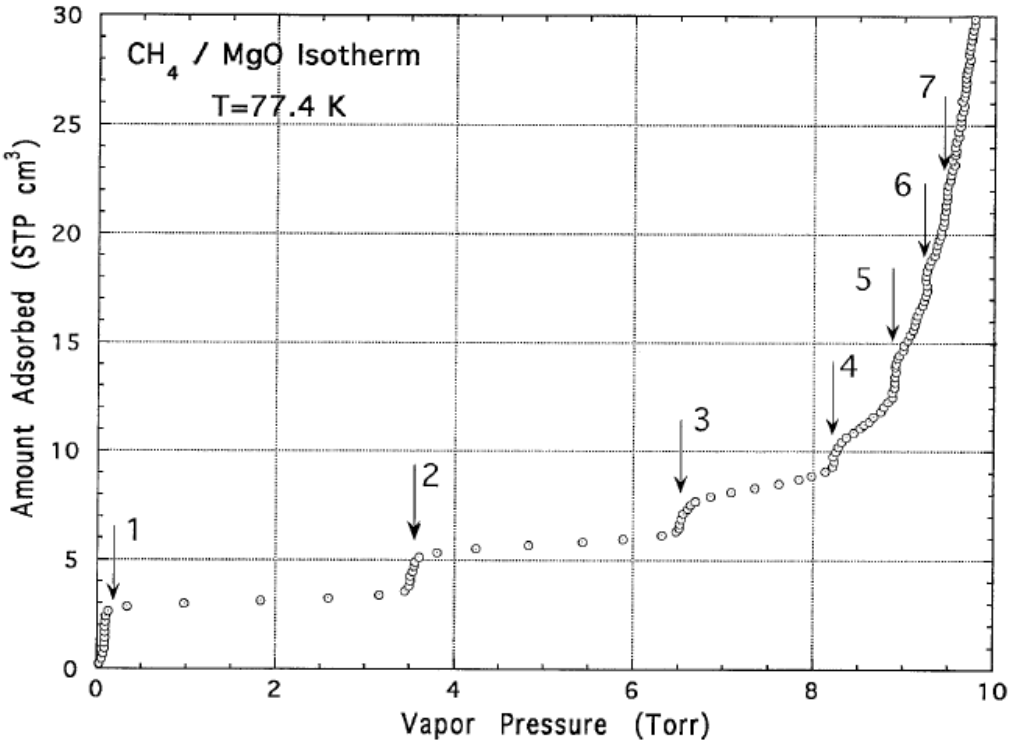

Figure 5. CH_4/MgO isotherm Showing Seven Distinct Layers.

From Reference [23].

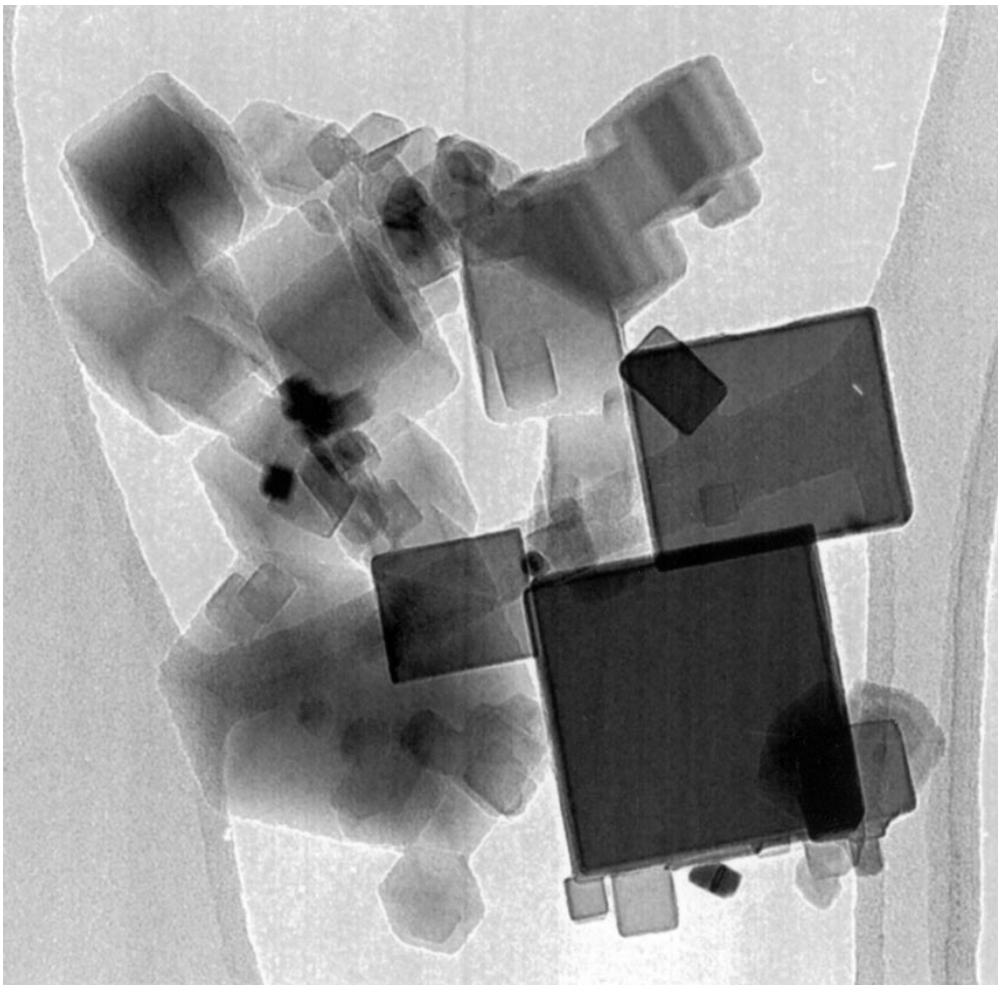

Figure 6. TEM Image of MgO(100) Nanocubes.

This image of MgO(100).nanocubes produced using the Kunnman-Larese method is from Reference [23]*. The largest cube has an edge length of ≈200 nm.*

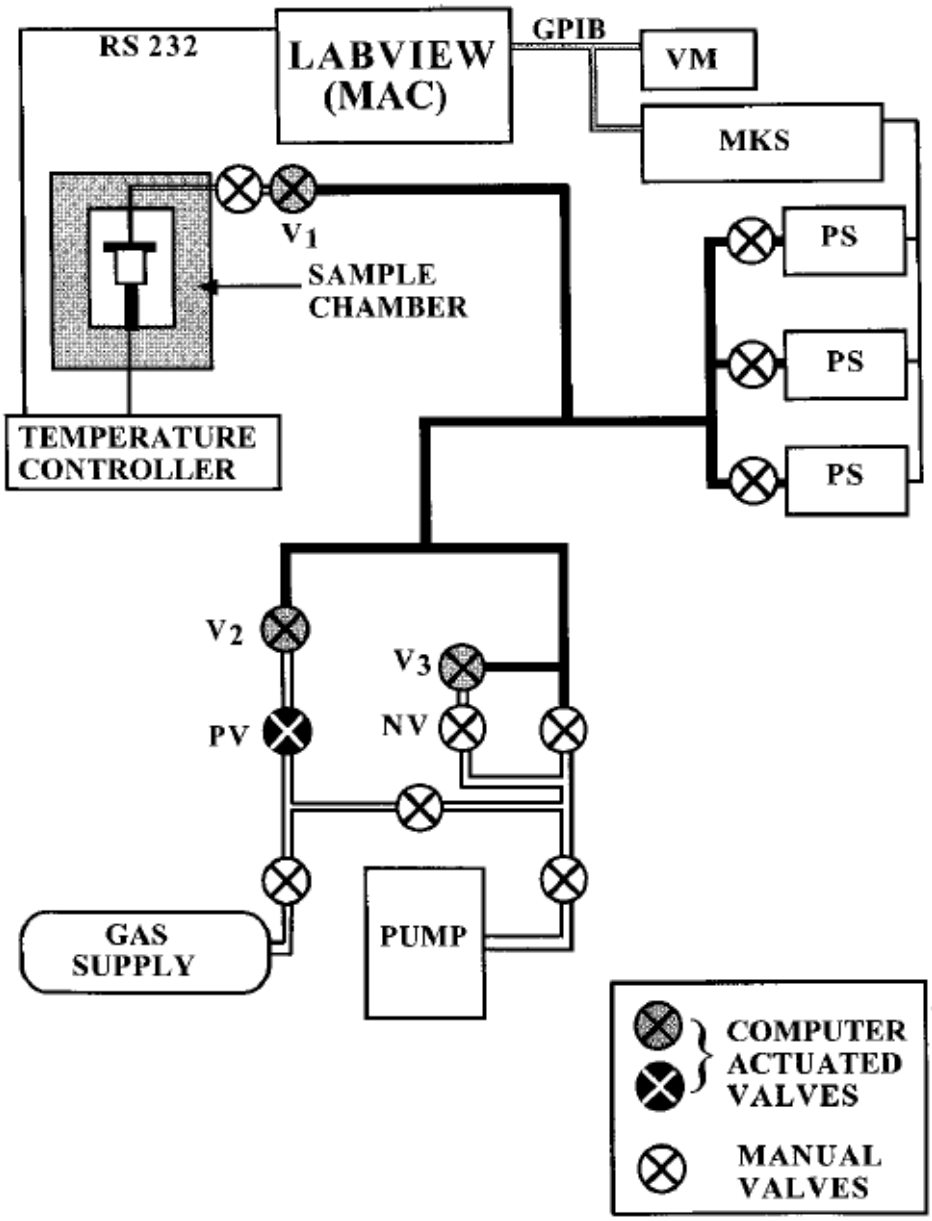

Figure 7. Schematic of Adsorption Isotherm Apparatus.

From Reference [38]. *A detailed description of components can be found therein.*

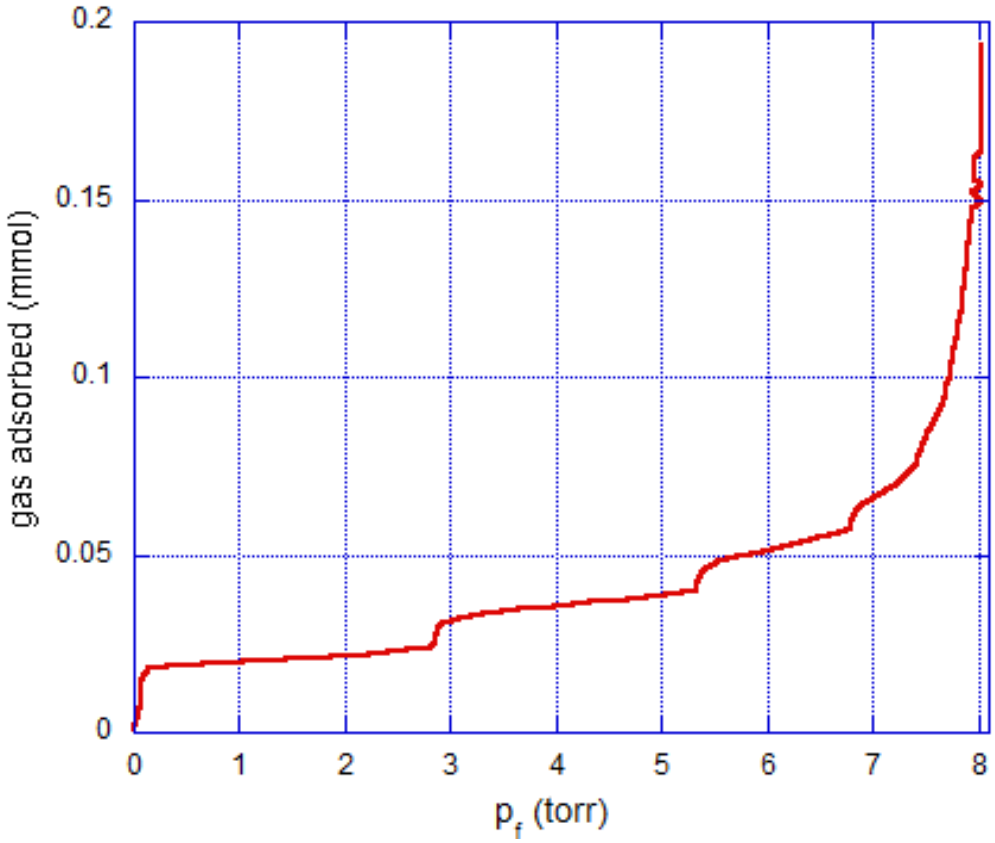

Figure 8. Representative CH_4 Isotherm.

This was performed at ≈77K. Five steps of the same approximate height are visible, indicating that this MgO sample is of high quality.

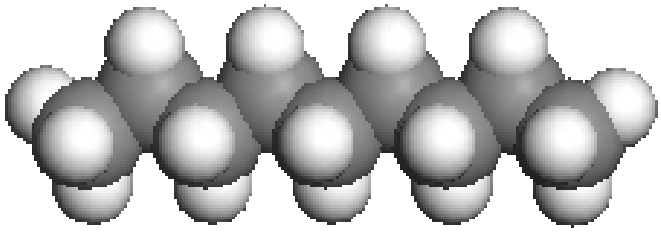

(a)

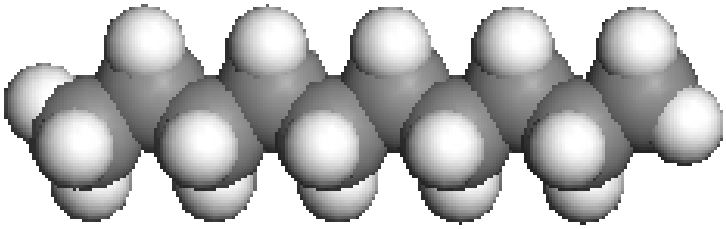

(b)

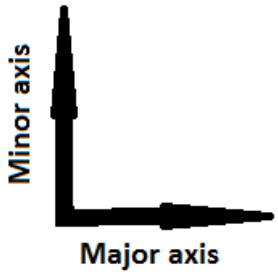

Figure 9. Structures of Adsorbates.

(a) n-nonane.

(b) n-decane.

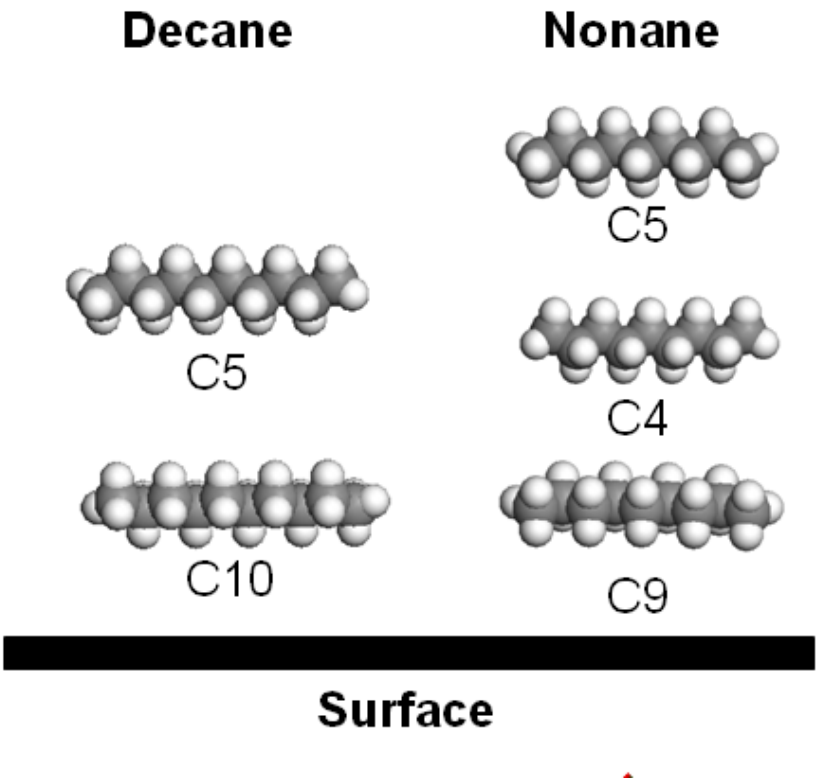

Figure 10. Minor Axis CBB Orientations.

Side view of high symmetry minor axis ccb orientations of nonane and decane..

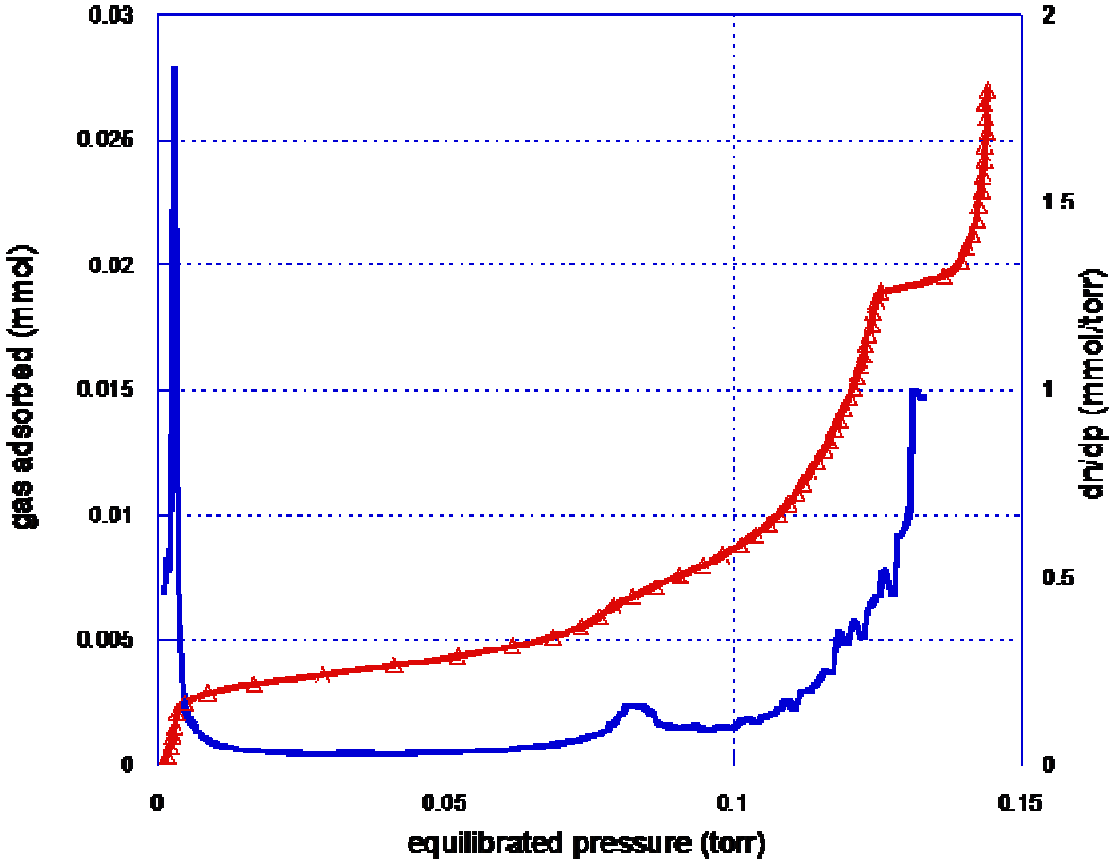

Figure 11. Representative Nonane Isotherm.

*Nonane isotherm at 253.85K (*red*) plotted next to its numerical derivative (*blue*).*

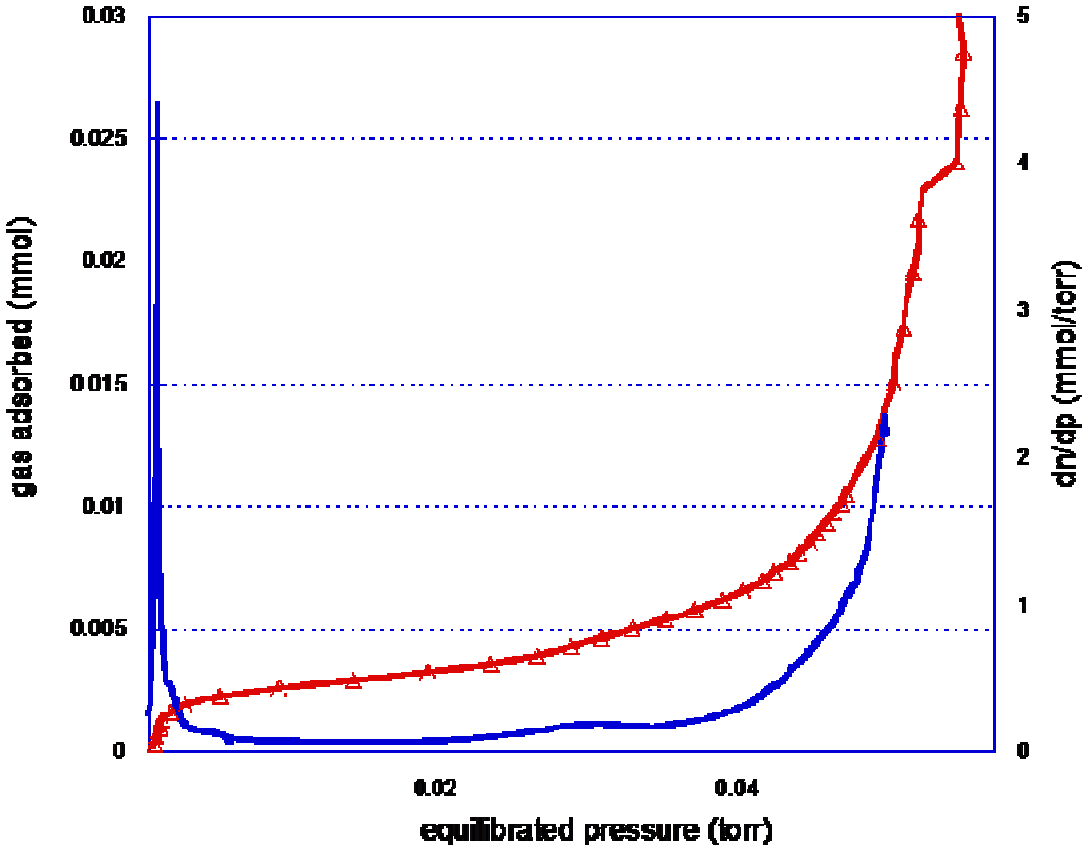

Figure 12. Representative Decane Isotherm.

*Decane isotherm at 258.33K (*red*) plotted next to its numerical derivative (*blue*).*

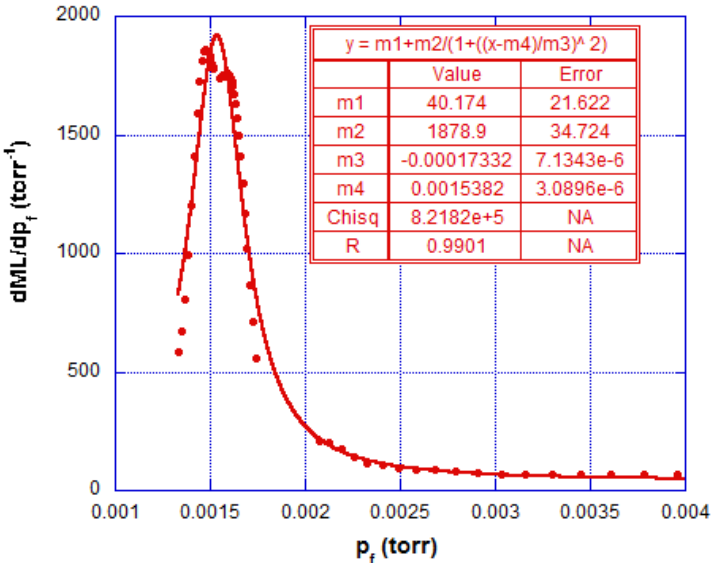

(a)

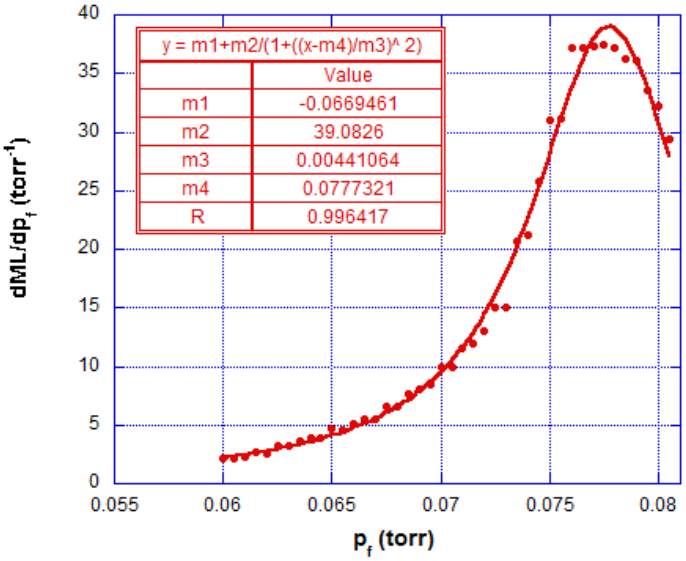

(b)

Figure 13. Isotherm Derivatives Fitted to Lorentzian Distributions.

(a) First layer of decane isotherm shown in Figure 12.

(b) Second layer of nonane isotherm shown in Figure 11

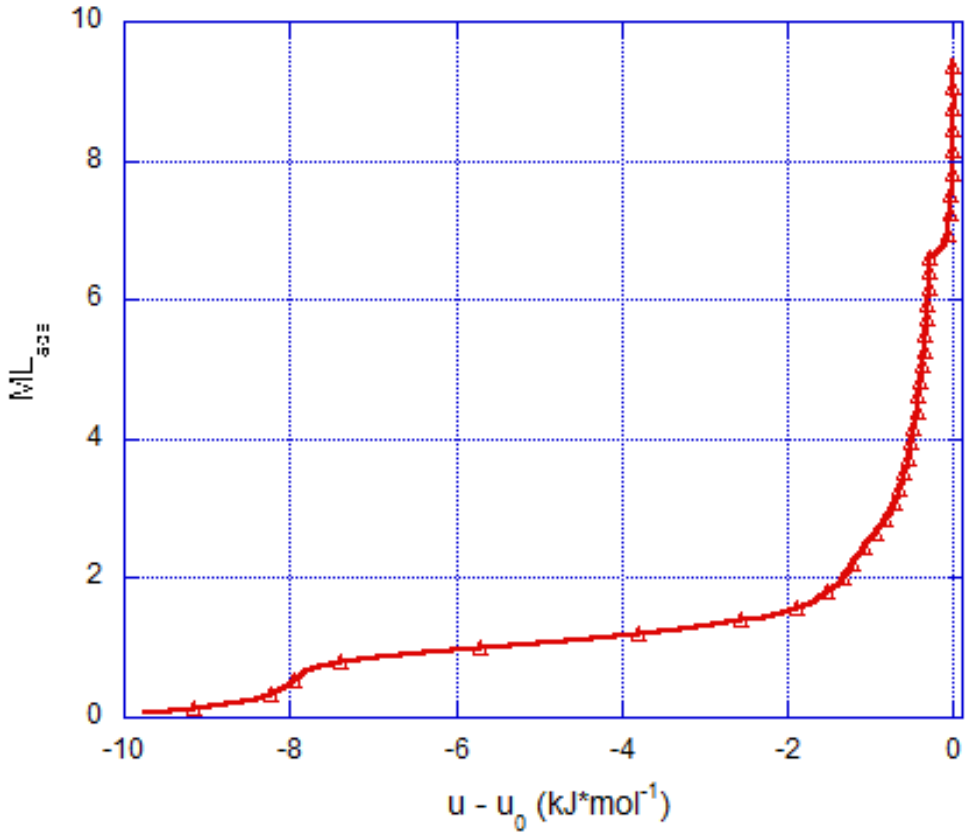

Figure 14. Nonane Isotherm Plotted Against μ - μ0.

This is the same isotherm from Figure 11. *Note the difference in the abrupt break toward SVP. The ordinate axis is given in units of adsorbed monolayers.*

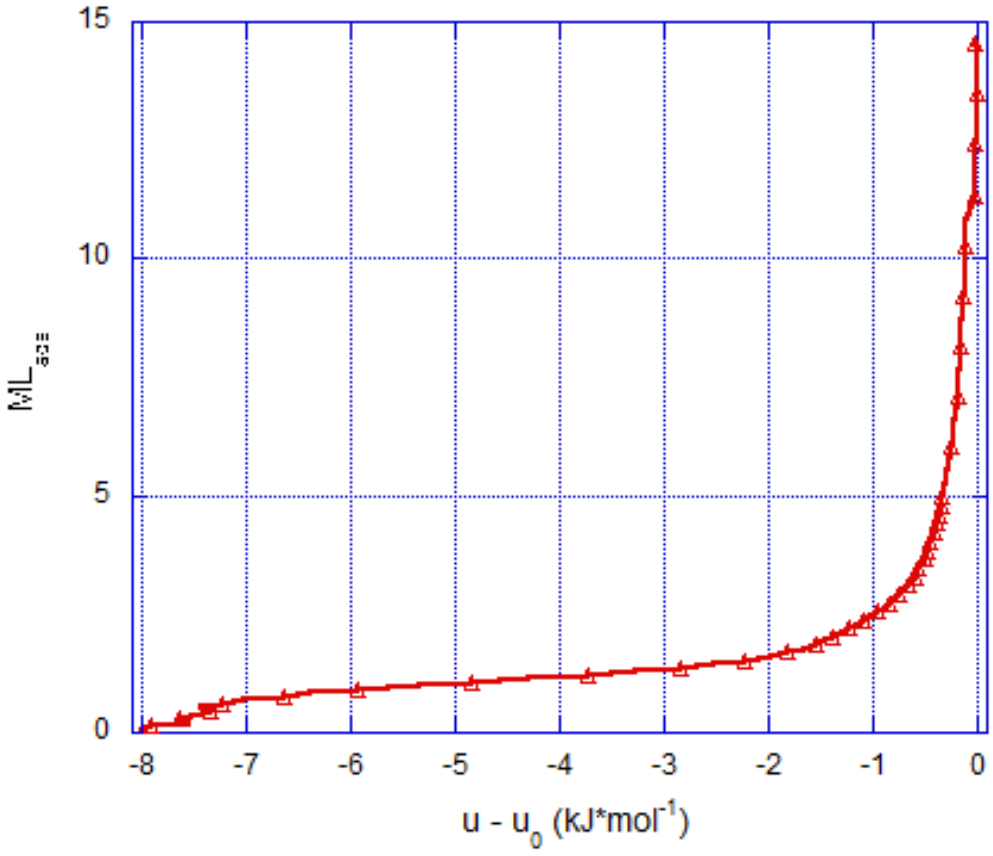

Figure 15. Decane Isotherm Plotted Against μ - μ0.

This is the same isotherm from Figure 12. *Again, note the difference in the discontinuity at high coverage.*

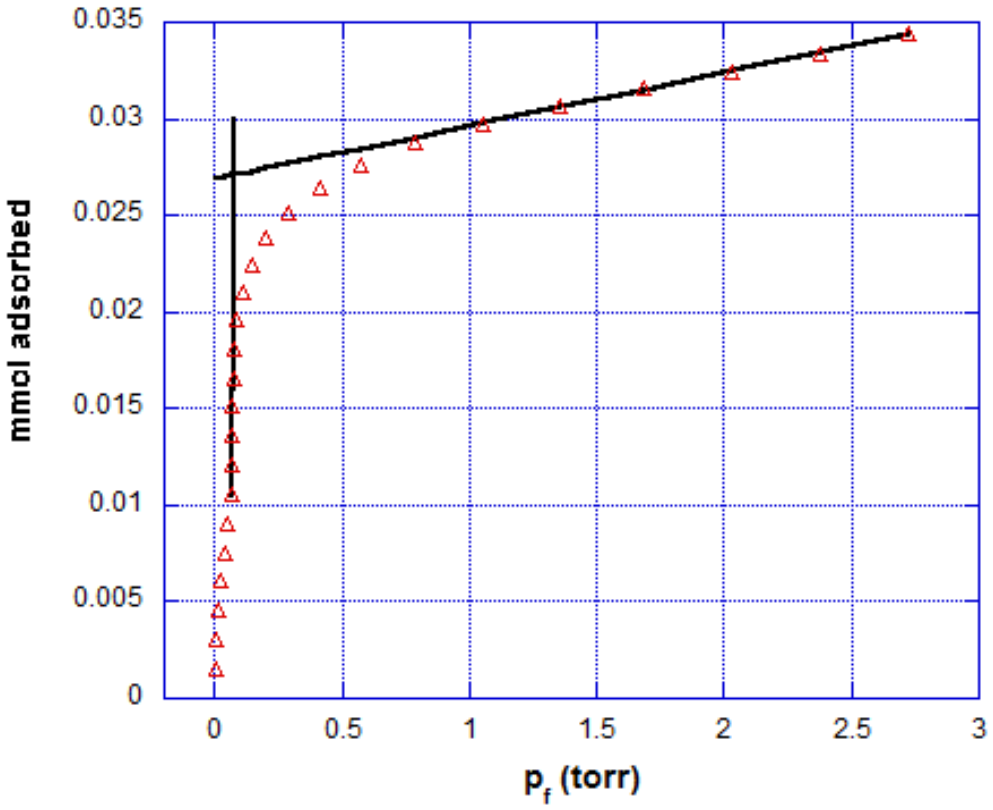

Figure 16. Point B Method Illustration.

Here the Point B method is applied to a methane isotherm. Linear regressions (black) are applied to the vertical and horizontal portions of the first step. The monolayer capacity is the ordinate value of the intersection of the two fits (≈0.027 mmol).

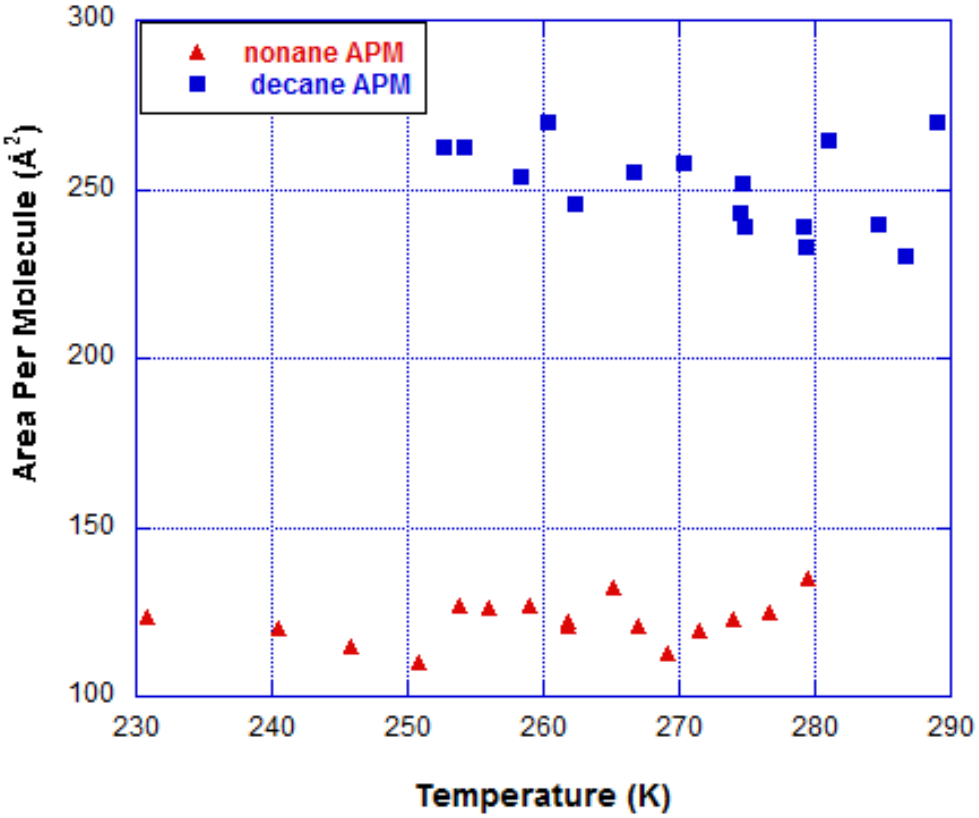

Figure 17. Variation of APM with Temperature.

The lack of correlation between APM and temperature argues against the presence of a low- to high-density phase transition for either molecule.

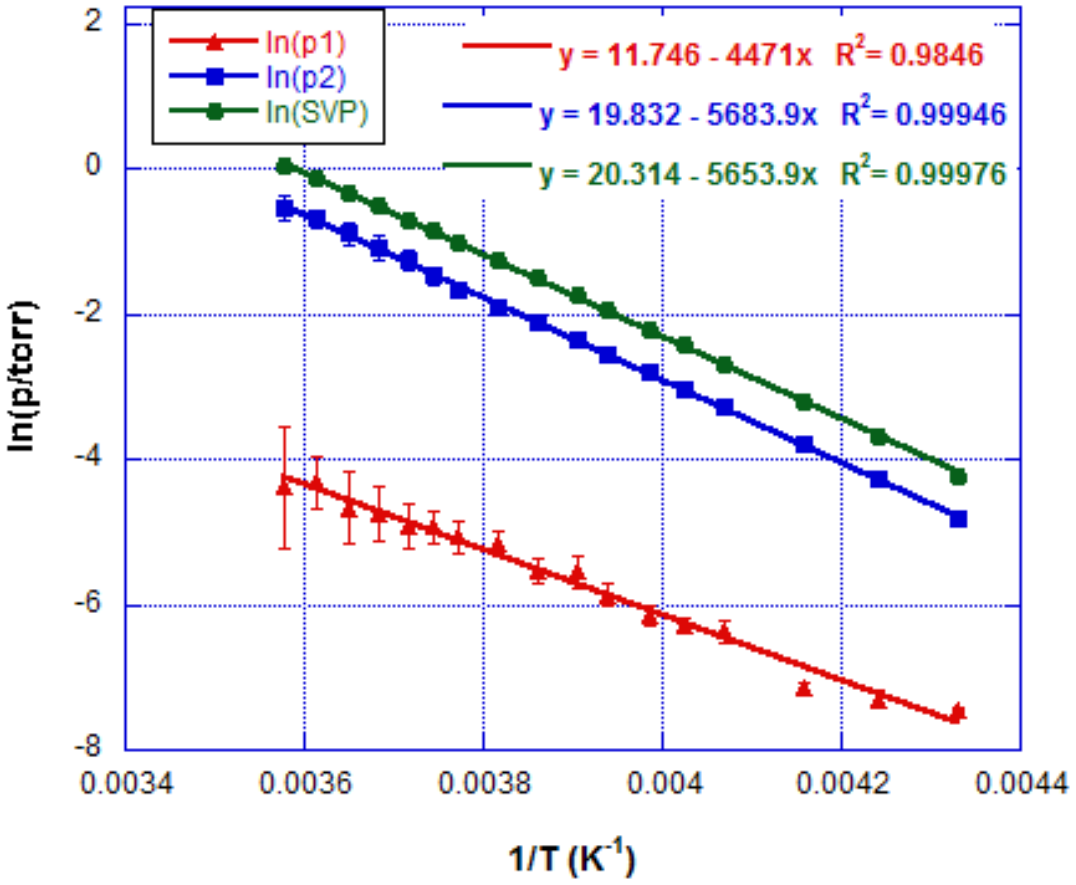

Figure 18. Nonane Clausius-Clapeyron Analysis.

*The pressures of the first and second layers (*p1 *&* p2*) are taken to be the centers of the Lorentzian fits of the derivative of each isotherm (see previous figure). The SVP of each isotherm corresponds to the bulk phase. In order to extract* $A^{(n)}$ *and* $B^{(n)}$*, the natural logarithm of these pressures is plotted against inverse temperature.*

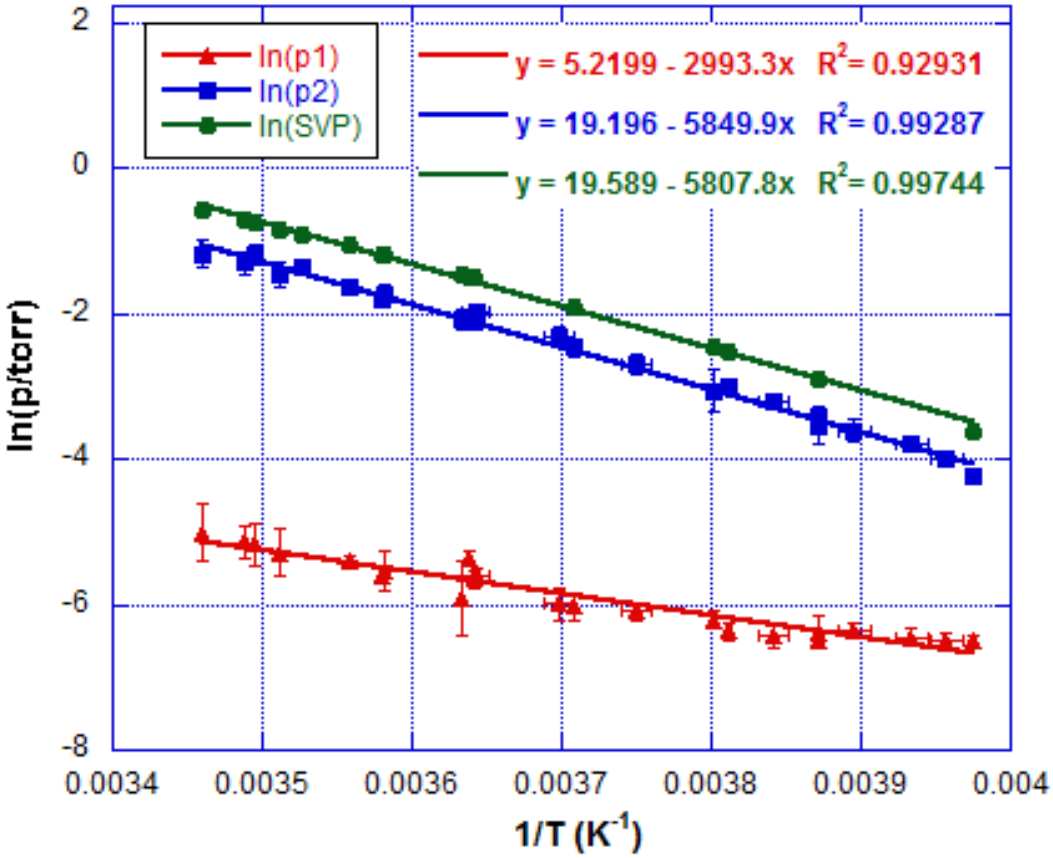

Figure 19. Decane Clausius-Clapeyron Analysis.

See comments for Figure 18.

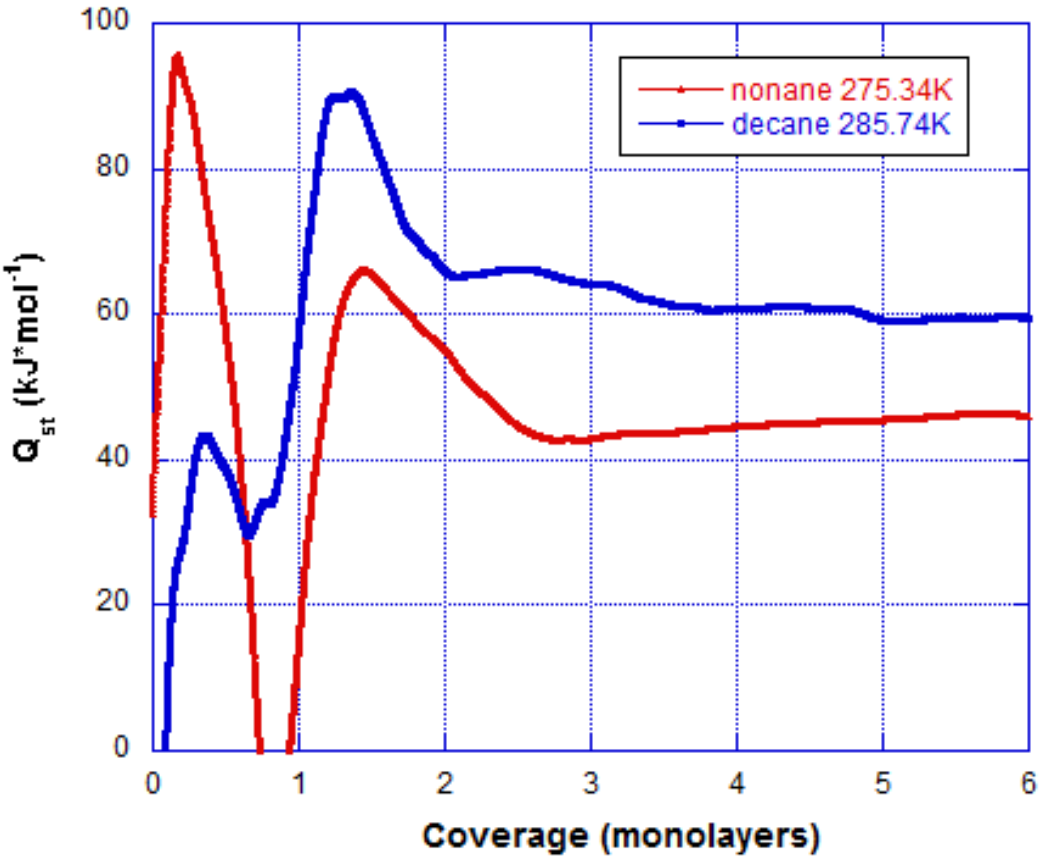

Figure 20. Q_{st} for Nonane & Decane.

These plots show maxima at the initial formation of the first and second layers. At high coverages, Q_{st} approaches the bulk ΔH_{vap} for both systems.

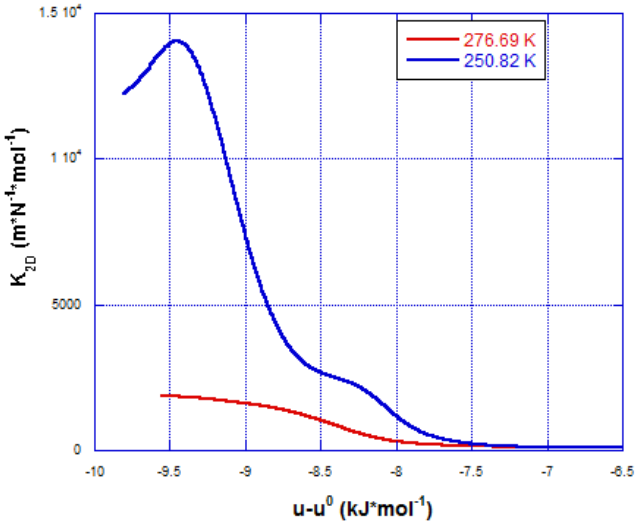

(a)

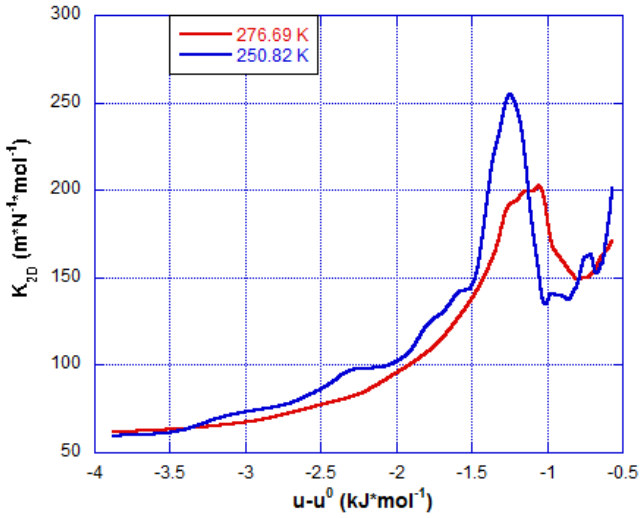

(b)

Figure 21. K_{2D} Peaks for Nonane.

(a) 1st layer.

(b) 2nd layer.

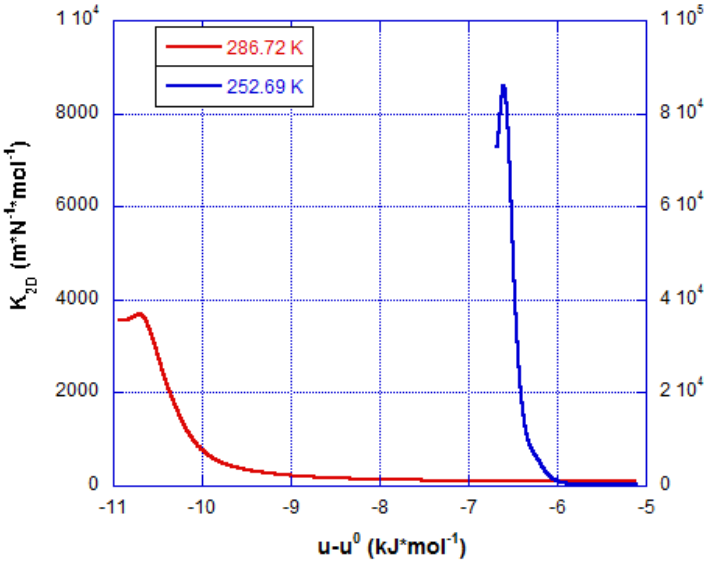

(a)

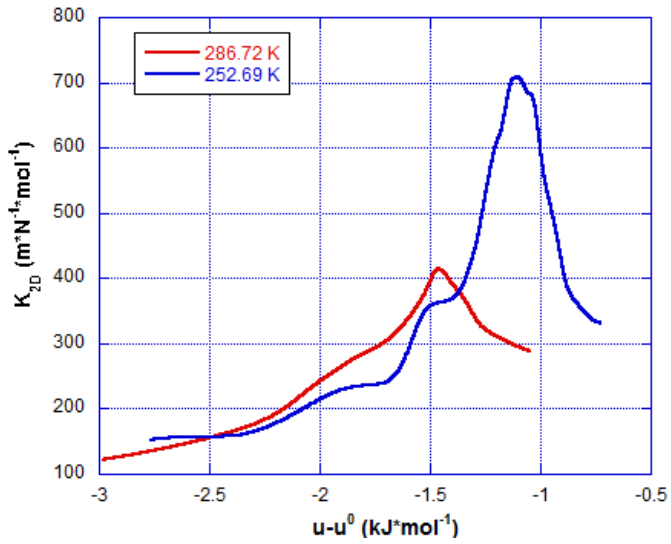

(b)

Figure 22. K_{2D} Peaks for Decane.

(a) 1st layer.

(b) 2nd layer.

See note for Figure 21*. Also note that in (a), the ordinate axis is scaled up by a factor of 10 for the lower temperature isotherm.*

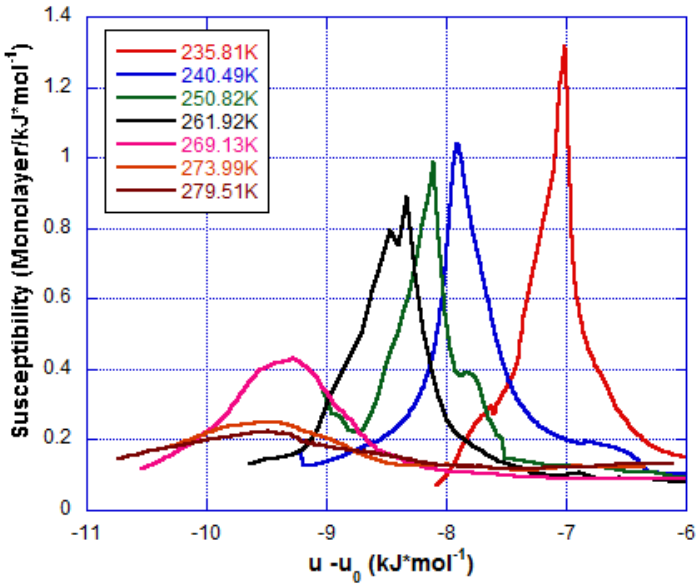

(a)

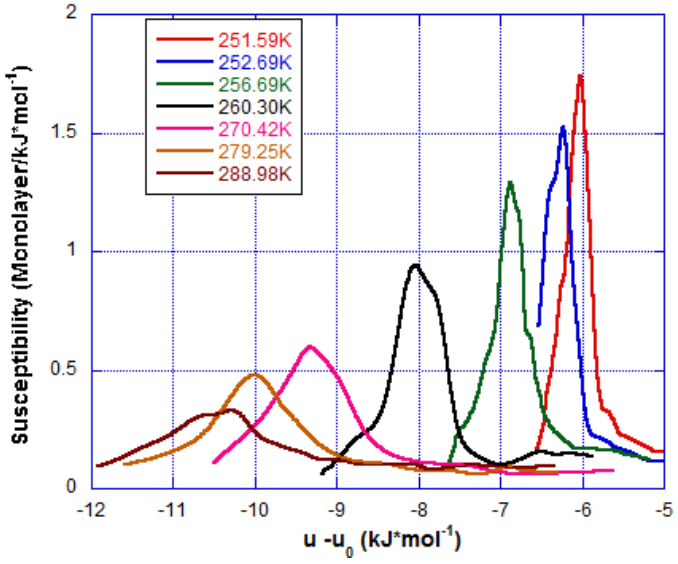

(b)

Figure 23. Select First Layer Suscepibilities.

(a) Nonane.

(b) Decane.

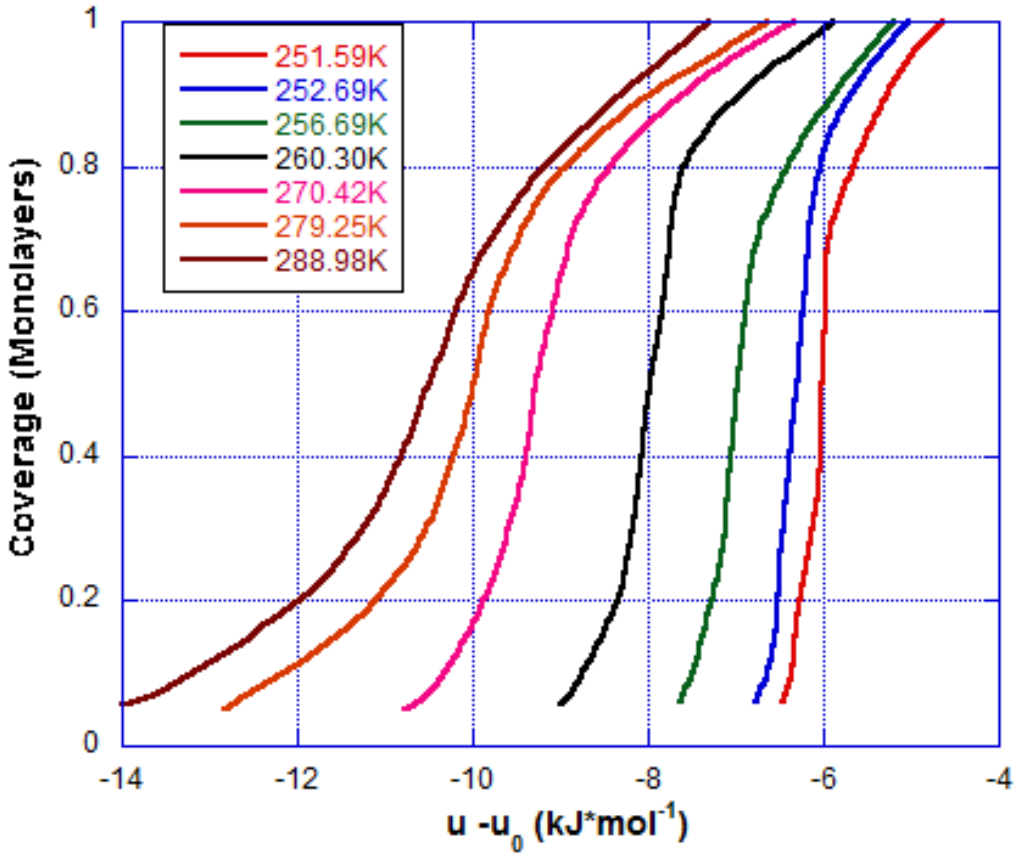

Figure 24. Decane 1st Monolayer.

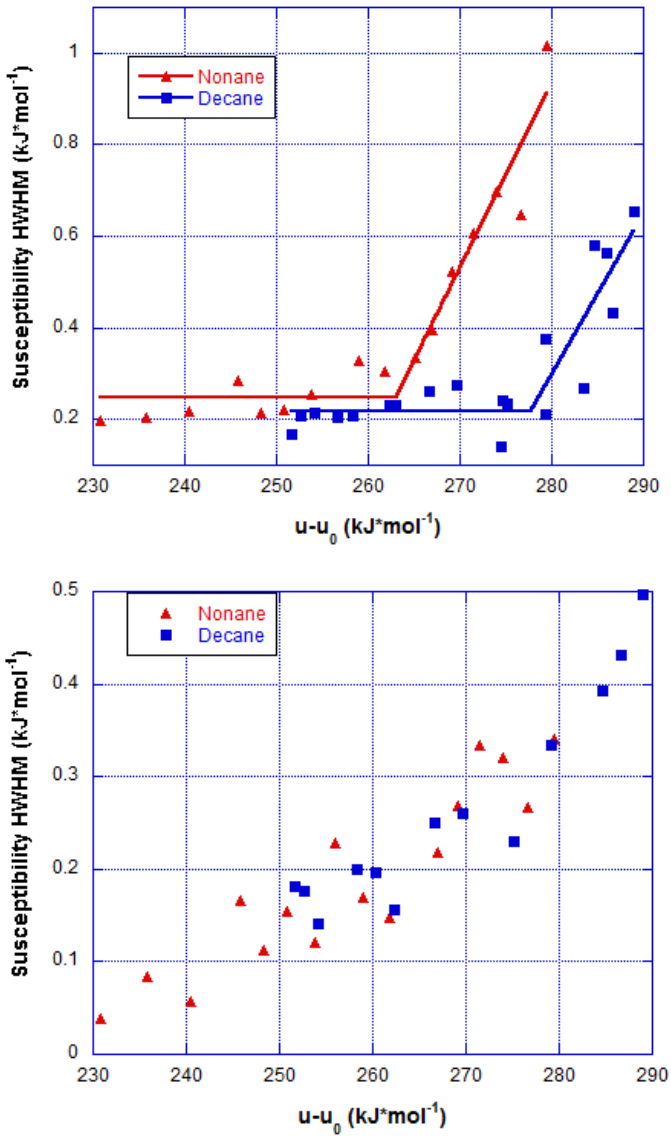

Figure 25. HWHM of Susceptibility Peaks.

Top: *First Layer: Transition occurs at 263.04 ± 1.36 K for nonane and 277.77 ± 1.72 K for decane*

Bottom: *Second Layer: No transition occurs for either adsorbate over the temperature ranges studied.*

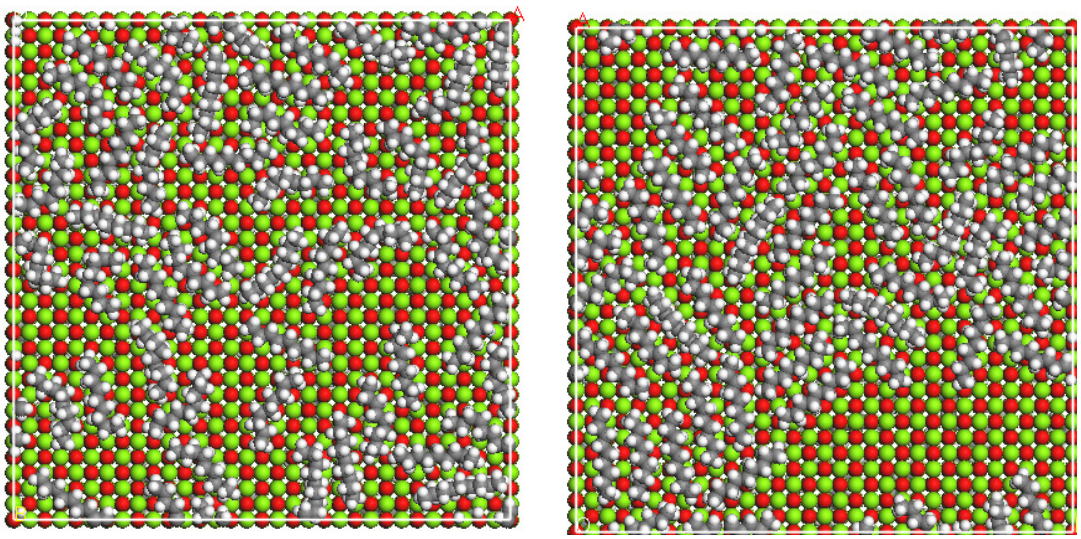

350K 250K

Nonane

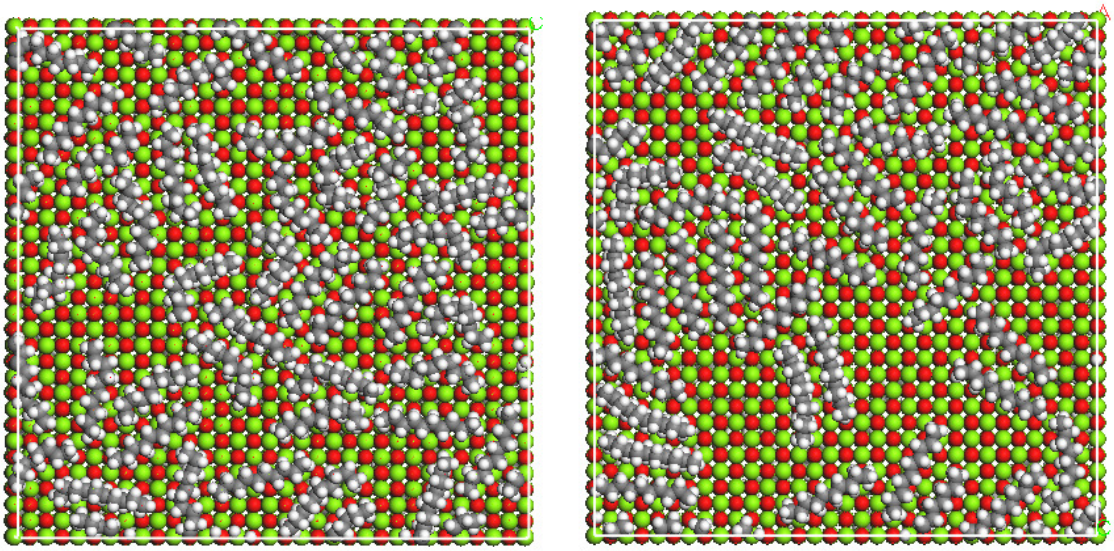

350K 260K

Decane

Figure 26. Depiction of 2D Supercritical and Liquid Phases.

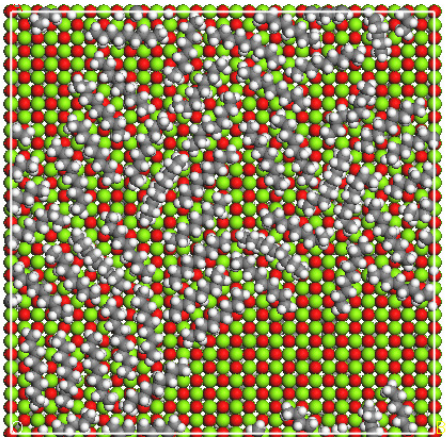

initial

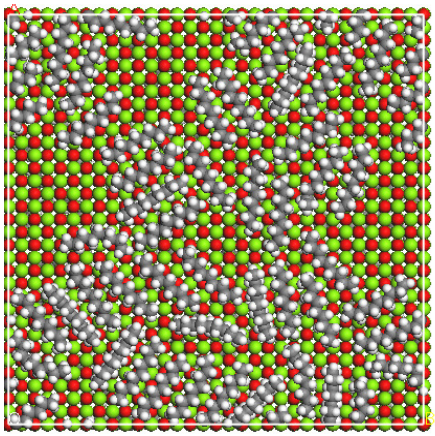

final

Nonane – 250K

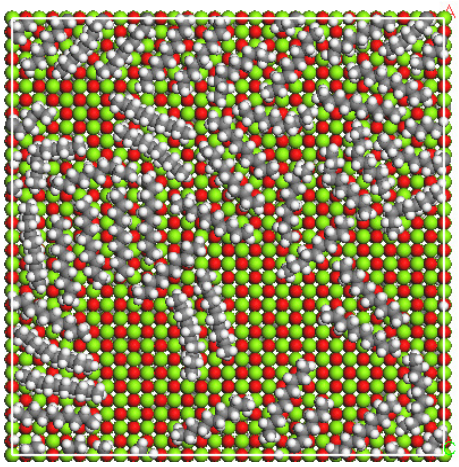

initial

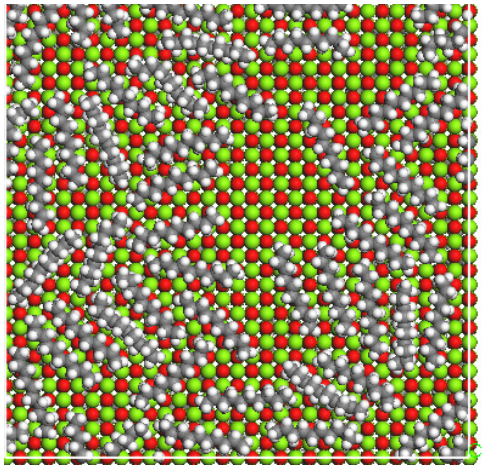

final

Decane – 260 K

Figure 27. 2D Liquid Phases.

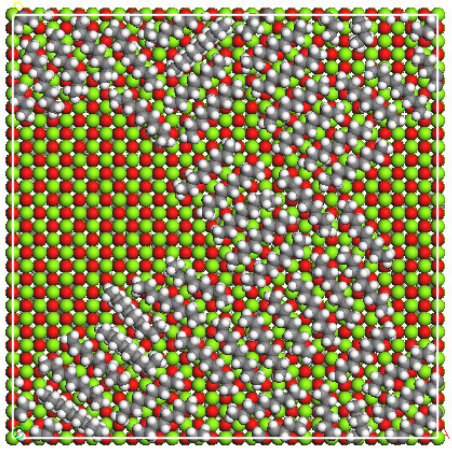

initial

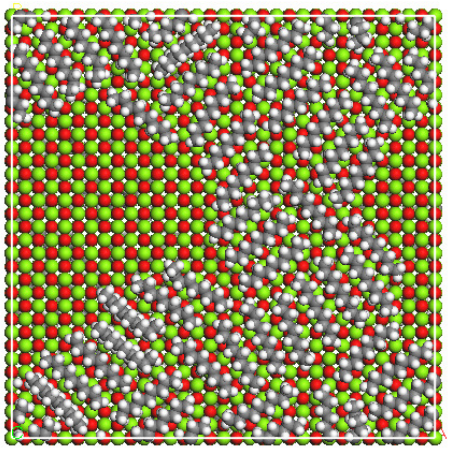

final

Nonane – 100K

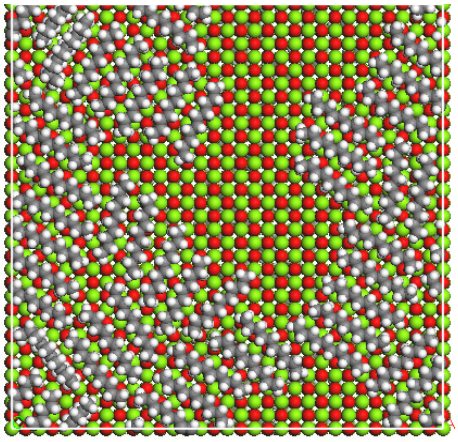

initial

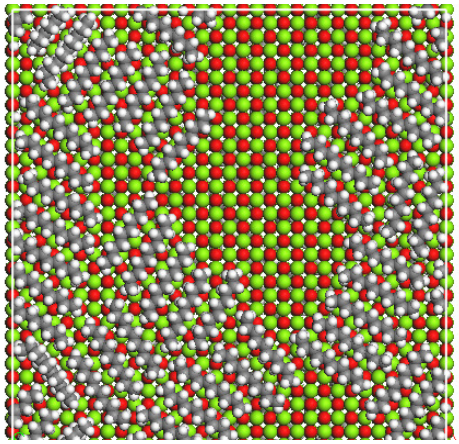

final

Decane – 100K

Figure 28. 2D Solid Phases.

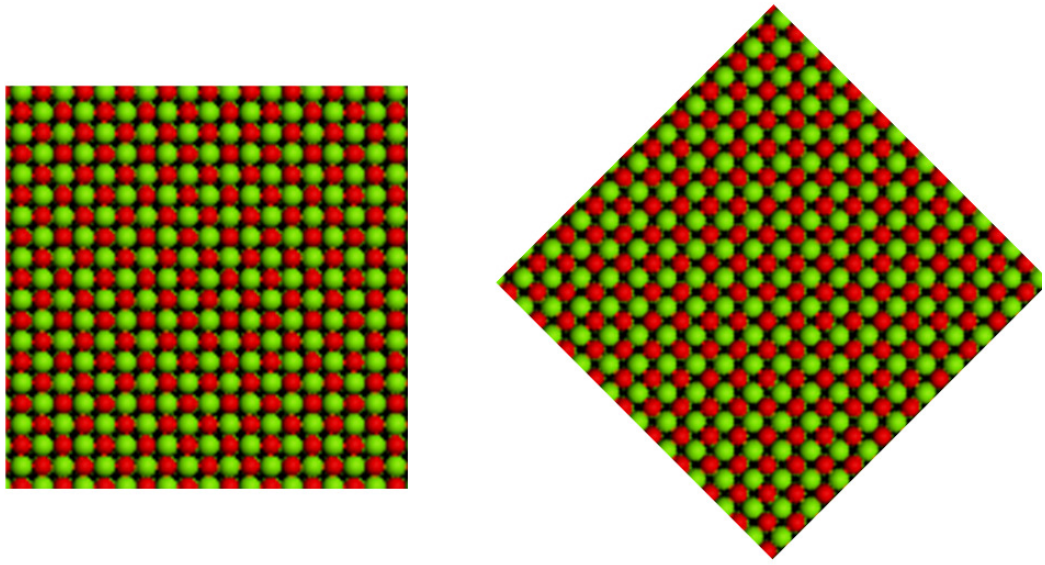

Figure 29. Two Top Views of MgO(100) Slab.

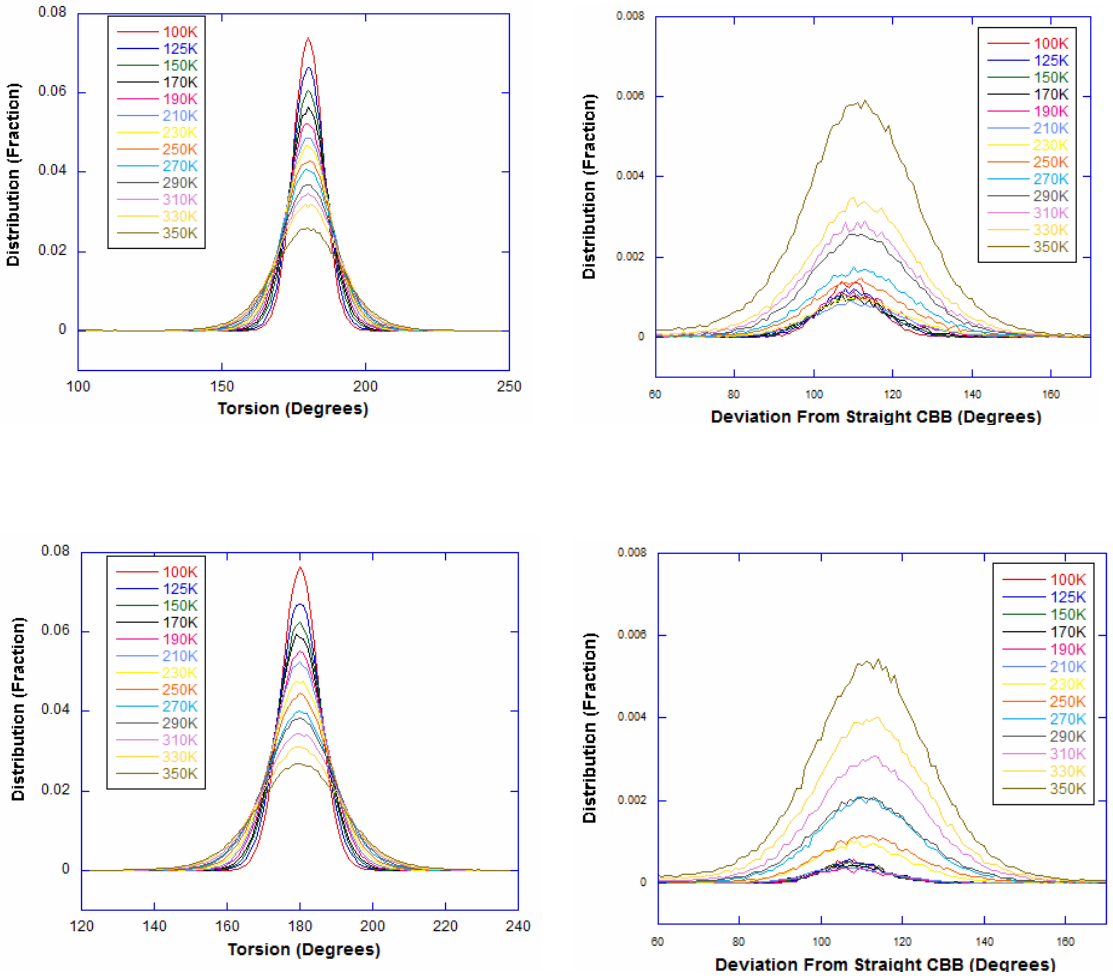

Figure 30. Distribution Around Torsional Minima.

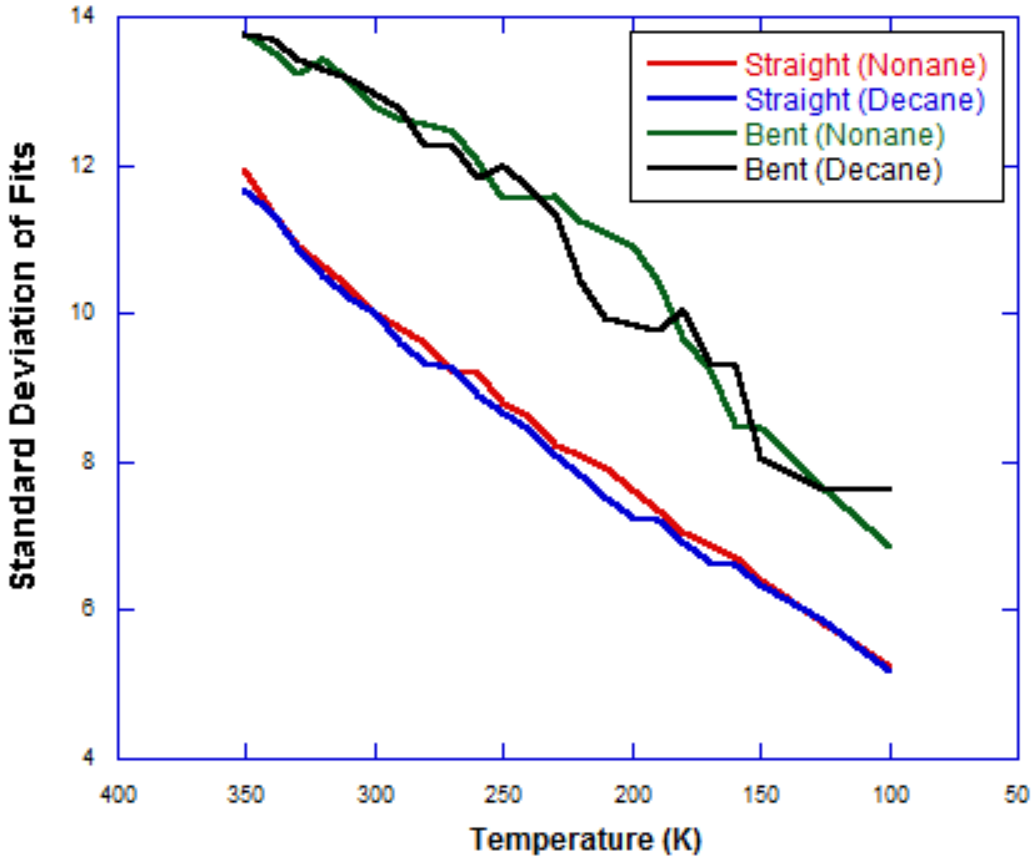

Figure 31. Standard Deviation of Torsion Gaussians.

Straight: *Centered around 180° minimum.*

Bent: *Centered about minimum 110° away.*

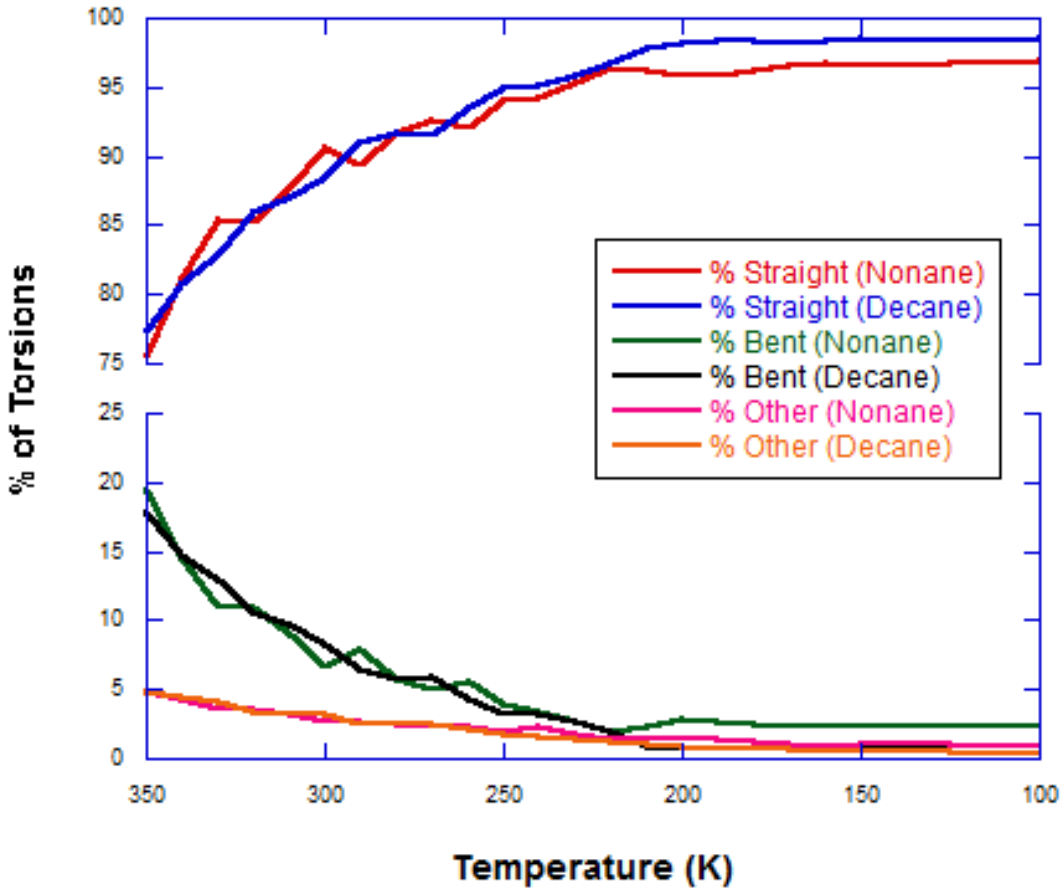

Figure 32. Temperature Dependence of Torsion Configuration.

Straight: *Centered around 180° minimum.*

Bent: *Centered about minimum 110° away.*

Other: *Remaining torsions.*

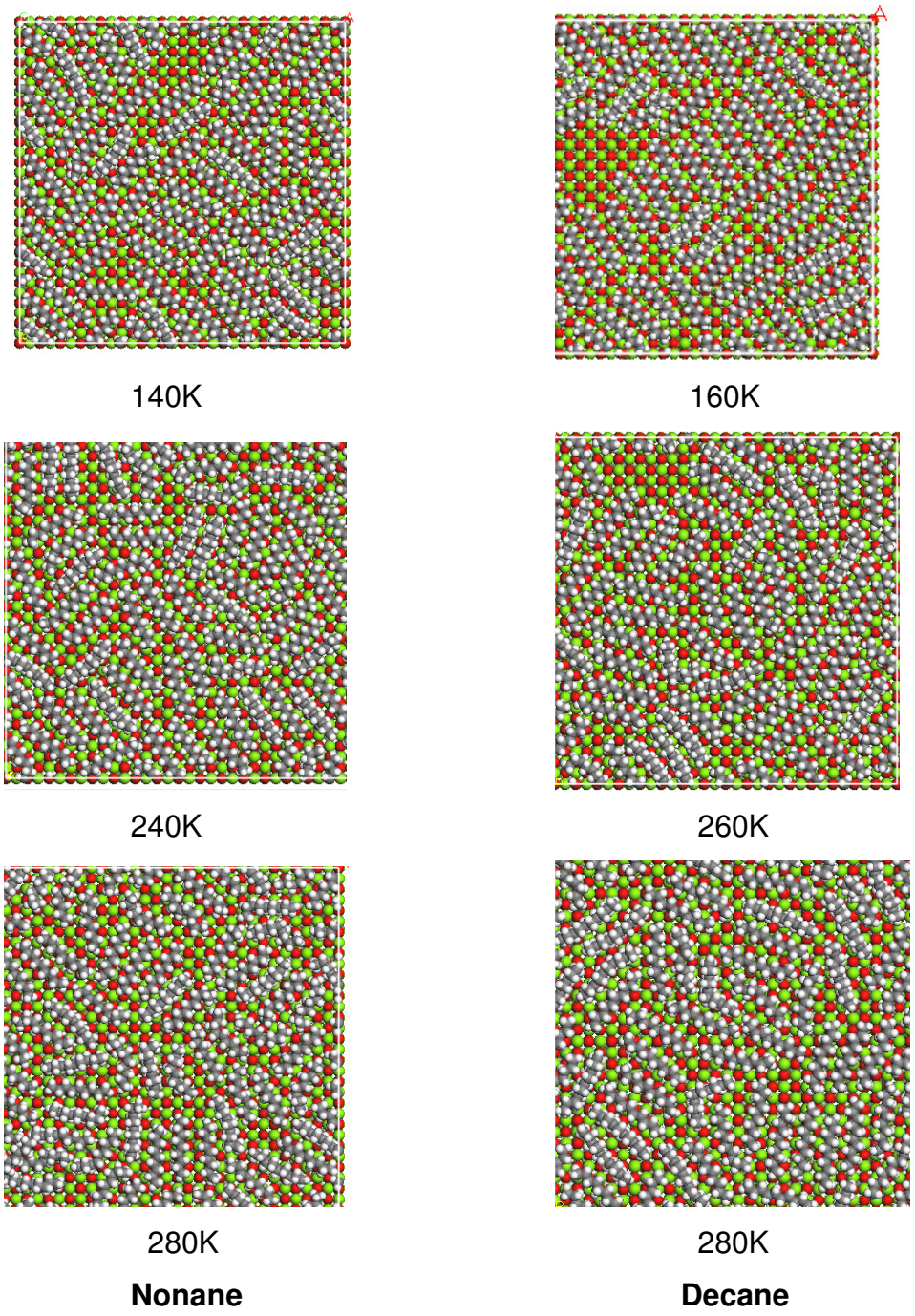

Figure 33. Temperature Dependence of First Monolayer Structure.

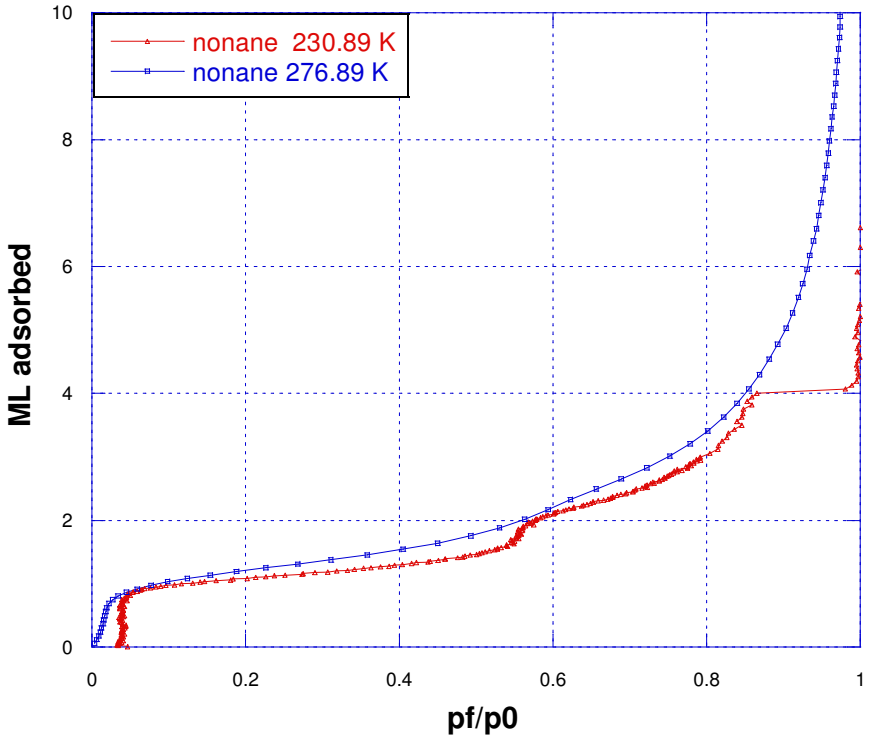

Figure 34. High and Low Temperature Nonane Isothems.

Second step is prominent in the low temperature nonane isotherm, but barely visible in at high temperature.

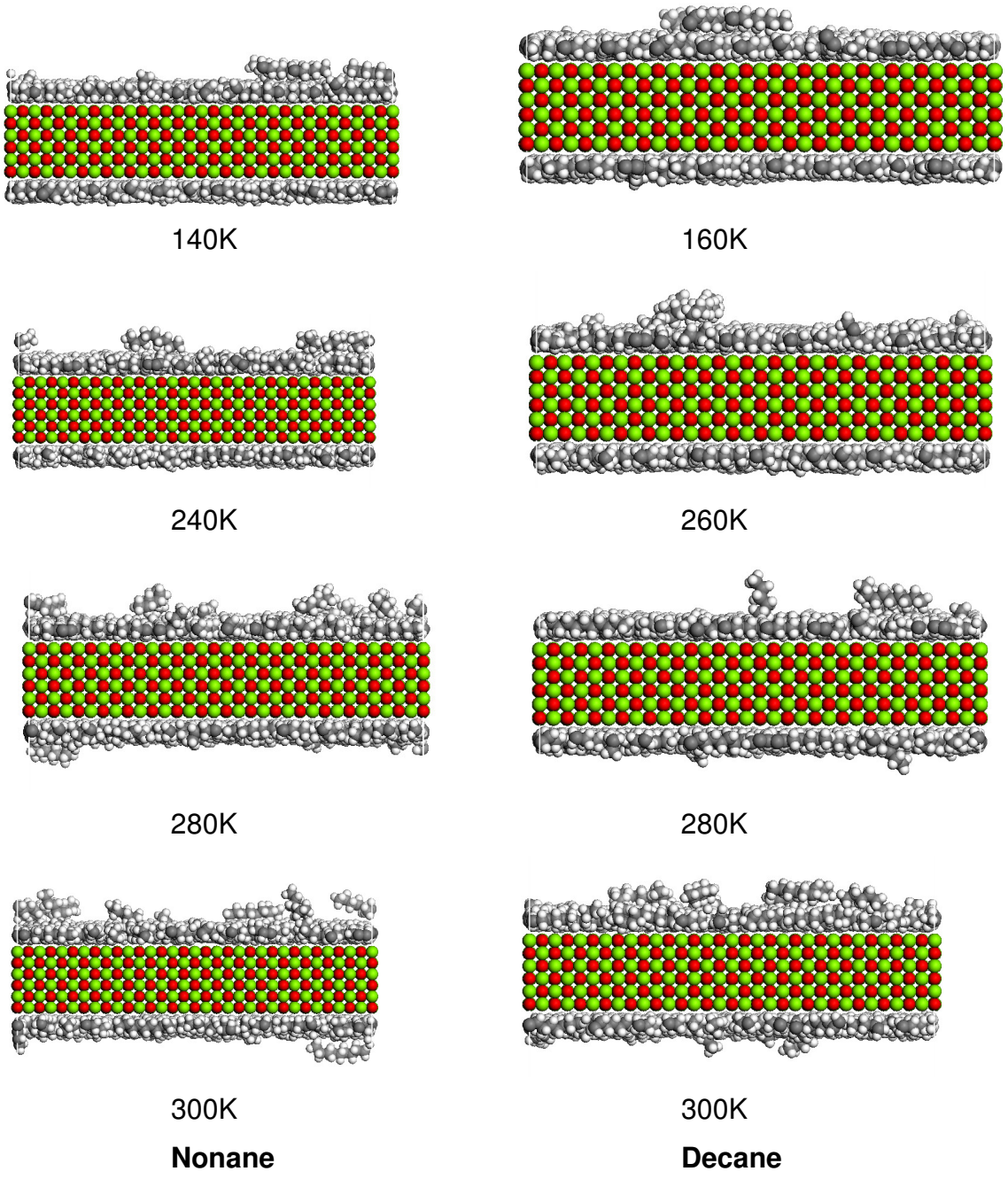

Figure 35. First ML at Varying Temperatures (Side)

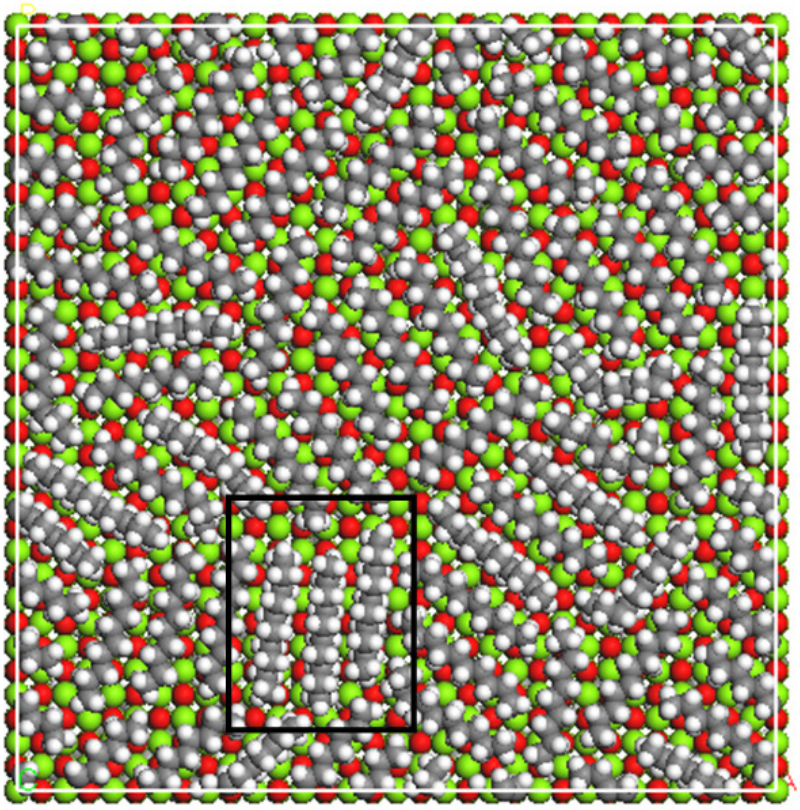

Figure 36. Decane at 160K, Second Layer Molecules Removed.

First layer molecules directly underneath outlined in black

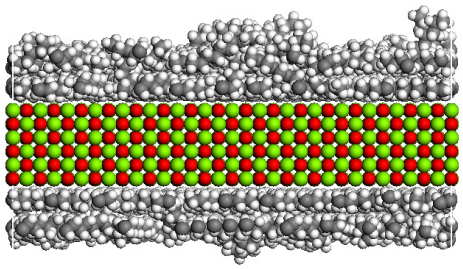

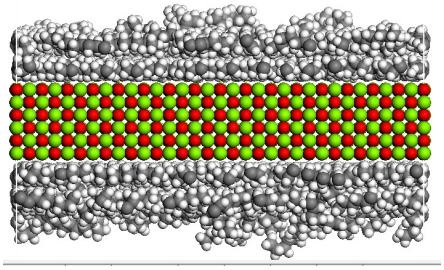

240K

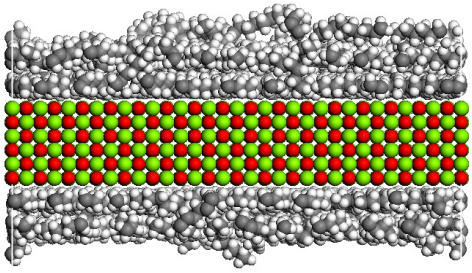

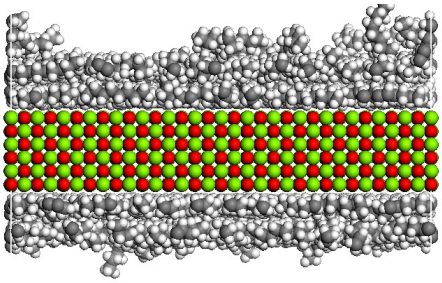

270K

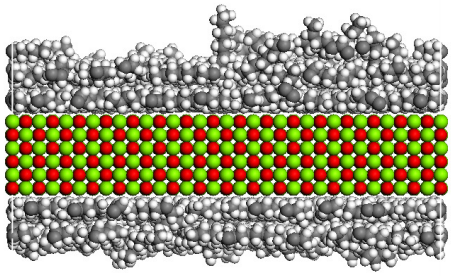

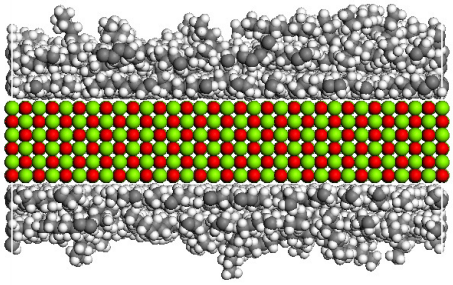

300K

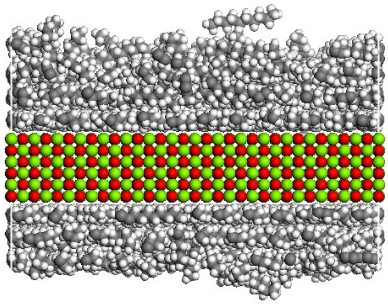

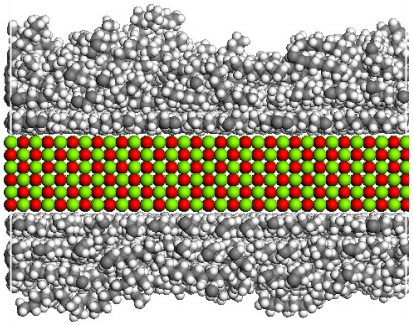

300K

Decane **Nonane**

Figure 37. Multilayer Coverages.

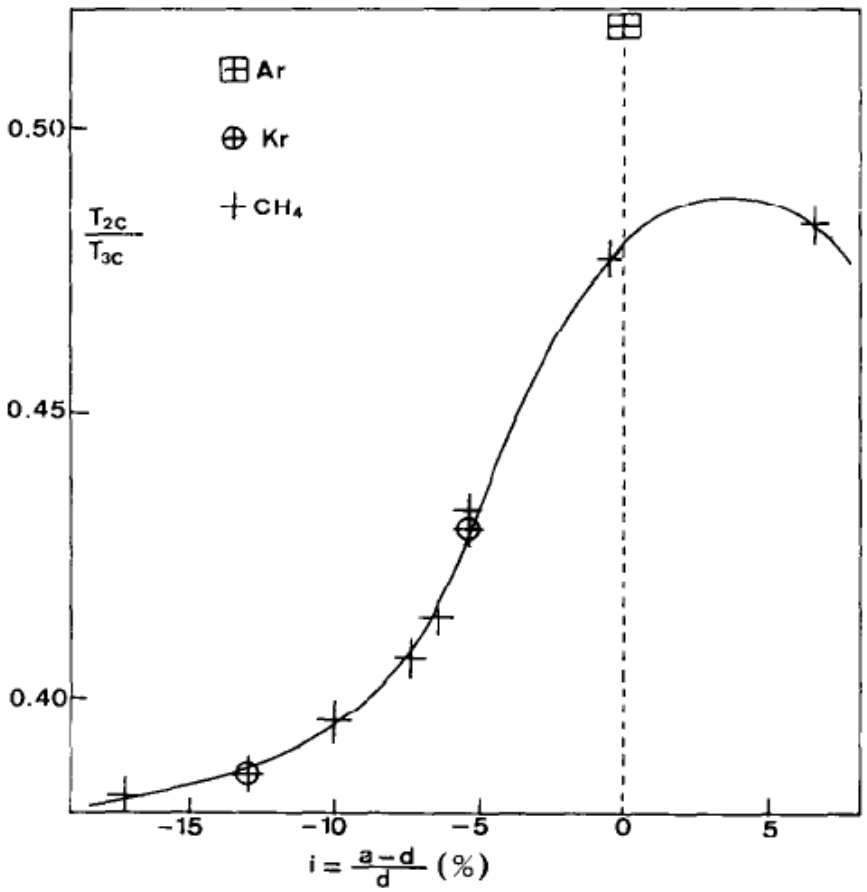

Figure 38. T_{2C}/T_{3C} Versus Incompatibility Factor.

From Reference [20].

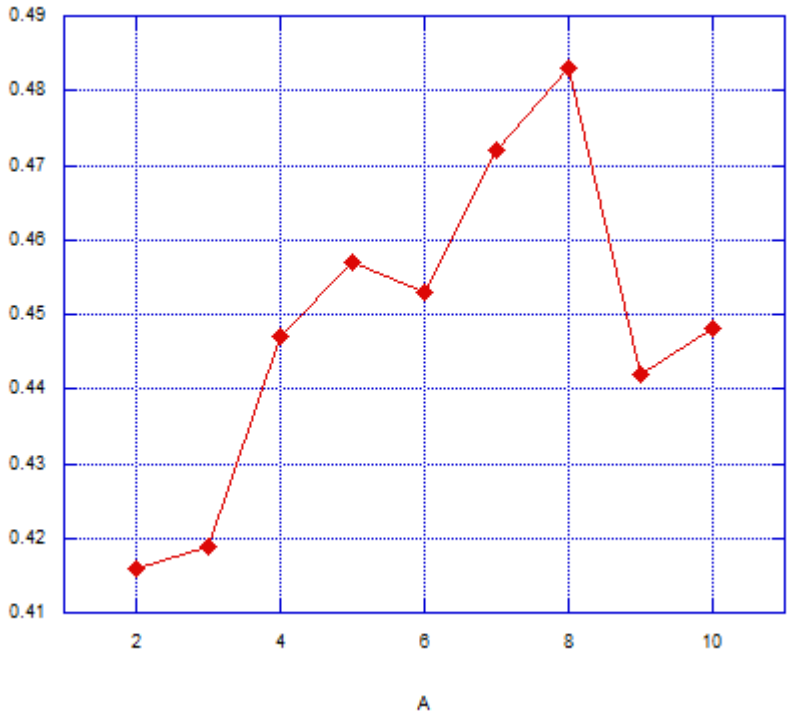

Figure 39. T_{2C}/T_{3C} Trend.

Compiled from data in [32,34]

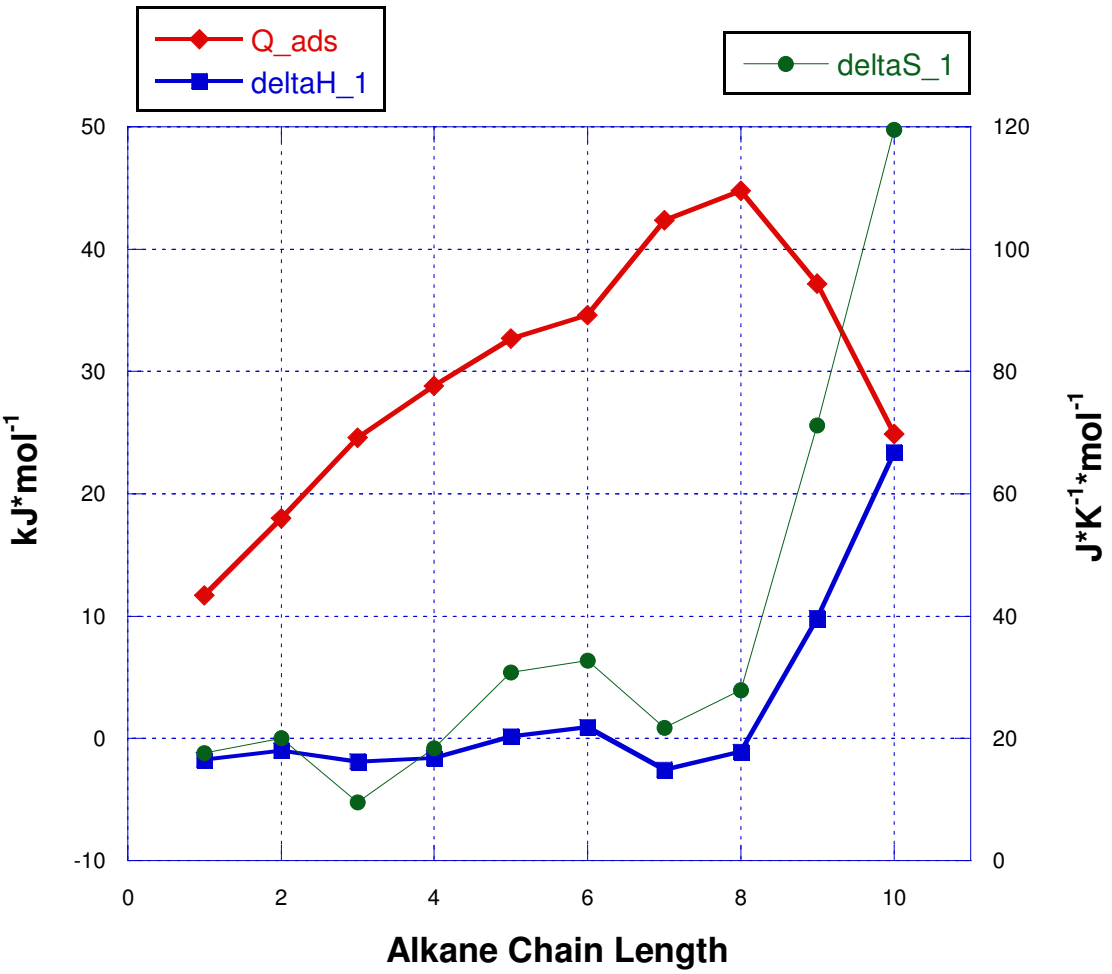

Figure 40. First Layer Thermodynamic Trends.

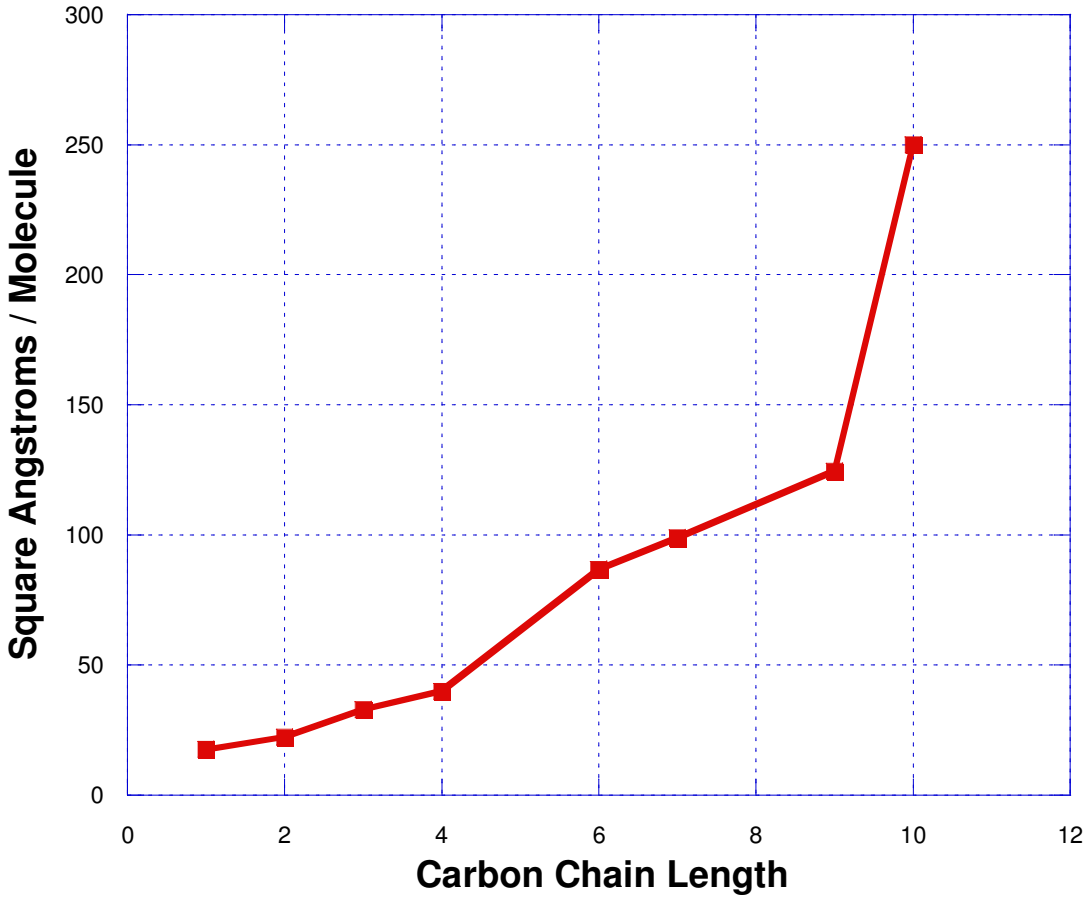

Figure 41. Area Per Molecule Trend.

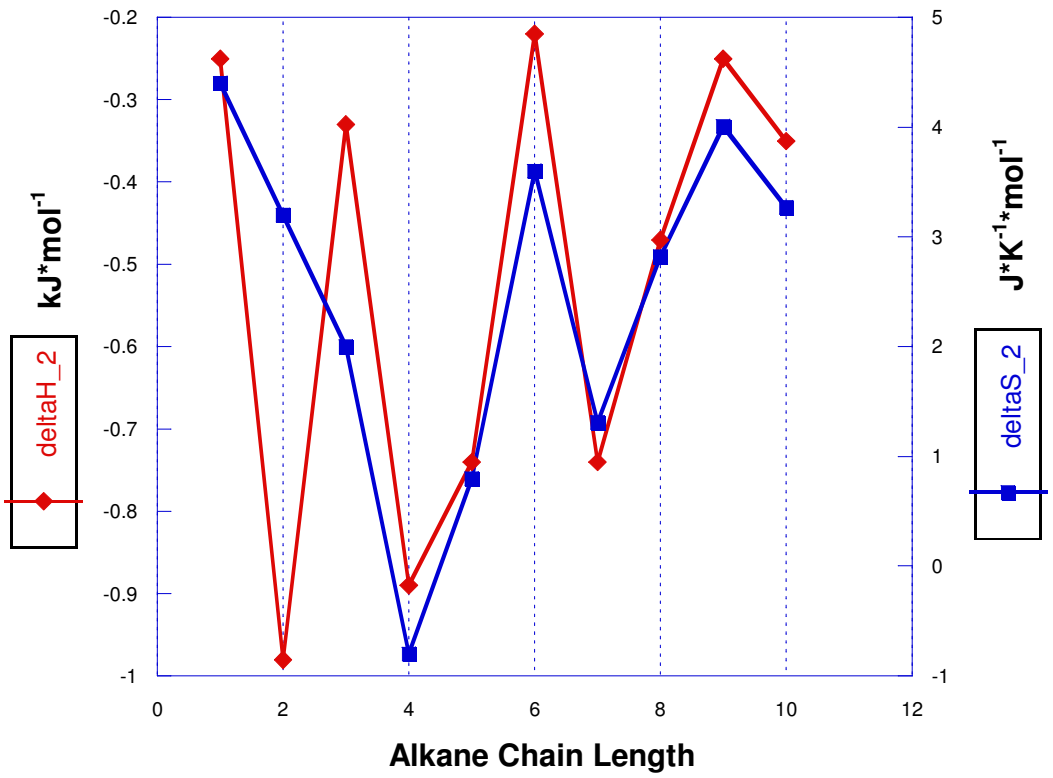

Figure 42. Second Layer Thermodynamic Trends.

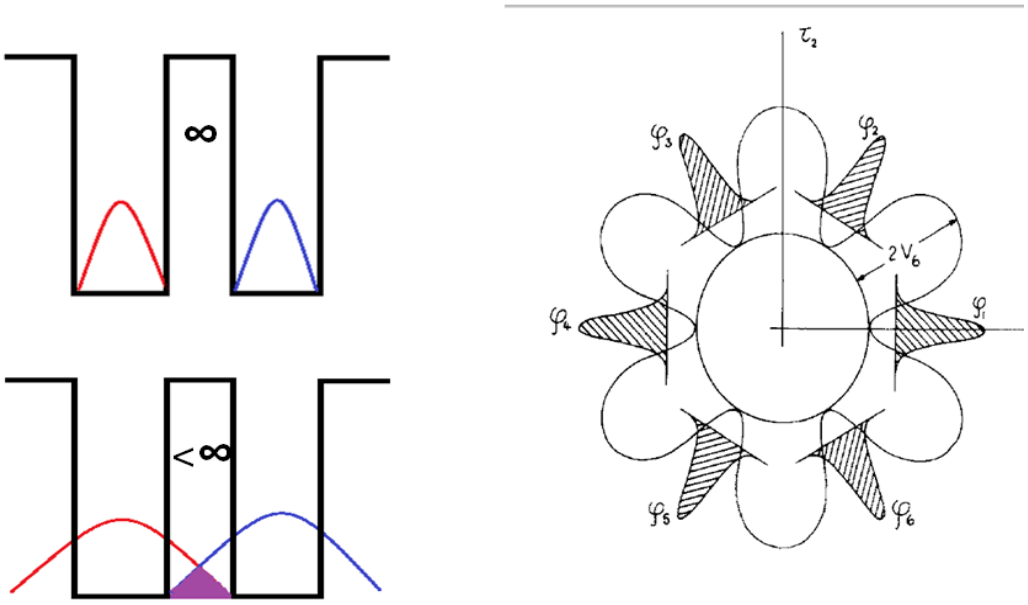

Figure 43. Translational Double Square Well and Six-Fold Rotational Potentials.

Right hand figure from Reference [64]

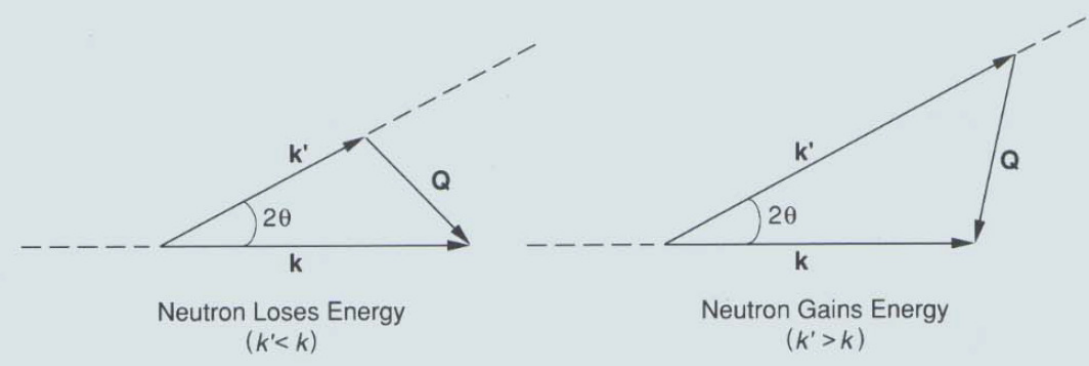

Figure 44. Scattering Triangle for Inelastic Neutron Scattering.

From Reference [56]

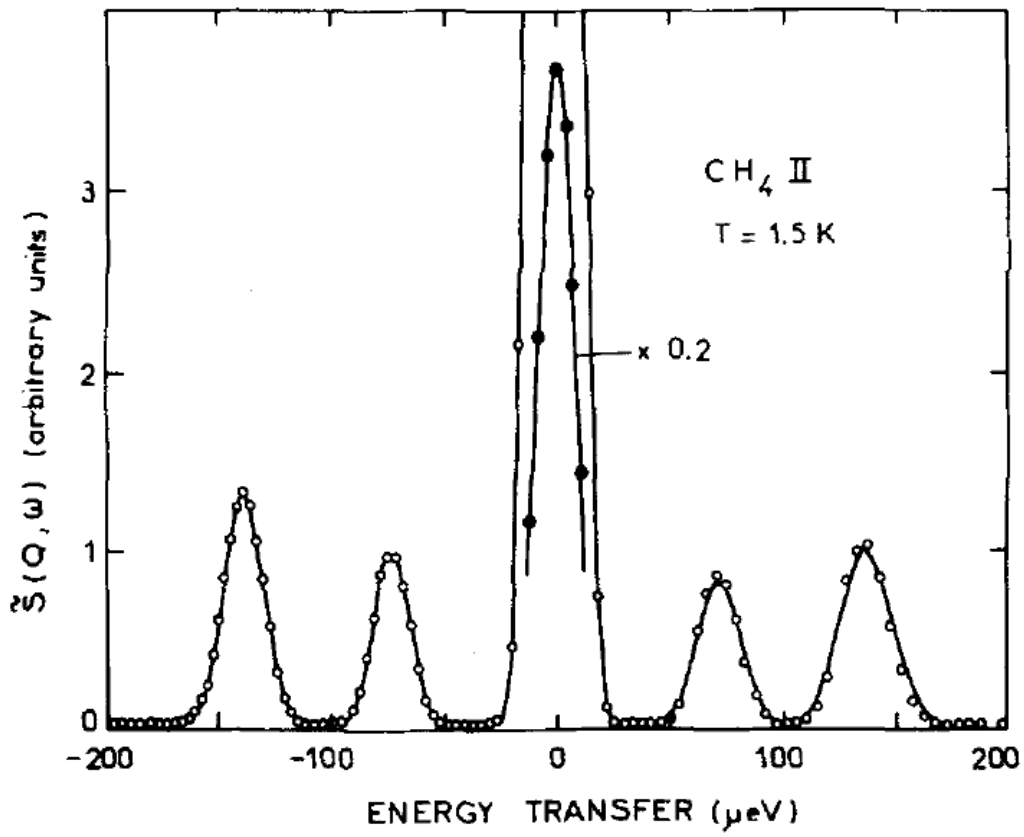

Figure 45. Rotational Tunneling Spectrum of Phase II CH_4.

From Reference [61]

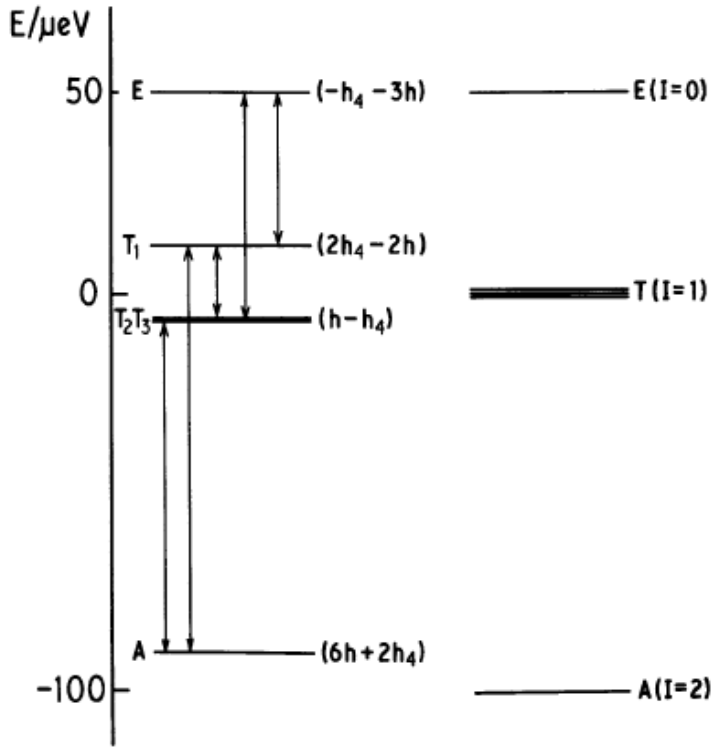

Figure 46. Splitting of T Sublevels (CH_4/Graphite).

From [67]

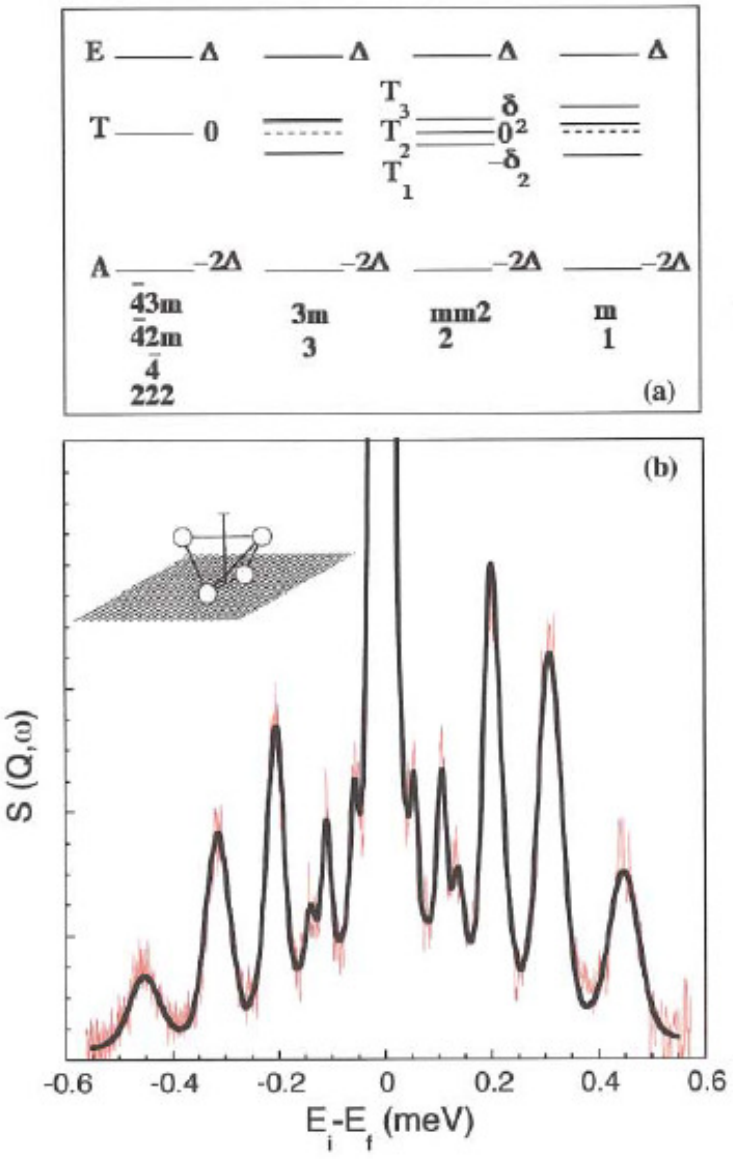

Figure 47. INS Results for CH_4/MgO.

From Reference [30]

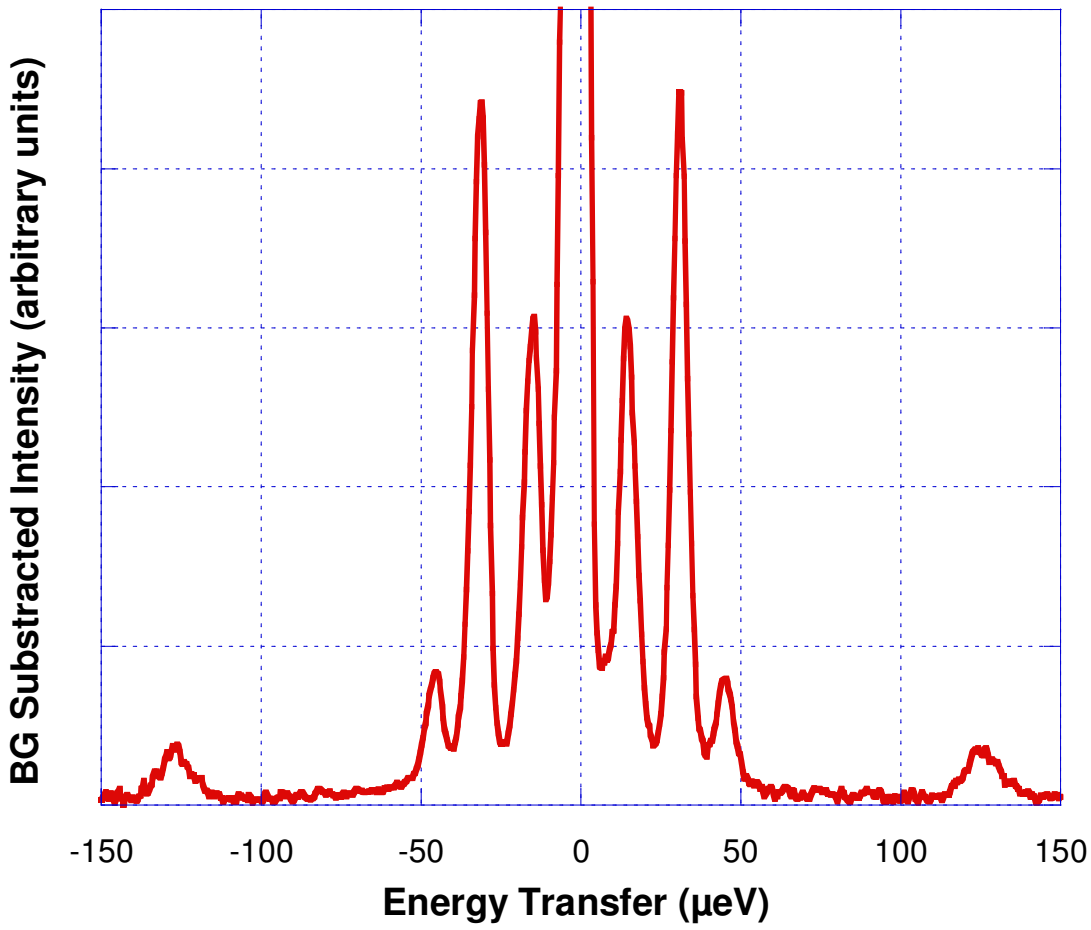

Figure 48. INS Spectrum of CH_2D_2/MgO Monolayer.

Background Subtracted.

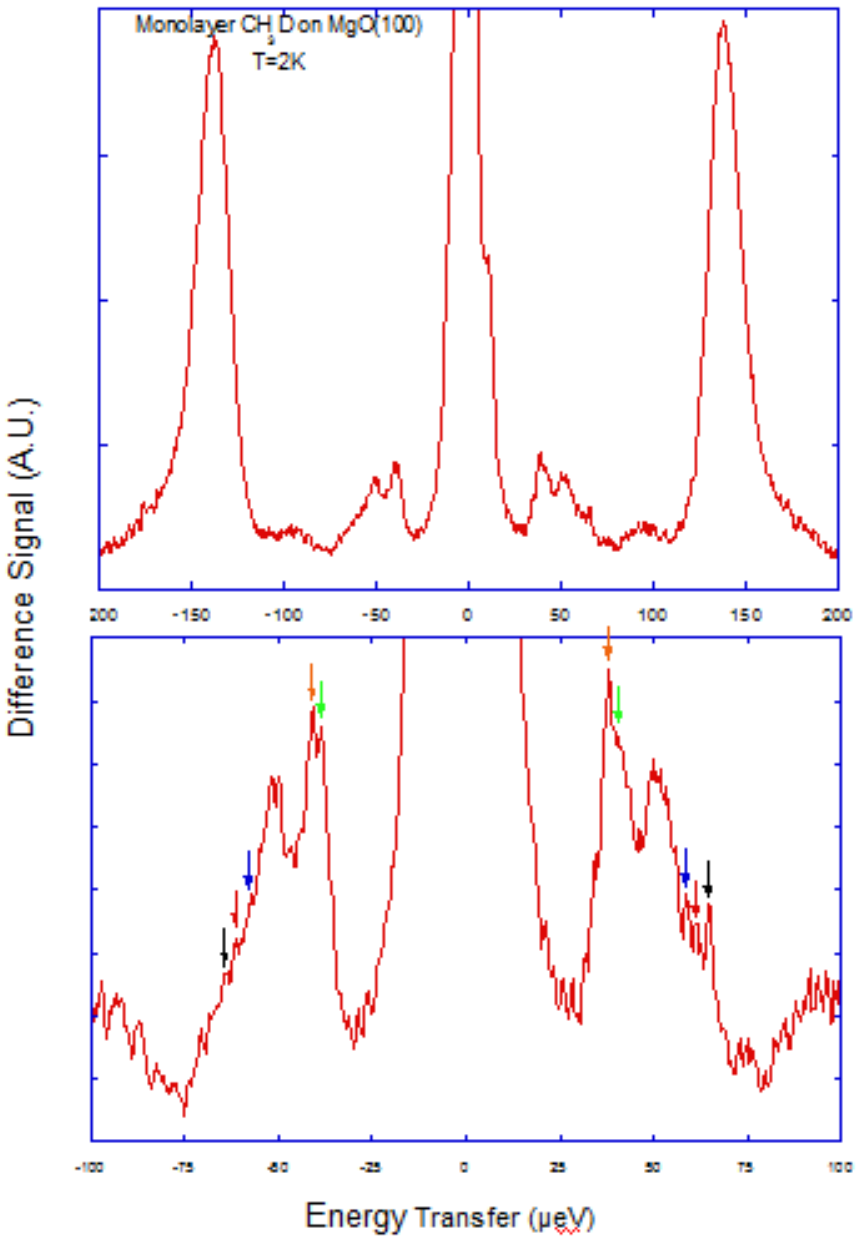

Figure 49. INS spectrum of CH_3D.MgO Monolayer.

Full INS spectrum of CH_3D */MgO (top) and close-up of fine structure of peaks closest to elastic line (bottom).*

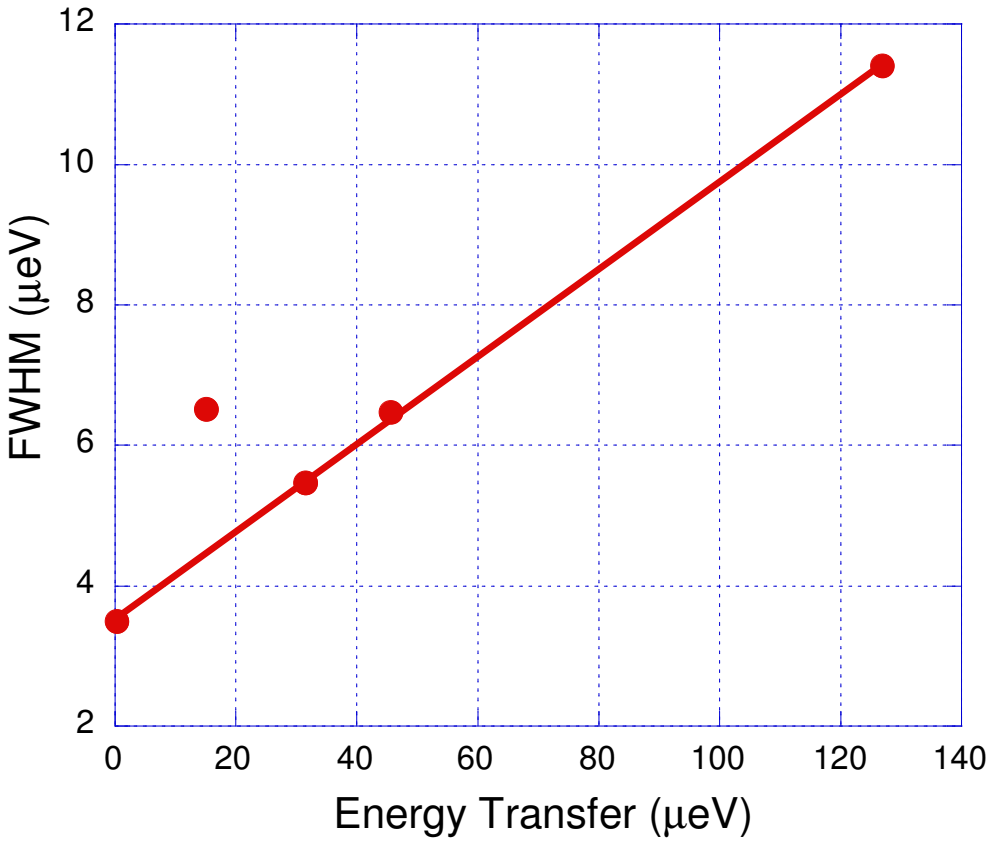

Figure 50. Peak Width Analysis of CH_2D_2 Spectrum.

Widths are from peaks on energy loss side of spectrum. These are plotted against the magnitude of energy transfer. The linear curve fit excludes the transition(s) at 15 μeV.

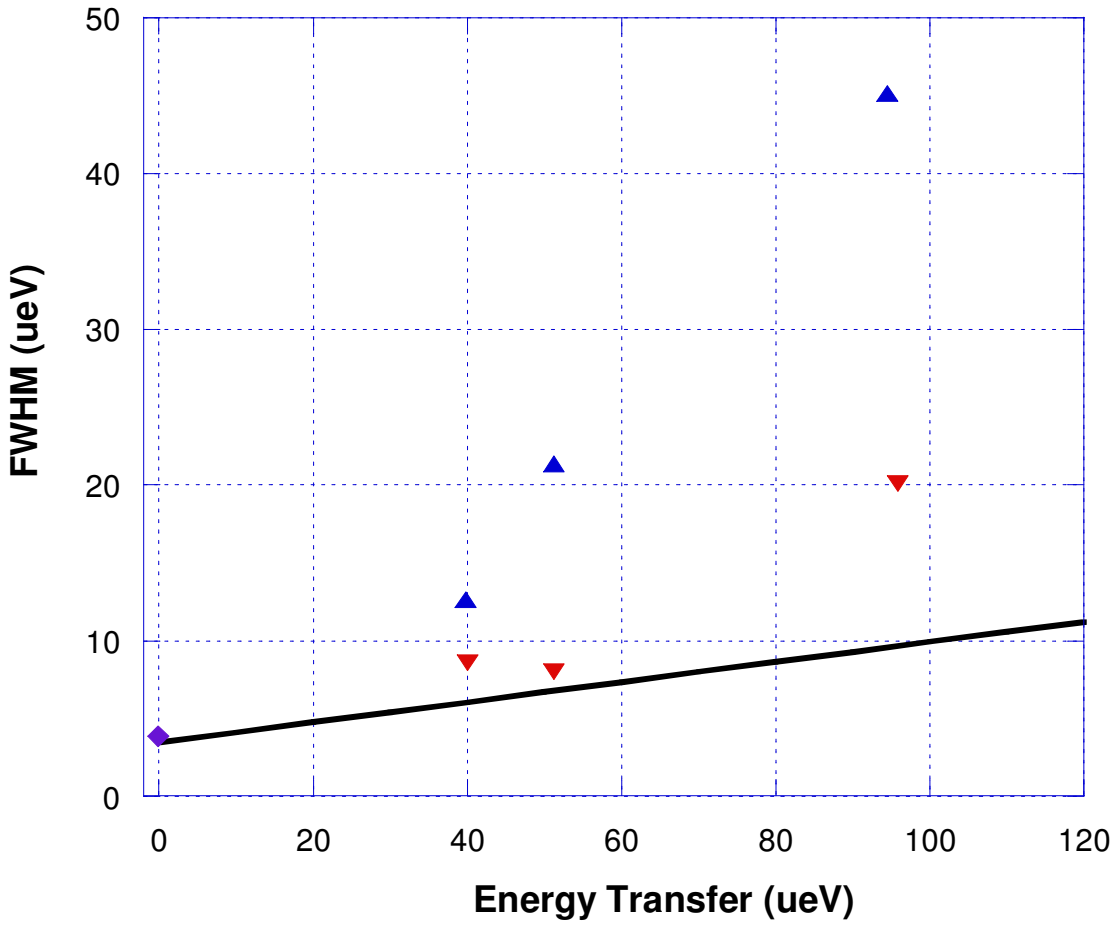

Figure 51. Peak Width Analysis of CH_3D spectrum.

*There is no discernible trend for features on either the energy loss side (*red*) or energy gain side (*blue*). Elastic peak is shown in* purple*. Linear curve fit from CH_2D_2/MgO peak width analysis (*black*) is shown to highlight the nonlinear behavior of CH_3D/MgO.*

PS	D	D	M	M	M	M	M	M	M	M	H	H
D	D	T_D	0	0	0	0	0	0	0	0	0	0
D	T_D	D	0	0	0	0	0	0	0	0	0	0
M	0	0	M	T	t_1	t_3	t_4	t_2	$T_\perp$	$T_\parallel$	0	0
M	0	0	T	M	t_3	t_1	t_2	t_4	$T_\parallel$	$T_\perp$	0	0
M	0	0	t_1	t_3	M	T	$T_\parallel$	$T_\perp$	t_2	t_4	0	0
M	0	0	t_3	t_1	T	M	$T_\perp$	$T_\parallel$	t_4	t_2	0	0
M	0	0	t_4	t_2	$T_\parallel$	$T_\perp$	M	T	t_3	t_1	0	0
M	0	0	t_2	t_4	$T_\perp$	$T_\parallel$	T	M	t_1	t_3	0	0
M	0	0	$T_\perp$	$T_\parallel$	t_2	t_4	t_3	t_1	M	T	0	0
M	0	0	$T_\parallel$	$T_\perp$	t_4	t_2	t_1	t_3	T	M	0	0
H	0	0	0	0	0	0	0	0	0	0	H	T_H
H	0	0	0	0	0	0	0	0	0	0	T_H	H

Figure 52. CH_2D_2/MgO 12x12 Hamiltonian Matrix.

The twelve PS's are labeled in the top row and far left column. Diagonal elements correspond to the zero-point energies for each state. Two-fold overlaps are labeled with a capital "T", and three-fold overlaps with a lowercase "t".

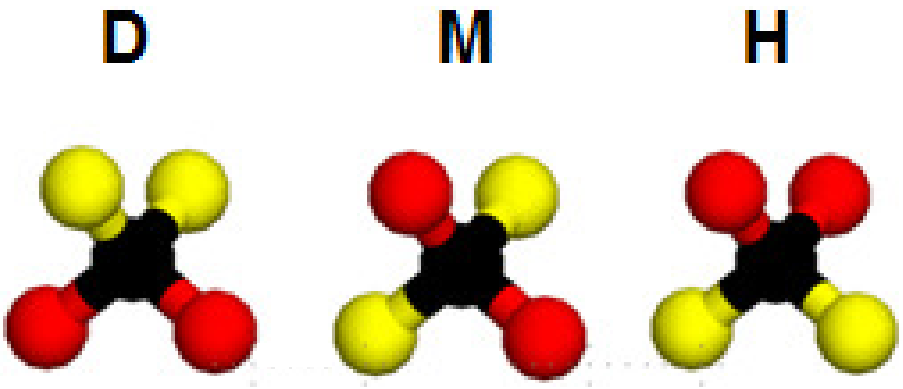

Figure 53. Three unique PS's for CH_2D_2.

The twelve equilibrium orientations can be divided into three types of states. Deuterium atoms are shown in red, protium atoms in yellow. States are labeled according to which nuclei are facing toward to the surface (toward the bottom of the page): deuterons (D states), protons (H states), or one of each (M—or mixed—states). Degeneracies of each type of state are below in parentheses.

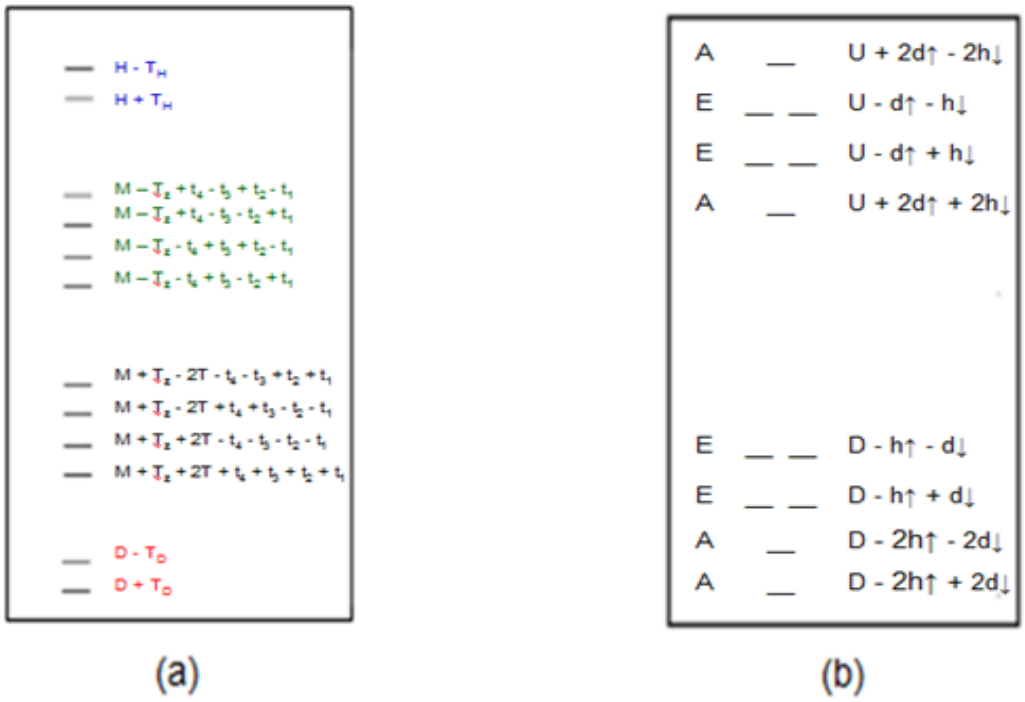

Figure 54. Preliminary Tunneling Diagrams.

(a) CH_2D_2/MgO: Diagonalizing Hamiltonian matrix yields twelve nondegenerate eigenvalues.

(b) CH_3D/MgO: Eigenvalues are divided into U and D blocks, each consisting of two doublet states of E symmetry and two singlet states of A symmetry.

PS	U	U	U	U	U	U	D	D	D	D	D	D
U	U	d↑	d↑	h↓	0	h↓	0	0	0	0	0	0
U	d↑	U	d↑	h↓	h↓	0	0	0	0	0	0	0
U	d↑	d↑	U	0	h↓	h↓	0	0	0	0	0	0
U	h↓	h↓	0	U	d↑	d↑	0	0	0	0	0	0
U	0	h↓	h↓	d↑	U	d↑	0	0	0	0	0	0
U	h↓	0	h↓	d↑	d↑	U	0	0	0	0	0	0
D	0	0	0	0	0	0	D	d↓	h↑	h↑	0	d↓
D	0	0	0	0	0	0	h↑	D	d↓	0	d↓	h↑
D	0	0	0	0	0	0	h↑	h↑	D	d↓	d↓	0
D	0	0	0	0	0	0	h↑	0	d↓	D	d↓	h↑
D	0	0	0	0	0	0	0	h↑	d↓	d↓	D	h↑
D	0	0	0	0	0	0	d↓	d↓	0	h↑	h↑	D

Figure 55. CH_3D/MgO 12x12 Hamiltonian Matrix.

There are two unique diagonal elements, and only the C_3 overlaps are nonzero. For a C_3 rotation, one proton/deuteron will remain stationary, and the off-diagonal elements are labeled according whether this stationary atom is a proton (h) or deuteron (d), and whether it points away (↑) or toward (↓) the surface.

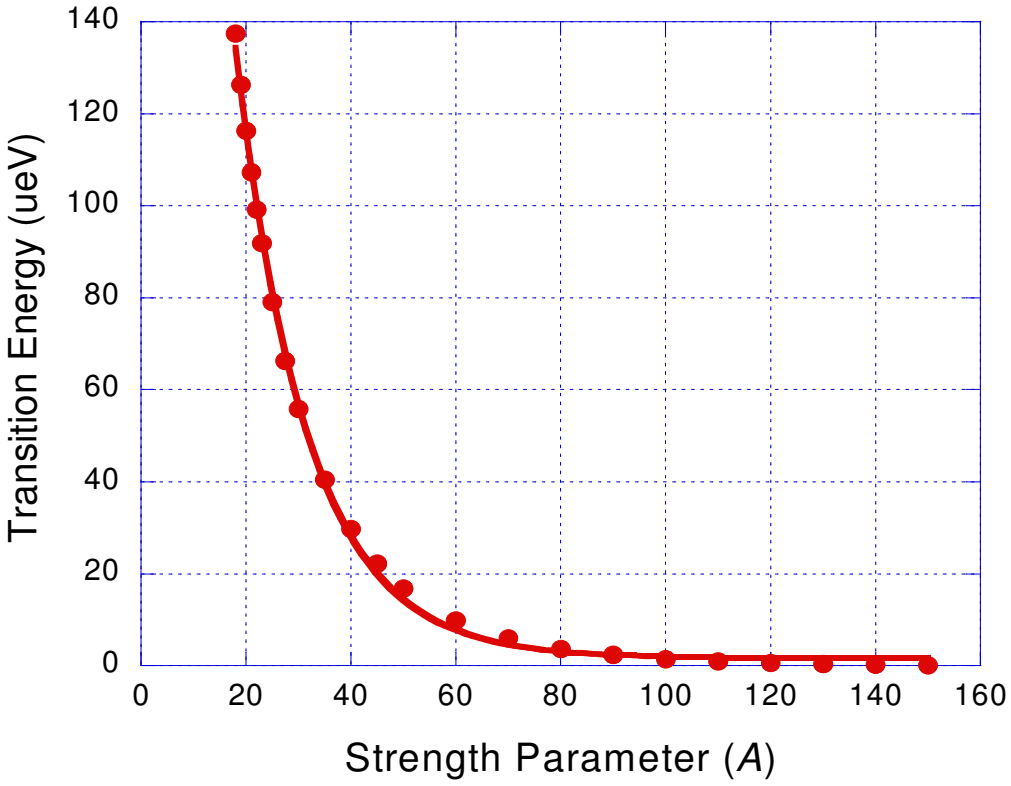

Figure 56. $H_A \rightarrow H_B$ / $D_A \rightarrow D_B$ vs. Potential Strength.

Strength parameter A *is expressed in units of average rotational constant of* CH_2D_2 *(436 μeV), and an exponential decay curvefit applied. Expressions for* $H_A \rightarrow H_B$ *&* $D_A \rightarrow D_B$ *are identical except for choice of potential strength parameter.*

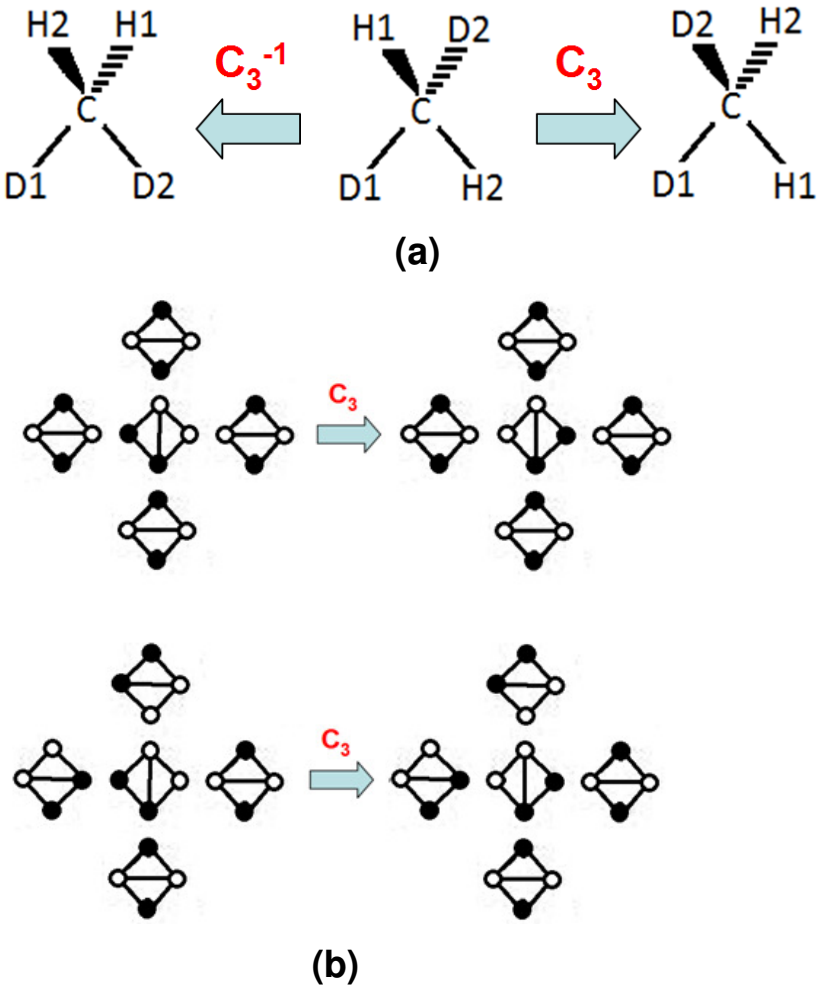

Figure 57. C_3 reorientations of CH_2D_2.

*(a) C_3 rotations about lower C-D bond for a B state (*middle*). Note the position of upper H and D atoms.*

*(b) Top view of same C_3 rotation for two molecules in same M orientation (*center tetrahedra in each frame*) but with different NN configurations. Deuterons shown as filled circles, protons as open circles.* Top: *All NN's in D orientations. For an ideal lattice, the initial and final states would be degenerate.* Bottom: *Top and left NN's are in M orientations. Thus, the final and initial states would not be degenerate.*

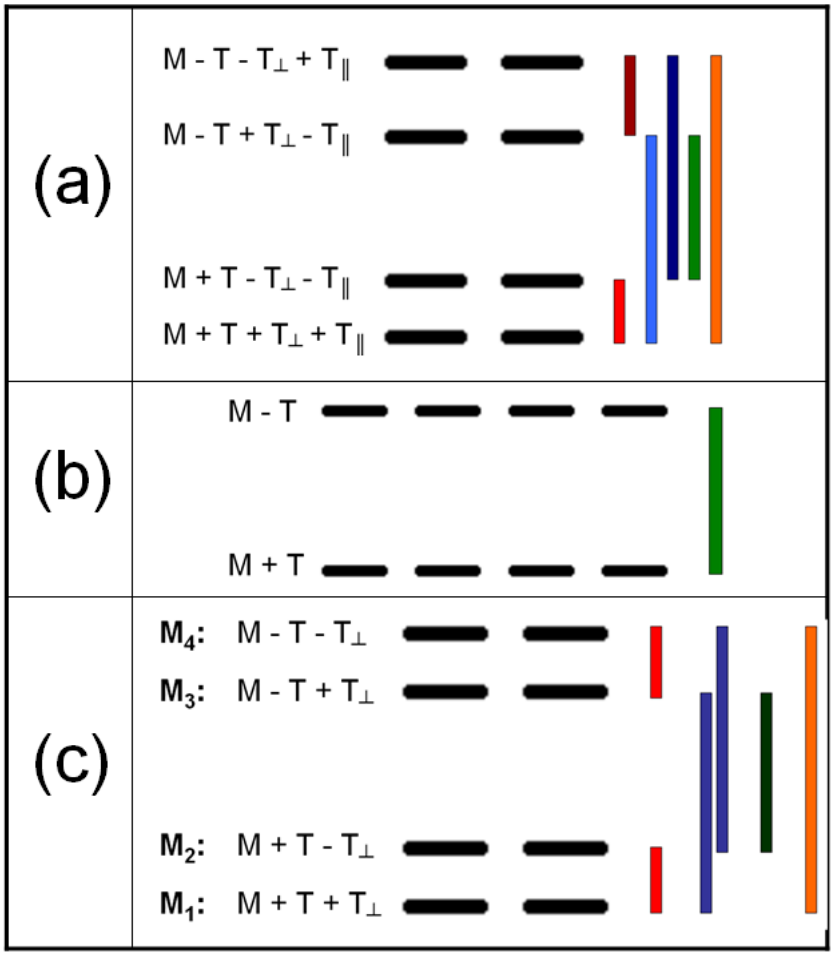

Figure 58. Diagram of M sublevels under three sets of assumptions.

(a) Tunneling is appreciable about all three C_2 axes.

(b) Tunneling is appreciable only the about true molecular axis and is negligible about both virtual axes.

(c) Tunneling is appreciable about axes coincident with molecular and site C_2 axes but negligible about virtual axis parallel to the surface. Although there are six possible transitions, two pairs of these (color coded in red *and* blue*) are of identical energy.*

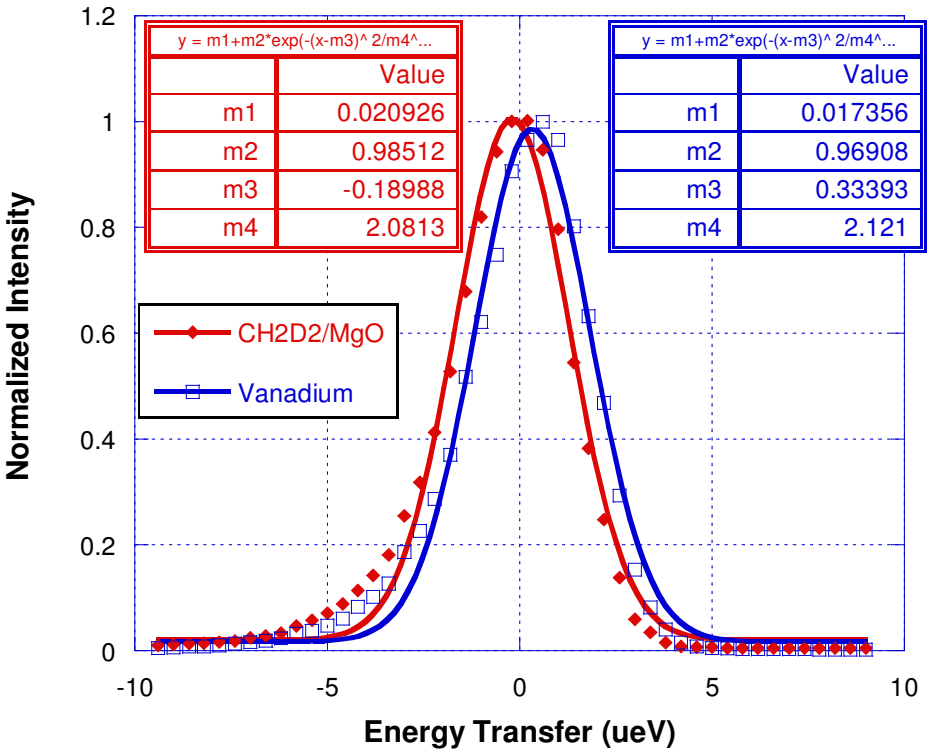

Figure 59. CH_2D_2/MgO and Vanadium Elastic Peaks.

VITA

Andrew Spencer Hicks was born in Memphis, TN. His family moved twice before he turned three, and thereafter he lived in Kinsgport, TN, where he graduated from Dobyns-Bennett High School in 2002. He then completed his undergraduate studies at the University of South Carolina-Columbia, graduating in May 2006 with a Bachelor of Science in Chemistry and a minor in German. After working for a year at 3V, Inc in Georgetown, SC, he returned closer to home to study chemical physics at the University of Tennessee-Knoxville.